THE ASTROPHYSICAL JOURNAL, 334:771–802, 1988 November 15

THE PHOTODISSOCIATION AND CHEMISTRY OF INTERSTELLAR CO

EWINE F. VAN DISHOECK
Princeton University Observatory
AND
JOHN H. BLACK
Steward Observatory, University of Arizona
Received 1988 February 12; accepted 1988 May 18

Recent work on the vacuum ultraviolet absorption spectrum of CO by Letzelter *et al.* and Yoshino *et al.* has clarified the nature of its photodissociation processes. The application of these spectroscopic data to the description of the photodissociation of interstellar CO and its principal isotopic varieties ^{13}CO, $C^{18}O$, and $^{13}C^{18}O$ is discussed. The unattenuated photodissociation rate of interstellar CO is $\sim 2 \times 10^{-10}$ s^{-1}, more than an order of magnitude larger than the value used in previous models. The effects of line broadening, self-shielding, shielding by H and H_2, and isotope-selective shielding are examined as functions of depth into interstellar clouds. The photodissociation rates of the isotopic species are larger than that of ^{12}CO inside the clouds by up to 1–2 orders of magnitude. A simple approximation to the attenuation by line absorptions is provided in tabular form. The new treatment of the CO photodissociation has been incorporated into detailed models of the structure and chemistry of interstellar clouds. Computed abundances of CO and related species C and C^+ are presented for a variety of interstellar clouds ranging from diffuse clouds to dense photodissociation regions. The large photodissociation rate of CO poses problems in explaining the observed CO column densities in diffuse clouds. A modification of the conventionally adopted interstellar ultraviolet radiation field at $\lambda < 1000$ Å may be necessary to bring the models into harmony with observations of these clouds. Several series of models of translucent clouds are presented which illustrate how the CO abundance increases rapidly with total thickness of the cloud. The variations of the isotopic abundances with depth, and their sensitivity to temperature and total cloud thickness, are explored in detail. The model results are compared with a variety of observational data on both the CO and C abundances in such clouds. Models of dense photodissociation regions show that substantial amounts of atomic carbon can be formed near the edges of the clouds. The consequences of a clumpy structure of interstellar clouds on the model results need to be investigated further.

Subject headings: interstellar: matter — interstellar: molecules — molecular processes

I. INTRODUCTION

Carbon monoxide is generally believed to be the most abundant interstellar molecule after H_2, and its millimeter wavelength rotational lines are widely used as tracers of molecular material in interstellar clouds. However, the abundance of CO relative to that of H_2 is poorly determined observationally and has not been well understood theoretically (see, e.g., Williams 1985; van Dishoeck and Black 1987 for reviews). One of the major theoretical uncertainties is the rate at which the molecule is photodissociated by ultraviolet starlight. This rate governs the abundance of CO and its growth with depth in diffuse clouds and the outer parts of thick molecular clouds. Even deep inside dense clouds, photodissociation of CO by cosmic-ray-induced photons may significantly influence the chemistry (Prasad and Tarafdar 1983; Gredel, Lepp, and Dalgarno 1987). A good understanding of the CO photodissociation processes is also needed to explain observations of CO in circumstellar envelopes (Morris and Jura 1983; Mamon, Glassgold, and Huggins 1988) and in cometary atmospheres.

The photodissociation processes of interstellar CO have been discussed previously by Solomon and Klemperer (1972), Bally and Langer (1982), Glassgold, Huggins, and Langer (1985), and van Dishoeck and Black (1986*a*). Although it has been clear for some time that the CO photodissociation is dominated by line rather than continuous absorptions, accurate calculations have been hampered by a lack of basic molecular data. Recent quantitative high-resolution spectroscopic studies in the laboratory (Letzelter *et al.* 1987; Yoshino *et al.* 1988) have begun to remove previous major uncertainties about the positions, oscillator strengths, and intrinsic widths of the dissociating transitions of CO at vacuum ultraviolet wavelengths. We incorporate here the new spectroscopic data on both the vibrational and rotational structure of the bands into a complete description of the depth-dependent photodissociation of ^{12}CO, and of its principal isotopic variants ^{13}CO, $C^{18}O$, and $^{13}C^{18}O$.[1] A similar study for ^{12}CO considering only the vibrational structure has recently been performed independently by Viala *et al.* (1988). The astrophysical implications of the new photodissociation rates are explored through detailed models of the structure and chemistry of interstellar clouds (see van Dishoeck and Black 1986*a*; Black and van Dishoeck 1988). The application of the new data to the photodissociation of CO in circumstellar envelopes has been investigated by Mamon *et al.* (1988).

The photodissociation processes in CO and the adopted molecular parameters are reviewed in detail in § II. The problems involved in the calculation of the depth-dependent photodissociation rates of CO and its isotopes are discussed in § III. The resulting CO abundances in a variety of interstellar clouds ranging from diffuse clouds to dense clouds exposed to intense radiation fields will be presented in § IV.

[1] If no nuclear mass is specified, the main species ^{12}C and ^{16}O are implied.

II. MOLECULAR DATA

The photodissociation of a molecule in general can take place either directly by continuous absorption into the repulsive part of an excited electronic state, or indirectly by discrete absorptions into predissociated bound states (see van Dishoeck 1987, 1988*a*). The dissociation energy of ground state CO is 11.09 eV, so that photodissociation of interstellar CO can occur only at wavelengths $911.75 < \lambda < 1117.8$ Å. Detailed knowledge of the electronic states of CO lying 11.09–13.6 eV above the ground state is thus needed.

Early measurements of the vacuum ultraviolet absorption cross sections of CO at low resolution (Huffman, Larrabee, and Tanaka 1964; Cook, Metzger, and Ogawa 1965) indicated the presence of a dissociation continuum between 912 and 960 Å. Hudson (1971) noted, however, that this continuum may be due to a number of discrete, unresolved, overlapping lines, a suggestion which has subsequently been confirmed by higher resolution measurements of Fock, Gürtler, and Koch (1980) and Letzelter *et al.* (1987). Letzelter *et al.* find no evidence for continuous absorption at $\lambda > 885$ Å and tabulate upper limits to the cross section at several points between lines which imply an integrated continuous absorption cross section of less than 9×10^{-17} cm^2 Å over the range 912–1118 Å. The true integrated continuum absorption is likely to be considerably weaker than this and is negligible compared with the total integrated absorption cross section through bands.

Information about possible continuum photodissociation channels can also be obtained from theory. The electronic ground state of CO has $^1\Sigma^+$ symmetry, so that strong electric dipole allowed transitions are possible to states of $^1\Sigma^+$ or $^1\Pi$ symmetry. Recent extensive quantum chemical calculations of the electronic structure of CO reveal no repulsive states of $^1\Sigma^+$ or $^1\Pi$ symmetry lying longward of 912 Å (Cooper and Kirby 1987). Thus the CO photodestruction must occur mostly through line absorptions into predissociating states. The ionization threshold of CO is at 885 Å, so that photoionization does not occur in the general interstellar radiation field.

Calculations of the photodissociation rate through line absorptions, and of its depth dependence, require accurate information on the line positions, the oscillator strengths, the line widths, and the predissociation probabilities. Most of these data can be obtained reliably only from very high resolution measurements under experimental conditions where pressure saturation effects are absent. The fact that all the CO predissociating transitions lie at vacuum ultraviolet wavelengths further complicates the experiments, since only synchrotron radiation sources can be used effectively as continuous background light sources to perform absorption cross section measurements.

a) Line Positions and Identifications

The vacuum ultraviolet spectrum of ^{12}CO has been analyzed by Ogawa and Ogawa (1972, 1974) and summarized by Huber and Herzberg (1979). The spectrum is well understood down to 1000 Å, but many of the bands at shorter wavelengths have not yet been fully analyzed spectroscopically. Letzelter *et al.* (1987) identified ~30 bands between 912 and 1118 Å, but their resolution of 0.15 Å was too low to resolve the rotational structure needed to assign the bands. Yoshino *et al.* (1988), Stark *et al.* (1987), and Eidelsberg, Letzelter, and Rostas (1987) obtained higher resolution spectra on which the rotational structure can clearly be distinguished, but analysis of these spectra is still in progress.

In order to simulate the absorption spectrum of CO and its isotopes in interstellar clouds, the electronic symmetry of each upper state, its vibrational quantum number, and its rotational constants need to be known. Stark *et al.* (1987) have kindly provided us with a list of their measured line positions of ^{12}CO on the high-resolution spectra, together with a preliminary analysis of the bands. The results are summarized in Table 1, where the adopted band head positions and rotational constants are listed. Some bands, such as Nos. 11 and 19, are so diffuse that no rotational analysis has been possible, and the listed constants are only estimates. Note also that some of the bands listed by Letzelter *et al.* (1987), such as their Nos. 14 and 15 (bands 10–13 of Table 1), can actually be separated into two or more different electronic transitions on the higher resolution spectra. Many of the bands probably belong to Rydberg series converging to the CO^+ $^2\Sigma^+$ ground state at 885 Å. The electronic identifications $^1\Sigma^+$ or $^1\Pi$ listed in Table 1 are obtained from previously published analyses or from the preliminary rotational analyses by Stark *et al.* (1987). Some plausible assignments of the Rydberg states can be made. For example, based on the positions of the $B(3s\sigma)$ $^1\Sigma^+$ and $J(4s\sigma)$ $^1\Sigma^+$ states, the transition to the $5s\sigma$ $^1\Sigma^+$ state is expected to occur around 940 Å. Similarly, transitions to the $5p\sigma$ and $5p\pi$ $^1\Sigma^+$ and $^1\Pi$ states are expected to lie in the 931–933 Å region, where indeed a complex pattern of $^1\Sigma^+$ and $^1\Pi$ states is observed. Some of the bands in the 912–920 Å region may involve transitions to the $6s\sigma$ and $6p\sigma$ $^1\Sigma^+$ states. Firm identifications cannot be made at present, however, owing to the large number of possible perturbations between the states. Most of the Rydberg transitions are assumed to involve the $v' = 0$ upper vibrational level. The major exception is formed by a series of $^1\Pi$–X $^1\Sigma^+$ transitions, of which the first member at 972.7 Å is denoted as the W $^1\Pi$–X $^1\Sigma^+$ system. The rotational constants for the upper states of the bands at 972.7, 941.1, 925.8, and possibly 956 Å have been found to be systematically smaller than those of other typical Rydberg states. One possible explanation for these anomalous bands is that they involve the same $^1\Pi$ upper state with different vibrational quantum numbers (Lindholm 1968). The W $^1\Pi$ state may have its equilibrium internuclear distance displaced by $\sim 0.2a_0$ from that of the X $^1\Sigma^+$ state; calculations of Franck-Condon factors indicate that such a shift would result in a progression of bands peaking around $v' = 2$–3. A plausible assignment for this state involves a $1\pi \rightarrow 3s\sigma$ excitation, so that the W state would be the first member of a Rydberg series converging to the CO^+ A $^2\Pi$ state. This assignment would be consistent with the fact that the equilibrium internuclear distance of the A state is larger than that of the CO X $^1\Sigma^+$ state by $\sim 0.2a_0$ (Huber and Herzberg 1979). The W state presumably has relatively strong interactions with other nearby $^1\Pi$ states such as the $4p\pi$ state, so that the vibrational spacing is irregular. The corresponding $1\pi \rightarrow 3p\sigma$ and $1\pi \rightarrow 3p\pi$ $^1\Pi$ and $^1\Sigma^+$ states lie much higher in energy, so that transitions to them cannot occur at $\lambda > 912$ Å. Most of the remaining bands for which no plausible (Rydberg) configuration could be found have been assumed to involve $v' = 0$. The upper states of these bands may actually be vibrationally excited levels of identified Rydberg states. An alternative identification would be a configuration with a $4\sigma \rightarrow 3s\sigma$ or $3p\sigma$ excitation. Note that of the transitions listed in Table 1, only the E–X (0, 0) and (1, 0), and the C–X (1, 0) bands were taken into account in previous work (Glassgold *et al.* 1985). It should be stressed again that many line positions may be uncertain by several wavenumbers and need to be confirmed by more detailed spectroscopic analyses.

TABLE 1

ADOPTED SPECTROSCOPIC DATA FOR CO

Band No.	LEFBT[a] No.	λ (Å)	f[b]	A[c] (s^{-1})	η[d]	Identification	Adopted v'	^{13}CO shift[e]	ν_0 (cm^{-1})	B' (cm^{-1})	D' (cm^{-1})	Notes
1	7	913.601	3.4 (-2)	3.0 (11)	1.00	$^1\Pi$	nz[f]	yes	109457.0	1.7393	2.0 (-4)	g,h
2	8	915.968	9.9 (-3)	3.0 (11)	1.00	$^1\Sigma^+$	0	?	109174.1	1.6627	-7.304(-4)	g
3	9	917.011	1.8 (-2)	3.0 (11)	1.00	$^1\Pi$	0	yes	109050.	1.9225	6.121 (-6)	g,i
4	9	919.210	5.0 (-3)	3.0 (11)	1.00	$^1\Sigma^+$	0	no	108789.1	2.1357	4.633 (-5)	g
5	9	920.143	5.0 (-3)	1.0 (11)	1.00	$I'\ ^1\Sigma^+$	nz	yes	108678.7	1.8989	-3.63 (-5)	g
6	10	922.696	6.3 (-3)	1.0 (11)	1.00	$^1\Sigma^+$	0	?	108378.0	1.9225	6.121 (-6)	g,i
7	11	924.635	5.2 (-3)	1.0 (11)	1.00	$^1\Sigma^+$	0	yes	108150.8	1.8629	8.882 (-6)	g
8	12	925.813	1.6 (-2)	3.0 (11)	1.00	$^1\Pi$	nz	yes	108013.2	1.6679	2.502 (-4)	g,h
9	13	928.664	6.7 (-3)	5.0 (10)	1.00	$^1\Pi$	0	yes	107681.5	1.9342	2.529 (-4)	g
10	14	930.060	3.2 (-3)	1.0 (11)	1.00	$^1\Pi$	0	yes	107520.0	1.8101	-1.107 (-4)	g
11	14	930.800	3.2 (-3)	3.0 (11)	1.00	$^1\Pi$?	nz	yes	107434.5	1.9	0.0	g,i
12	15	931.498	2.0 (-2)	3.0 (11)	1.00	$^1\Pi$?	0	yes	107354.0	1.9810	3.189 (-6)	g,o
13	15	933.097	2.0 (-2)	3.0 (11)	1.00	$^1\Sigma^+$?	0	yes	107170.0	1.9163	5.241 (-5)	g,p
14	16	935.699	2.9 (-3)	3.0 (11)	1.00	$^1\Sigma^+$?	0	yes	106872.0	1.95	0.0	g
15	17	939.957	2.1 (-2)	1.0 (12)	1.00	$I'^1\Sigma^+$	0	yes	106387.8	2.080	6.121 (-6)	g,n
16	18	941.174	2.6 (-2)	1.0 (11)	1.00	$^1\Pi$	nz	yes	106250.3	1.6315	4.99 (-5)	g,h
17	19	946.285	7.6 (-3)	1.0 (11)	1.00	$^1\Sigma^+$	0	yes	105676.4	1.8880	-3.17 (-5)	g
18	20	948.290	2.8 (-3)	1.0 (11)	1.00	$L(4p\pi)^1\Pi$	1	yes	105453.0	1.9839	2.966 (-5)	k
19	21	950.043	2.2 (-2)	1.0 (12)	1.00	$^1\Sigma^+$	0	yes	105258.4	1.9	0.0	g,j
20	22	955.996	1.4 (-2)	1.0 (12)	1.00	$^1\Pi$	nz	?	104603.0	1.58	5.0 (-4)	g,h,q
21[r]	24	964.360	2.8 (-3)	3.0 (11)	1.00	$J(4s\sigma)^1\Sigma^+$	1	yes	103695.7	1.9072	-1.48 (-4)	g
22	25	968.320	8.6 (-3)	1.0 (10)	0.99	$L(4p\pi)^1\Pi$	0	yes	103271.7	1.9839	2.966 (-5)	g,r
23	26	968.884	1.8 (-2)	1.0 (11)	1.00	$L'\ ^1\Pi$	0	yes	103211.5	1.7986	1.229 (-5)	g,r
24	27	970.360	1.5 (-2)	1.0 (10)	0.99	$K(4p\sigma)^1\Sigma^+$	0	no	103054.6	1.9161	5.82 (-5)	g,r
25	28	972.701	1.2 (-2)	1.0 (10)	0.96	$W^1\Pi$	0	yes	102806.5	1.5705	1.434 (-4)	g,h
26	29	977.416	1.8 (-3)	1.0 (11)	1.00	$W'\ ^1\Pi$	0	yes	102310.6	1.536	0.0	l
27	30	982.570	4.8 (-4)	1.0 (12)	1.00	$F(3d\sigma)^1\Sigma^+$	1	yes	101773.9	1.8193	-1.279 (-4)	m
28	31	985.649	1.5 (-2)	3.0 (11)	1.00	$J(4s\sigma)^1\Sigma^+$	0	?	101456.0	1.942	0.0	s
29	32	989.795	4.6 (-4)	1.0 (11)	1.00	$G(3d\pi)^1\Pi$	0	no	101031.0	1.9625	7.0 (-6)	l
30	33	1002.610	7.9 (-3)	1.0 (11)	1.00	$F(3d\sigma)^1\Sigma^+$	0	no	99739.713	1.8094	-2.129 (-4)	m
31	37	1051.704	2.5 (-3)	1.0 (11)	0.98	$E(3p\pi)^1\Pi$	1	yes	95083.770	1.9390	6.00 (-6)	l
32	38	1063.087	2.8 (-3)	5.0 (8)	0.60	$C(3p\sigma)^1\Sigma^+$	1	yes	94065.636	1.9236	5.023 (-6)	t,u
33	39	1076.079	3.7 (-2)	1.0 (9)	0.89	$E(3p\pi)^1\Pi$	0	no	92929.9750	1.9646	6.543 (-6)	t,v

[a] Band index number from Table 1 of Letzelter *et al.* 1987. Note that LEFBT Nos. 9, 14, and 15 were not resolved.
[b] Band oscillator strength from Letzelter *et al.* 1987 unless otherwise noted.
[c] Total inverse lifetime of the upper state estimated from the apparent diffuseness in the high-resolution spectra of Stark *et al.* 1987 unless otherwise noted.
[d] Predissociation probability based upon results of Letzelter *et al.* 1987.
[e] ^{13}CO shifts measured from spectra by Stark *et al.* 1988. "Yes" indicates a shift with respect to ^{12}CO greater than 10 cm^{-1}; "no" indicates a shift smaller than 10 cm^{-1}.
[f] "nz" indicates that a nonzero upper state vibrational quantum number was adopted.
[g] Line positions and spectroscopic constants are from the preliminary measurements of Stark *et al.* 1987.
[h] Bands 1, 8, 16, 20, and 25 are consistent with a vibrational progression as noted previously by Lindholm 1968. The $W\ ^1\Pi$ state was characterized as a Rydberg state arising from the configuration $(1\pi)^3(5\sigma)^2(3s\sigma)$ by Ogawa and Ogawa 1974.
[i] No analysis: ground-state rotational constants assumed.
[j] This transition has evidently been listed as $H\ ^1\Pi$–$X\ ^1\Sigma^+\ v' = 0$ by Huber and Herzberg 1979. According to Stark *et al.* 1987, the upper state is more likely $^1\Sigma^+$ with $B' \approx B''$. $K(4p\sigma)\ ^1\Sigma^+\ v' = 1$ is a plausible identification; see Ogawa and Ogawa 1972.
[k] Ogawa and Ogawa 1972 suggest the assignment as $(4p\pi)\ v' = 1$; hence, we adopt the same rotational constants as for band 22, $L(4p\pi)\ v' = 0$.
[l] Spectroscopic constants and/or line positions are from Ogawa and Ogawa 1974.
[m] Line positions are from Ogawa and Ogawa 1974; constants have been recomputed for $J < 10$.
[n] $D' = D''$ is assumed.
[o] No analysis: same rotational constants as in an earlier analysis of band 22 $L(4p\pi)\ ^1\Pi$ are assumed.
[p] No analysis: same rotational constants as in an earlier analysis of band 24 $K(4p\sigma)\ ^1\Sigma^+$ are assumed.
[q] No analysis: assumed rotational constants are in harmony with those of the other members of the progression.
[r] An oscillator strength from the higher-resolution data of Yoshino *et al.* 1988 has been adopted.
[s] See Ogawa and Ogawa 1974. No analysis: adopted rotational constants are in harmony with those of band 21 $J(4s\sigma)\ ^1\Sigma^+\ v' = 1$.
[t] Analysis from Amiot, Roncin, and Verges 1986.
[u] Isotopic data are in Tilford and Vanderslice 1968.
[v] Isotopic data are in Tilford, Vanderslice, and Wilkinson 1965.

The photodissociation of the isotopic species is complicated by the fact that they may be shielded by the more abundant ^{12}CO molecule inside the clouds if their lines coincide with those of ^{12}CO. In general, isotopic shifts are expected to be small for lines involving zero vibrational quantum numbers, but significant otherwise. The identification and inclusion of some bands with nonzero vibrational quantum numbers between 912 and 1118 Å in the calculations thus has important consequences for the depth dependence of the photodissociation of the isotopic species. Table 1 indicates the transitions for which we have assumed a nonzero upper state vibrational quantum number. Wavelengths for all lines of ^{12}CO, ^{13}CO, $C^{18}O$, and $^{13}C^{18}O$ arising from $X\ ^1\Sigma^+$, $v'' = 0$, $J'' = 0$–9 have been generated based on direct laboratory measurements where available, or on the molecular constants listed in Table 1 otherwise. The rotational and vibrational constants of the isotopic species have been obtained from those for ^{12}CO by scaling with the appropriate mass ratio, wherever directly measured values are not available. In the absence of specific spectroscopic measurements for isotopic species, the values of the equilibrium term values T_e are assumed to be the same for all species.

After this paper was submitted for publication, Stark *et al.* (1988) kindly obtained high-resolution spectra of ^{13}CO for us. Compared with the ^{12}CO spectra, many ^{13}CO bands—including those which most likely involve zero vibrational quantum numbers—appear to be shifted by amounts ranging from a few to nearly 200 cm^{-1}. Those bands which show ^{13}CO shifts in excess of 10 cm^{-1} on the new spectra are indicated in Table 1, where they can be compared with our assignments of vibrational quantum numbers. It appears that a number of ^{13}CO bands for which we have adopted virtually no shifts, such as band Nos. 26, 25, 19, 13, 12, and 3, are actually shifted significantly, suggesting that ^{13}CO may be photodissociated even more rapidly inside clouds than assumed in this work. On the other hand, we had assigned a nonzero vibrational quantum number to band 20, whereas it actually exhibits only a small shift. These new spectra also indicate that our assignment of bands 25, 10, 16, and 8 to a single progression involving the $W(1\pi \rightarrow 3s\sigma)$ configuration is an oversimplification, and that interactions with other states play a role. The influence of these different shifts on the results for the isotopic species will be discussed throughout §§ III*c* and IV.

b) Oscillator Strengths

Lee and Guest (1981) measured absorption cross sections of ^{12}CO in the 1060–1600 Å range using synchrotron radiation, whereas Fock *et al.* (1980) explored the cross sections down to 880 Å. In both experiments, the pressure saturation effects may have been severely underestimated. Letzelter *et al.* (1987) recently redetermined the photoabsorption cross sections in the 885–1150 Å range at 0.15 Å resolution and obtained significantly larger values. Note that at 0.15 Å resolution, the individual rotational lines within the observed bands are still not resolved. Measurements at the 20 times higher resolution of 0.007 Å are currently being carried out by Yoshino *et al.* (1988). Preliminary results reported by Yoshino *et al.* indicate that the cross sections given by Letzelter *et al.* may still be too low by up to factors of 2 for some bands. Reliable theoretical calculations of oscillator strengths can be made only for the lowest members of each Rydberg series. As summarized in Table 2 of van Dishoeck and Black (1987), the most recently computed oscillator strengths for the $C\ ^1\Sigma^+$–$X\ ^1\Sigma^+$ and $E\ ^1\Pi$–$X\ ^1\Sigma^+$ (0, 0) bands by Kirby and Cooper (1987) agree well with, or are slightly larger than, the measured values of Letzelter *et al.* (1987). The adopted oscillator strengths are included in Table 1. Several weak bands with $f < 5 \times 10^{-5}$ listed by Letzelter *et al.* (1987) as Nos. 34–36 were not included in this work.

c) Predissociation Probabilities and Line Widths

Absorption of a photon into a discrete state below the first ionization threshold can result either in dissociation of the molecule or in emission of another photon. The relative probabilities for these processes can be determined experimentally by simultaneous measurements of the absorption and fluorescence cross sections. The measurements are complicated by the fact that the emission can occur over a wide range of wavelengths, all of which must be sampled to infer the total fluorescence cross sections. Such experiments have been performed by Letzelter *et al.* (1987), and estimates of the fluorescence cross sections are listed in their work. For most bands at short wavelengths, $\lambda < 1000$ Å, virtually no fluorescence is observed, suggesting that the upper states are rapidly predissociated.

If k^{pr} is the rate in s^{-1} at which level v', J' of an upper electronic state is predissociated, then the probability $\eta_{v'J'}$ that absorption into that level leads to dissociation is given by

$$\eta_{v'J'} = \frac{k^{pr}}{k^{pr} + A^{rad}}, \quad (1)$$

where A^{rad} is the summed radiative transition probability to all lower lying states. The total inverse lifetime of the level $A = A^{rad} + k^{pr}$. The adopted values of $\eta_{v'J'}$ based on the work of Letzelter *et al.* are listed in Table 1. The predissociation probability is related to a line width Γ in cm^{-1} through $\Gamma = 5.3 \times 10^{-12} k^{pr}$. Radiative transition probabilities are typically 10^8–10^9 s^{-1} for strong ultraviolet transitions. Thus if k^{pr} is comparable to A^{rad}, the line widths are typically 10^{-3} cm^{-1}, which are too small to be measured by current spectroscopic techniques. Strong predissociations, however, often involve rates of the order of $k^{pr} \approx 10^{11}$–10^{12} s^{-1}, resulting in line widths $\Gamma \approx 0.5$–5 cm^{-1} that are large enough to be detectable on high-resolution spectra.

Predissociation widths were estimated from unpublished high-resolution spectra of Stark *et al.* (1987) on the basis of their diffuseness. The resolution of ~ 0.5 cm^{-1} corresponds to a minimum detectable predissociation rate of $\sim 10^{11}$ s^{-1}. Bands that are diffuse but still show rotational structure have been assigned predissociation probabilities $k^{pr} \approx (1$–$3) \times 10^{11}$ s^{-1}, whereas the most diffuse bands are assumed to have $k^{pr} \approx 10^{12}$ s^{-1}. Note that sharp features on these spectra can still be significantly predissociated with $k^{pr} \approx 10^9$–10^{10} s^{-1}. For those sharp bands for which the predissociation probabilities were measured to be less than 100% by Letzelter *et al.* (1987), the corresponding predissociation rates have been estimated (see eq. [1]). The corresponding total inverse lifetimes $A = A^{rad} + k^{pr}$ are included in Table 1. The total lifetimes for most bands are uncertain by factors of at least 5, and differ by up to an order of magnitude in either direction from those adopted by Viala *et al.* (1988). Note that the photodissociation of CO differs significantly from that of H_2 in the aspect of line widths. The photodissociation of H_2 also takes place by discrete absorptions, but these are followed by spontaneous emission from the excited electronic states into the vibrational continuum of the ground electronic state, rather than by pre-

dissociation. The widths characterizing the H_2 photodissociation transitions are thus determined by the radiative lifetimes of the upper levels, which are typically 10^8–10^9 s^{-1}, i.e., orders of magnitude smaller than the widths characterizing most CO predissociating lines.

Although most of the higher lying states of CO appear to be strongly predissociated, the electronic states causing the predissociation and the coupling mechanisms have not yet been identified. In addition, most experiments have been performed at room temperature where a broad distribution of population over rotational levels exists. In interstellar clouds, most of the CO molecules reside in the lowest few rotational levels, so that the dissociating absorptions will involve only the lowest rotational levels of the upper electronic states. It still remains to be established whether the predissociations for the lower levels are as rapid as they appear to be for the higher levels, as is assumed in this work. Various singlet and triplet states that are known to be repulsive in the Franck–Condon region and/or that correlate with ground state $C(^3P)$ and $O(^3P)$, such as the $I\ ^1\Sigma^-$, $E\ ^1\Pi$, $D\ ^1\Delta$, $e\ ^3\Sigma^-$, $d\ ^3\Delta$, and $a'\ ^3\Sigma^+$ states, may play a role through spin-orbit coupling and radial and rotational nuclear interactions. If the predissociations occur mostly by spin-orbit or radial nuclear couplings, the lower levels are expected to be rapidly predissociated as well. If, however, rotational nuclear interactions dominated, the rates for the low rotational levels would be orders of magnitude less than those for the higher levels, since the strength of these interactions scales with J^2.

The $E\ ^1\Pi$–$X\ ^1\Sigma^+$ and $C\ ^1\Sigma^+$–$X\ ^1\Sigma^+$ bands require a special discussion. Although the experiments of Lee and Guest (1981) indicated that these bands are fully predissociated, fluorescence from the $C\ ^1\Sigma^+$ $v' = 1$ level was easily detected by Eidelsberg *et al.* (1984), and weak fluorescence from the $E\ ^1\Pi$ $v' = 0$ state was detected by Letzelter *et al.* (1987). The fluorescence yields suggest predissociation probabilities of $\sim$0.6 and 0.9, respectively. These estimates apply again to a distribution over rotational levels. Since the predissociation and radiative rates are of comparable magnitudes for these bands, small changes in the predissociation rates with rotational level can significantly affect the values of $\eta_{v'J'}$. The oscillator strength for the E–X transition is large, and it occurs at the longest wavelength where the intensity of the radiation field is largest. In addition, the E–X (1, 0) band plays an important role in the photodissociation of the isotopic species. Accurate determination of the predissociation rates and probabilities for the low J levels of both the E–X (0, 0) and (1, 0) bands is therefore very important.

The oscillator strengths and predissociation probabilities for bands of the isotopic species were taken to be the same as those for ^{12}CO. This assumption is expected to be accurate for the oscillator strengths for most bands. The predissociation probabilities for the upper levels of the isotopes may differ, however, especially for levels involving a nonzero vibrational quantum number.

III. DEPTH-DEPENDENT PHOTODISSOCIATION OF CO

a) Unshielded Photodissociation Rate

The photodissociation rate of CO by absorption into an upper state u from a lower level l with fractional population x_l in a radiation field with mean intensity I in photons cm^{-2} s^{-1} $Å^{-1}$ is given by

$$k_{ul}^{pd} = \frac{\pi e^2}{mc^2} f_{ul} \eta_u \lambda_{ul}^2 x_l I(\lambda_{ul})\ s^{-1}\ , \qquad (2)$$

where $\pi e^2/mc^2$ takes the numerical value 8.85×10^{-21} if λ is in Å. The total rate k^{pd} is obtained by summing over all possible lines and initial levels. The intensity of the unattenuated interstellar radiation field in the solar neighborhood has been determined by Habing (1968), Jura (1974), Draine (1978), Gondhalekar, Phillips, and Wilson (1980; hereafter GPW), and Mathis, Mezger, and Panagia (1983; hereafter MMP). The various estimates in the 912–2000 Å wavelength region are illustrated in Figure 1; in the relevant wavelength range 912–1100 Å, they differ by up to a factor of 2. If the Draine (1978) radiation field is employed, the unattenuated rate is $k^{pd} = 2.0 \times 10^{-10}\ s^{-1}$. The rates in the GPW and MMP radiation fields are 1.6×10^{-10} and $1.8 \times 10^{-10}\ s^{-1}$, respectively. The unshielded rate is at least an order of magnitude larger than that used in previous models (e.g., Solomon and Klemperer 1972; Federman *et al.* 1980; Glassgold *et al.* 1985).

b) Depth-dependent Photodissociation Rates

The depth dependence of the absorption rate in each line is controlled by several effects:

1) Self-shielding, i.e., the growth toward saturation of the absorption in the line itself with increasing depth and column density;

2) Mutual shielding, i.e., the blending of lines of the isotopic species with those in the same band of the more abundant ^{12}CO molecule;

3) The shielding by coincident lines of H and H_2;

4) The attenuation of radiation by dust particles and carbon atoms.

As in van Dishoeck and Black (1986*a*), the line and continuum attenuations are assumed to be separable. In order to account for effects 1–3, the full absorption spectrum—consisting of 3496 lines of the four isotopic forms of CO, and of H and H_2—is simulated in the wavelength interval $\lambda =$ 912–1077 Å at each depth into the cloud. All lines arising in rotational levels $J'' = 0$–9 of the CO $X\ ^1\Sigma^+$, $v'' = 0$ state and its isotopes are included, as well as all lines of H_2 arising in $X\ ^1\Sigma_g^+$ $v'' = 0$, $J'' = 0$–7 and the first 50 lines of the Lyman series of H. The attenuation of radiation at every wavelength and the absorption rate in every line are computed numerically directly from this simulated spectrum at each depth. A model is typically divided into 50 depth steps to the center of the cloud, and is assumed to have a plane-parallel geometry. Most models are illuminated on both sides with half the intensity of the unattenuated radiation field so that the boundary rate with the Draine radiation field is $\sim 1 \times 10^{-10}\ s^{-1}$. The profile of each line is taken to be a Voigt function. The Doppler widths of the CO lines are usually taken to be small, $b \approx 0.5$ km s^{-1}. Note that for the strongly predissociated transitions, the predissociation probabilities of 10^{11}–$10^{12}\ s^{-1}$ correspond to natural widths of 2–20 km s^{-1} in Doppler velocity units, i.e., much larger than the thermal and turbulent widths in quiescent interstellar clouds. The population distribution of CO and its isotopes over the rotational levels is assumed to be characterized by a single excitation temperature T_{ex}. The CO, H, and H_2 concentrations and cumulative column densities to the near and far boundaries of the cloud are computed at each depth.

The continuum attenuation by dust (effect 4) depends on the extinction curve, the albedo ω_λ, and the scattering phase function g_λ of the grains, only the first of which is sometimes known in the 912–1100 Å range. Grain models 2 and 3 of Roberge, Dalgarno, and Flannery (1981), which have $\omega \approx 0.6$ and 0.8, and $g \approx 0.5$ and 1.0 at $\lambda = 1000$ Å, respectively, have been employed in this work. If the continuum attenuation is

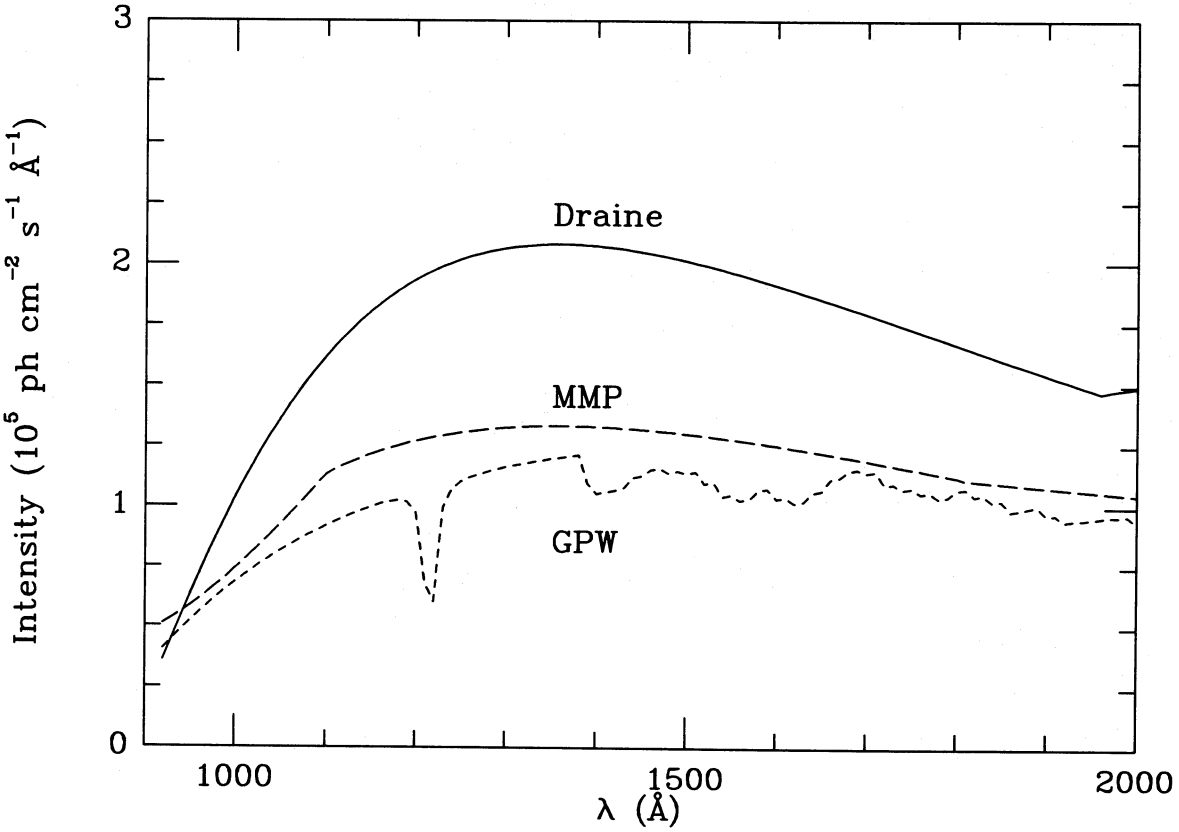

FIG. 1.—Variation of the intensity of the ultraviolet interstellar radiation field with wavelength as given by Draine (1978) (*full line*), Mathis *et al.* (1983) (*long-dashed line*), and Gondhalekar *et al.* (1980) (*short-dashed line*).

characterized by a wavelength-dependent exponential decay exp $(-s_\lambda \tau_\lambda)$, the models 2 and 3 correspond to exponents s_λ of 3 and 0.8 at $\lambda = 1000$ Å, respectively. This range of exponents covers that suggested by the more recent grain models of Draine and Lee (1984) and Chlewicki and Greenberg (1984*a*, *b*).

c) *Results*

The radiative transfer effects are illustrated in Figures 2 and 3, which contain two small portions of the simulated absorption. These figures represent the absorption that would be produced by CO and by H and H_2 at the center of a diffuse interstellar cloud such as that towards ζ Oph. The CO excitation temperature is taken to be $T_{ex} = 4$ K as inferred from the ultraviolet observations of Wannier, Penzias, and Jenkins (1982), which implies that only levels $J'' = 0$–3 are appreciably populated. The adopted Doppler parameters are $b = 5.0$, 3.0, and 0.3 km s^{-1} for lines of H, H_2, and CO, respectively, based on the Copernicus results for H and H_2 (Morton 1975; Spitzer and Morton 1976), and the CO millimeter emission-line observations of Langer, Glassgold, and Wilson (1987). Figure 2 shows the spectrum in the region of the CO E–X (0, 0) and C–X (1, 0) bands. It is clear that the C–X (1, 0) band at 1063 Å is coincident with a strong feature of H_2, and is thus completely shielded by it (Glassgold *et al.* 1985). The E–X (0, 0) band at 1076 Å, on the other hand, is only partly shielded. Figure 3 illustrates the spectrum around 940 Å where a strong $^1\Sigma^+$–X $^1\Sigma^+$ transition occurs at 940 Å and a $^1\Pi$–X $^1\Sigma^+$ transition at 941.2 Å. Note that the rotational structure of the 940 Å band is indistinct owing to the large predissociation width. The 941.2 Å band is rotationally resolved and is relatively free of overlaps with H and H_2. Since we identify the upper state of the 941.2 Å band as one of nonzero vibrational quantum number, the lines of the isotopic species in this band are well shifted from those of ^{12}CO. The weak band at 941.8 Å in Figure 3 is the counterpart in ^{13}CO of the 941.2 Å ^{12}CO band. The new spectra of Stark *et al.* (1988) confirm the adopted ^{13}CO shift for this band. The full simulated spectrum in the 912–1100 Å range is presented in reduced form in Figure 4. Table 2 lists the individual contributions to the total CO photodissociation rate of the most important bands, both at the edge of the cloud and at the center. It is seen that the contributions from some bands that are important at the edge become completely negligible inside the cloud due to shielding by H and H_2. This shielding can be significant at depths corresponding to a visual extinction A_V of only 0.1 mag. Coincidences between CO lines and strong resonance lines of abundant atomic species and of HD have been checked: no other shielding species of any consequence have been found. The total photodissociation rate of CO clearly results from contributions of many different transitions, with the E–X (0, 0) transition dominating only at the edge of the cloud.

The depth-dependent photodissociation rates of CO and the isotopic species are presented in Figures 5 and 6 for two different model clouds (see § IV). The first model, illustrated in Figure 5, represents a translucent cloud with a total visual extinction $A_V^{tot} = 5.2$ mag, a density $n_H = n(H) + 2n(H_2) = 1000$ cm^{-3} and a temperature of 15 K (model T6 of Table 7).

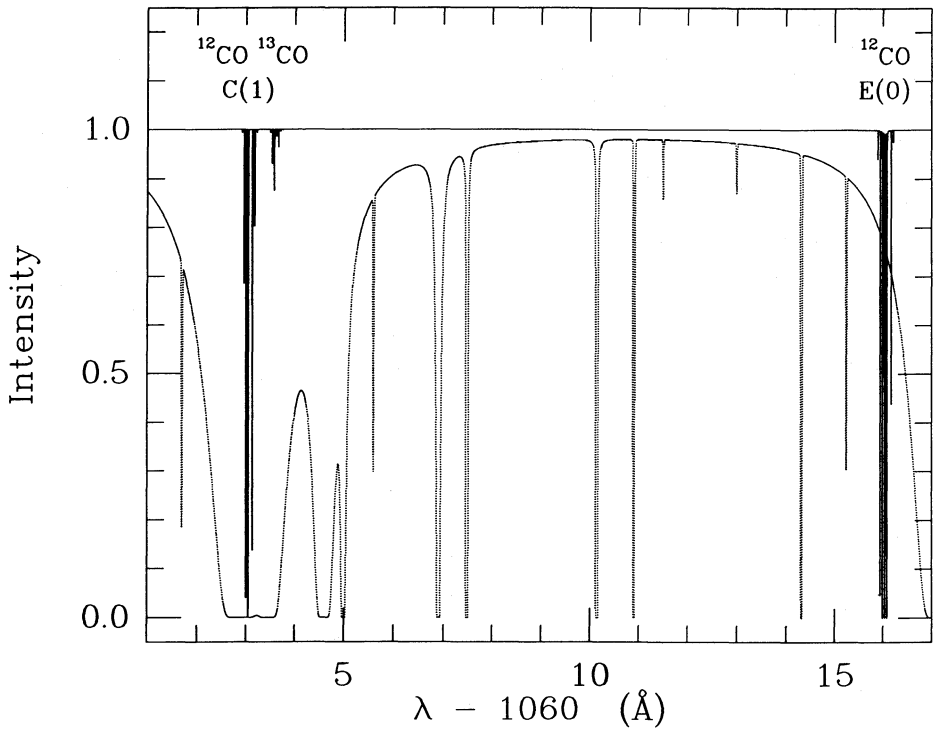

FIG. 2.—Simulated line absorption at the center of the ζ Oph diffuse cloud for the interval $\lambda = 1061$–1077 Å at a resolution of 0.001 Å. The absorptions due to CO (*solid curve*) and H and H_2 (*dotted curve*) are plotted separately. The adopted column densities to the center are half the observed values: 2.6×10^{20}, 2.1×10^{20}, 1.0×10^{15}, and 1.8×10^{13} cm^{-2} for H, H_2, CO, and ^{13}CO, respectively. The $C^{18}O$ and $^{13}C^{18}O$ column densities are assumed to be 2.0×10^{12} and 3.6×10^{10} cm^{-2}, respectively. The Doppler parameters are $b = 5.0$, 3.0, and 0.3 km s^{-1} for lines of H, H_2, and CO, respectively. The adopted CO excitation temperature $T_{ex} = 4$ K.

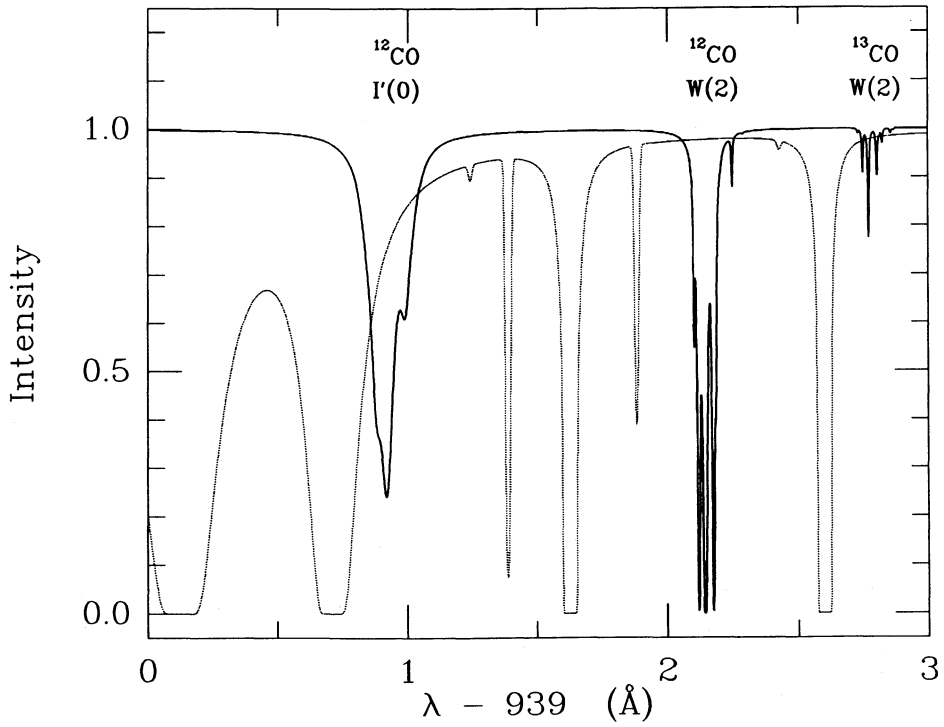

FIG. 3.—Simulated absorption of CO, H, and H_2 at the center of the ζ Oph diffuse cloud as in Fig. 2, but for the interval $\lambda = 939$–942 Å

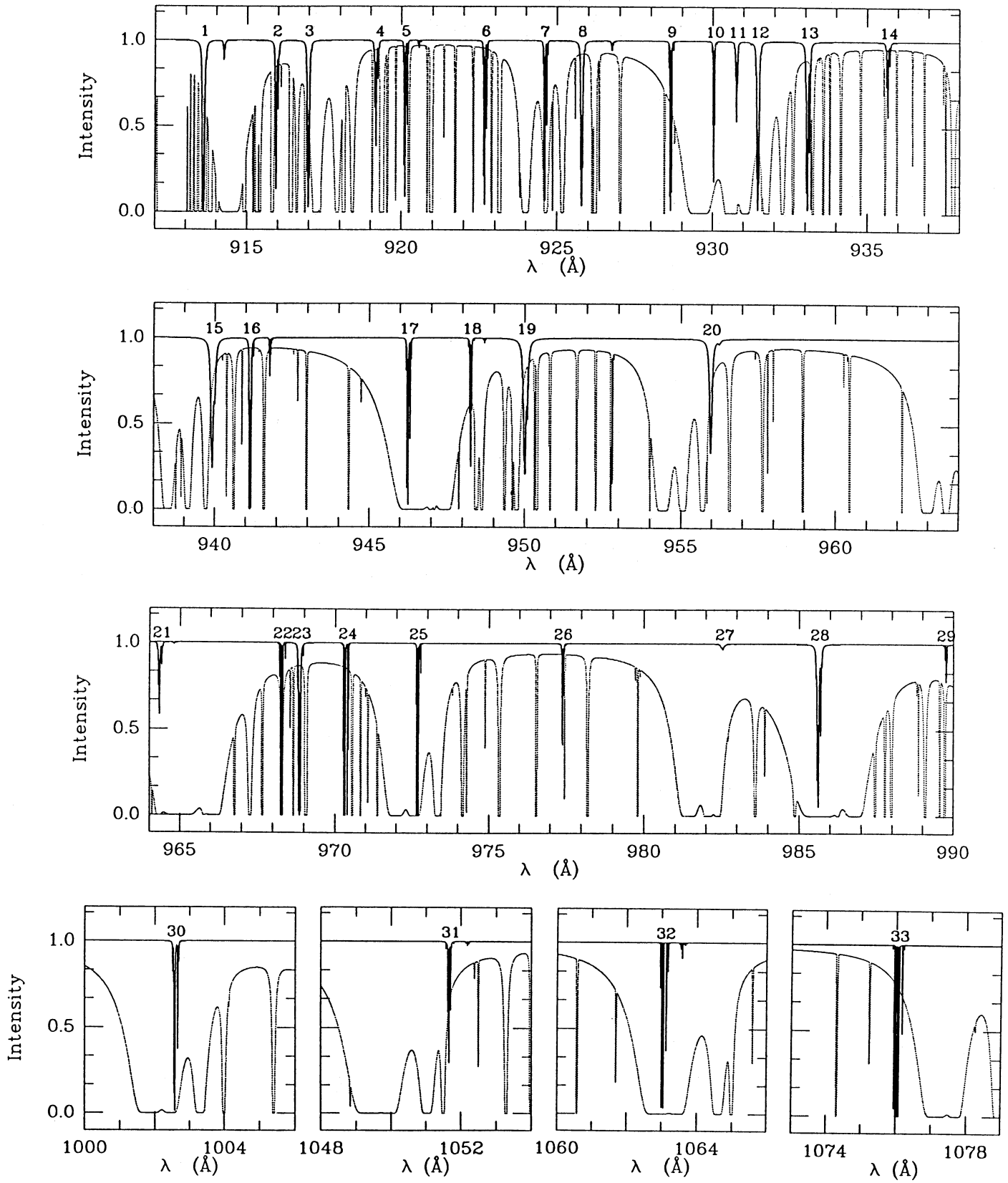

FIG. 4.—Simulated absorption spectra of CO, H, and H_2 at the center of the ζ Oph diffuse cloud over the complete wavelength range 912–1077 Å. All CO bands are labeled by the index number of Table 1.

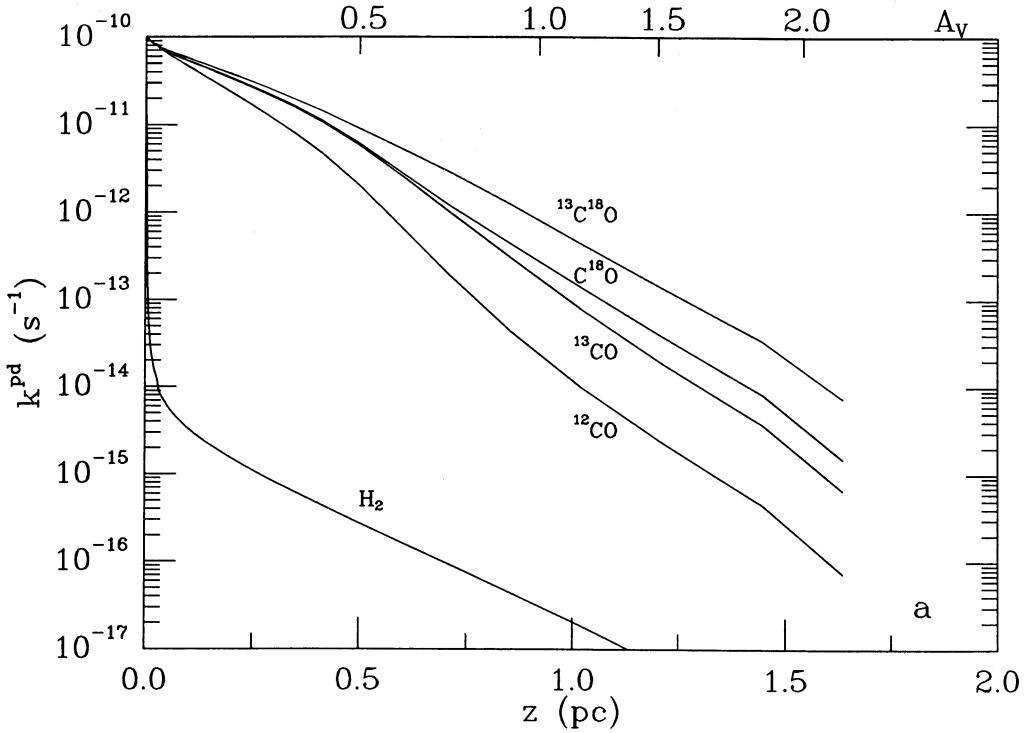

FIG. 5a

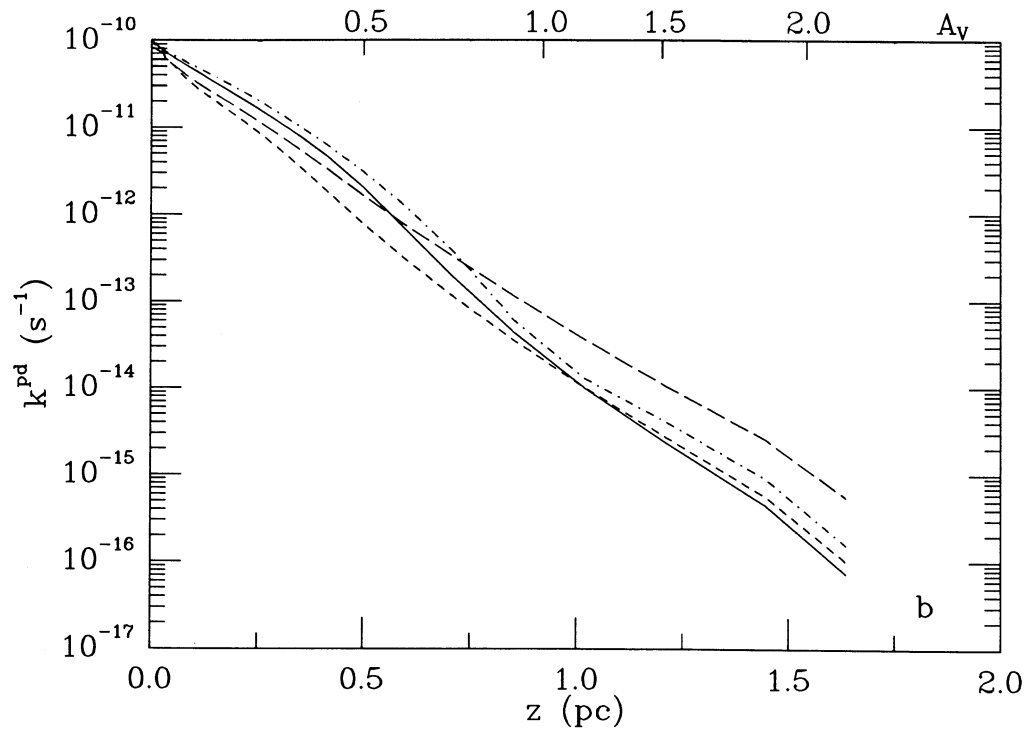

FIG. 5b

FIG. 5.—(*a*) Photodissociation rates of ^{12}CO and the isotopic varieties as functions of linear depth into translucent cloud model T6. See Table 7 for details of the model. (*b*) Photodissociation rates of ^{12}CO as functions of linear depth computed at four different levels of approximation. *Solid curve:* full calculation including self-shielding, mutual shielding, shielding by lines of H and H_2 and dust attenuation for all CO lines up to $J'' = 9$. *Short-dashed curve:* calculation including only the $R(0)$ lines of CO and H_2 lines with $J'' = 0$ and 1. *Long-dashed line:* calculation in which only self-shielding in the CO $R(0)$ lines and dust attenuation is taken into account. *Dash-dotted line:* calculation using the shielding functions presented in Table 5.

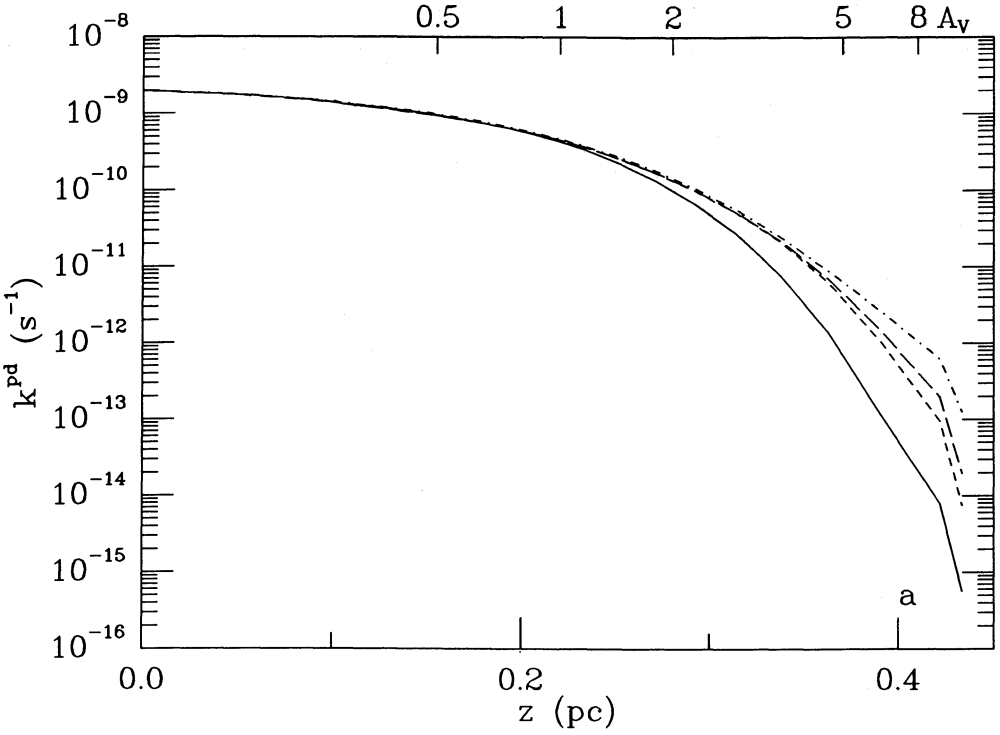

FIG. 6a

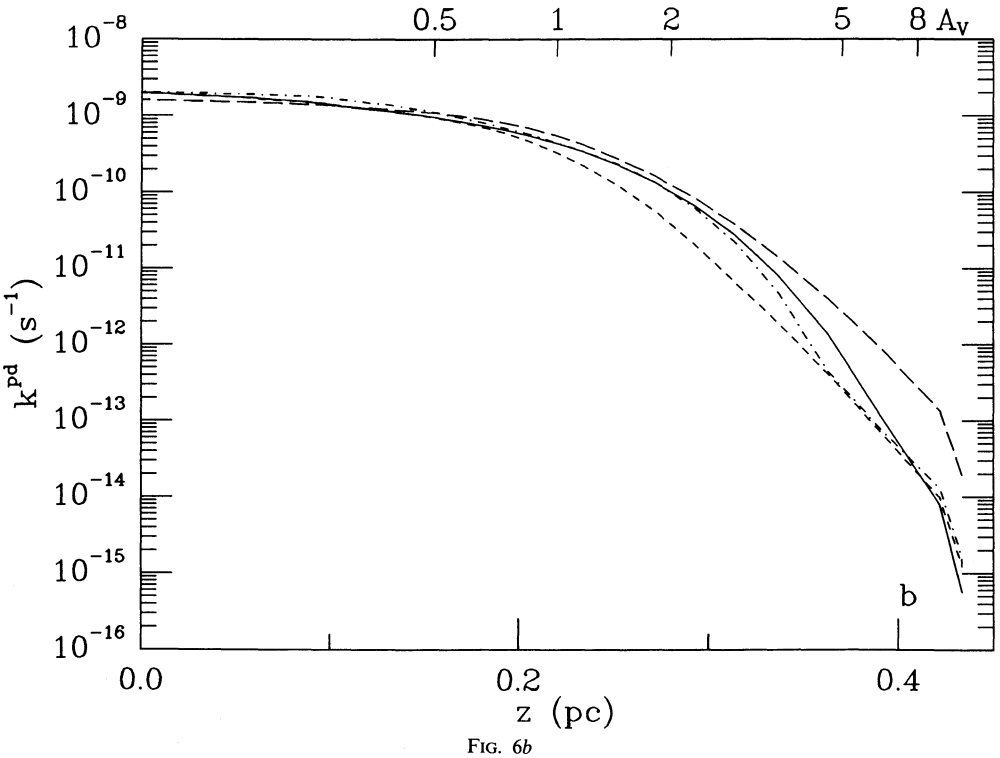

FIG. 6b

FIG. 6.—(*a*) Photodissociation rates of ^{12}CO (*full line*), ^{13}CO (*short-dashed line*), $C^{18}O$ (*long-dashed line*), and $^{13}C^{18}O$ (*dash-dotted line*) as functions of linear depth into the NGC 2024 dense cloud model. See Table 8 for details of the model. (*b*) As Fig. 5*b*, but for the dense cloud model.

TABLE 2

CONTRIBUTIONS FROM INDIVIDUAL BANDS[a] TO THE TOTAL ^{12}CO PHOTODISSOCIATION RATE

Band	λ(Å)	Edge[b]	Center[b,c]	Edge[d]	Center[c,d]
33.....	1076.1	24.8	2.9	39.9	6.9
30.....	1002.6	3.6	0.2	5.8	0.4
28.....	985.6	5.8	0.0	9.4	0.0
25.....	972.7	3.9	0.0	6.0	0.0
24.....	970.4	4.9	2.8	7.2	6.4
23.....	968.9	5.8	8.0	8.4	17.9
20.....	956.0	3.8	10.2	3.9	16.4
19.....	950.0	5.4	13.8	4.2	16.8
16.....	941.2	5.5	5.9	1.6	2.7
15.....	940.0	4.3	10.5	0.9	3.6
13.....	933.1	3.6	7.1	0.0	0.0
12.....	931.5	3.5	2.4	0.0	0.0
8.....	925.8	2.5	5.2	0.0	0.0
1.....	913.6	3.7	1.6	0.0	0.0

[a] In percent.
[b] Using the Draine 1978 radiation field.
[c] At the center of a diffuse cloud with $N(CO) = 10^{15}$ cm^{-2}, $N(H) = 2.6 \times 10^{20}$ cm^{-2}, and $N(H_2) = 2.1 \times 10^{20}$ cm^{-2}, see the legend to Fig. 2.
[d] Using the modified Draine 1978 radiation field; see the discussion of § IV*a*.

The model is exposed to the normal interstellar radiation field (Draine 1978), and uses grain model 2 of Roberge *et al.* (1981). The second model, presented in Figure 6, is for a typical dense cloud with $A_V^{tot} = 16.8$ mag, a total density that varies with depth from 700 cm^{-3} at the boundary to 3×10^4 cm^{-3} at the center, and a central temperature of 40 K. The radiation field in this case is enhanced by a factor $I_{UV} = 20$ with respect to the average background starlight, and employs grain model 3. This model was developed specifically for the NGC 2024 region in the direction of IRS 2 (see Table 8). In Figures 5*a* and 6*a*, variations of the photodissociation rates of the isotopic varieties with depth are displayed. The rates for the isotopic species are larger than that for ^{12}CO inside the clouds owing to the smaller self-shielding of the isotopic species, and because some of their lines are shifted enough from those of ^{12}CO that mutual shielding is not significant. The depth at which the rates of the various isotopes start to differ depends on the strength of the incident radiation field. Figure 5*a* also includes the H_2 photodissociation rate as a function of depth into the cloud. It is evident that the H_2 self-shielding becomes important at much smaller depths than the CO self-shielding, owing to the larger abundance of H_2. The CO photodissociation also shows a much more gradual decrease with depth into the cloud than does the H_2 rate for several reasons. First, at the depth where the onset of CO self-shielding occurs, the dust extinction is already significant. Second, much of the shielding of CO by H and H_2 saturates at small depths and thus does not grow rapidly with greater increasing depth. Third, most of the dissociating lines of CO have natural widths that are much larger than the widths (Doppler plus natural) of the self-shielding lines in H_2.

TABLE 3

PHOTODISSOCIATION RATES[a] OF CO AND ITS ISOTOPES

	Translucent Cloud[b]		Dense Cloud[b]	
Species	Edge	Center	Edge	Center
^{12}CO	1.0(−10)	3.4(−17)	2.0(−9)	5.7(−16)
^{13}CO	1.0(−10)	2.6(−16)	2.0(−9)	7.5(−15)
$C^{18}O$	1.0(−10)	6.2(−16)	2.0(−9)	2.0(−14)
$^{13}C^{18}O$ ...	1.0(−10)	3.5(−15)	2.0(−9)	1.3(−13)

[a] In s^{-1}.
[b] See text for description of models. The Draine 1978 radiation field is employed throughout.

Table 3 lists the photodissociation rates of the isotopic species in the centers of the two clouds. The ^{13}CO and $C^{18}O$ rates are larger by factors of 6–20 than those for ^{12}CO, while the $^{13}C^{18}O$ rates are more than two orders of magnitude larger. It is thus evident that self-shielding does reduce the ^{12}CO rate significantly. In Table 4, the bands for which the isotope-selective effects are largest are presented. As expected, the list includes most bands to which we have assigned a nonzero upper state vibrational quantum number. It appears that the *E–X* (1, 0) band at 1051 Å and the band at 941.2 Å are most effective in the isotope-specific photodissociation. Surprisingly, the *E–X* (0, 0) band also contributes slightly. Although the lines of the isotopes are shifted by only 2–4 km s^{-1} from those of ^{12}CO in this band, the natural widths are small enough that no significant overlap occurs for Doppler parameters $b < 2$ km s^{-1}. More accurate determinations of the predissociation probabilities for the low rotational levels of the E $v' = 0$ and 1 states are therefore of paramount importance. The *C–X* (1, 0) band plays almost no role in the isotope-

TABLE 4

ISOTOPE-SELECTIVE PHOTODISSOCIATION EFFECTS FOR INDIVIDUAL BANDS[a]

			^{13}CO		$C^{18}O$		$^{13}C^{18}O$	
Band	λ (Å)	v'	Percent of Rate	Ratio[b]	Percent of Rate	Ratio[b]	Percent of Rate	Ratio[b]
33.....	1076.1	0	2	3	3	10	11	196
31.....	1051.7	1	63	47	58	100	39	375
29.....	989.8	0	1	2	<1	2	<1	3
24.....	970.4	0	1	2	<1	2	<1	3
20.....	956.0	1	4	3	2	3	4	27
18.....	948.3	1	1	51	1	178	1	469
16.....	941.2	2	9	11	15	40	38	578
8.....	925.8	3	5	14	9	56	4	152
5.....	920.1	1	6	22	7	62	3	141

[a] The calculations refer to the center of the translucent cloud model.
[b] Ratio of photodissociation rate of isotopic species with respect to that of ^{12}CO through the same band.

selective photodissociation, because it is completely shielded by H_2. If the ^{13}CO shifts measured by Stark *et al.* (1988) are adopted, other bands, such as Nos. 26, 23, 22, and 13, also contribute to the isotope-selective photodissociation. Consequently, the central ^{13}CO rates in the translucent cloud model are increased by $\sim 50\%$. However, these differences have only minor effects on the computed column densities, as will be shown in § IV*b*.

Figures 5*b* and 6*b* illustrate the sensitivity of the rate to the amount of detail included in the calculation. The ^{12}CO photodissociation rates are shown as functions of linear depth at three different levels of approximation. The full curve refers to the complete calculation that includes self-shielding in all CO lines with $J'' < 10$, mutual shielding in all lines of the isotopic varieties of CO, shielding by H and all lines of H_2 with $J'' < 8$, and attenuation by dust. The next level of approximation (*short-dashed curve*) treats the above effects, but only for the $R(0)$ lines of CO and its isotopes and for H_2 lines with $J'' = 0$ and 1. The crudest approximation (*long-dashed curve*) neglects the H and H_2 shielding and incorporates attenuation by dust and self-shielding in the $R(0)$ lines of CO only in the manner described for H_2 by van Dishoeck and Black (1986*a*); i.e., the absorption at each depth in each line is simply proportional to the slope of the curve of growth. Only those bands (24 out of the total 33) which do not significantly overlap with any H or H_2 line are taken into account in this last calculation. It is clear from these figures that representing the CO photodissociation as though it occurs through a single line in each band can lead to an order of magnitude error in the rate at some depths. As we will see below, however, the approximation affects the total column densities only at the level of a factor of 2 or less, depending upon the total thickness of the cloud.

There are several other parameters in the calculations that affect the depth dependence of the CO photodissociation rate. If the CO excitation temperature is larger, the populations will be distributed over more rotational levels so that the lines become optically thick slightly deeper into the cloud. Similarly, if the predissociation probabilities of the higher levels were underestimated by an order of magnitude, the photodissociation rates would be increased inside the clouds. This effect has been demonstrated clearly in Figure 1 of Viala *et al.* (1988). Both changes influence the overall CO photodissociation rates and column densities at the level of 10% or less, however. Increase of the Doppler parameter b from 0.5 to 5 km s^{-1} has negligible effect on the CO photodissociation rates, because the natural widths of most lines are larger than the Doppler widths. Decrease of the Doppler parameters for H and H_2 to less than 1 km s^{-1} also affects the rates by less than a few %.

d) Simple Representation of the Depth-dependent Rates

The full calculation of the depth-dependent photodissociation rates is very costly in terms of computing time; therefore, time-saving approximations may be valuable for some—but not all—applications. Two approaches to simplification have already been discussed and illustrated in the preceding sections. A third, preferred simplification for cloud modeling is to determine a shielding function $\Theta[N(CO), N(H_2)]$ by interpolation within a two-dimensional matrix of precomputed shielding factors for each isotopic species at each depth. The total photodissociation rate of isotopic species i is then

$$k_i = k_{i0}\,\Theta_i[N(CO), N(H_2)]\theta_c(\bar{\lambda}, A_V)\,, \qquad (3)$$

where k_{i0} is the appropriate boundary rate and θ_c is the continuum attenuation function due to extinction by dust (see van Dishoeck and Black 1986*a*). The shielding function Θ_i depends primarily on the column densities of CO and H_2 for a given, constant isotope abundance ratio. The tables used to determine Θ_i are computed in the detailed scheme once for a grid of values of $N(H_2)$ and $N(CO)$, all the other parameters being fixed at "typical" values. These other parameters are the Doppler broadening parameters for CO, H_2, and H lines, the atomic column density, the external radiation field, and the rotational excitation temperatures T_{ex} of CO and H_2. The results are relatively insensitive to the values of these secondary parameters over a wide range of interstellar conditions. In any case, an appropriate set of tables of Θ_i could be prepared for a specific class of models: e.g., hot photodissociation regions would require higher excitation temperatures and larger Doppler parameters. Fixing $N(H) \approx 5 \times 10^{20}$ cm^{-2} seems realistic in that the atomic column density is likely to be within a factor of 3 of this value for most clouds that have $A_V > 0.1$ mag and for depths where CO is abundant. This approximation technique reproduces quite well the photodissociation rate of ^{12}CO once the table has been constructed (see Figs. 5*b* and 6*b*). Column densities of ^{12}CO computed with the shielding functions (eq. [3]) agree with those computed through the full-rate calculation within 10% in models of translucent clouds like that of Figure 5. The corresponding tables of Θ_i for the rarer isotopic species depend on the column density of $^{12}C^{16}O$ and are computed for fixed ratios of the isotope abundances at all depths. As a result, the dissociation rates and abundances of the rarer varieties of CO will deviate from the results of the full calculations, particularly at depths where fractionation effects are most important (see § IV*b*[ii]). On the other hand, the total column densities of the isotopic species derived from the approximate calculation are within 20%–30% of the results of the full calculation in many cases.

In order to provide a widely usable distillation of the dissociation rate computation, we provide in Table 5 an example of the shielding factor matrices that should be applicable to cool ($T \lesssim 100$) interstellar regions ranging from diffuse clouds to thick, dark clouds. The values of the secondary parameters are indicated in the note to the table. Interpolation through two-dimensional cubic splines works well. In equation (3), the continuous attenuation θ_c depends on a characteristic wavelength

$$\bar{\lambda} = (5675.) - 200.6w) - (571.6 - 24.09w)u + (18.22 - 0.7664w)u^2 \text{ (Å)} \qquad (4)$$

that varies with the column depths $u = \log N(CO)$ and $w = \log N(H_2)$ and that represents the mean of the wavelengths of the 33 dissociating bands weighted by their fractional contributions to the total rate at each depth.

Table 5 is also useful as an illustration of the relative effects of shielding by H_2 and by CO. On considerations of element abundances, most interstellar clouds will satisfy the condition $N(CO) < 10^{-3}N(H_2)$; therefore, the entries in Table 5 that violate this constraint are present only to permit accurate interpolation elsewhere in parameter space.

The gradual decrease of the CO photodissociation rates with depth, as illustrated in Figures 5 and 6, raises the question whether they could also be represented well by a single exponential decay. Although such a fit may be quite accurate for individual cases, the resulting exponents depend sensitively on the total thickness of the cloud, the adopted grain model, and

TABLE 5

SHIELDING FUNCTIONS $\Theta[N(CO), N(H_2)]$[a]

log $N(H_2)$	log N(CO) 0	13	14	15	16	17	18	19
^{12}CO: Unattenuated Rate[b] $k_{i0} = 2.039 \times 10^{-10} I_{UV}$ s^{-1}								
0.....	1.000	9.681(−1)	7.764(−1)	3.631(−1)	7.013(−2)	1.295(−2)	1.738(−3)	9.985(−5)
19.....	8.215(−1)	7.916(−1)	6.160(−1)	2.749(−1)	5.351(−2)	1.065(−2)	1.519(−3)	8.818(−5)
20.....	7.160(−1)	6.900(−1)	5.360(−1)	2.359(−1)	4.416(−2)	8.769(−3)	1.254(−3)	7.558(−5)
21.....	3.500(−1)	3.415(−1)	2.863(−1)	1.360(−1)	2.500(−2)	4.983(−3)	7.151(−4)	3.796(−5)
22.....	4.973(−2)	4.877(−2)	4.296(−2)	2.110(−2)	4.958(−3)	9.245(−4)	1.745(−4)	8.377(−6)
23.....	1.310(−4)	1.293(−4)	1.160(−4)	6.346(−5)	1.822(−5)	6.842(−6)	3.622(−6)	3.572(−7)
^{13}CO: Unattenuated Rate[b] $k_{i0} = 2.034 \times 10^{-10} I_{UV}$ s^{-1}								
0.....	1.000	9.887(−1)	9.159(−1)	6.485(−1)	2.610(−1)	6.032(−2)	7.788(−3)	3.402(−4)
19.....	8.181(−1)	8.083(−1)	7.463(−1)	5.324(−1)	2.185(−1)	4.961(−2)	6.431(−3)	2.859(−4)
20.....	7.011(−1)	6.922(−1)	6.386(−1)	4.540(−1)	1.835(−1)	4.160(−2)	5.556(−3)	2.404(−4)
21.....	3.599(−1)	3.573(−1)	3.392(−1)	2.585(−1)	1.202(−1)	2.767(−2)	3.389(−3)	1.346(−4)
22.....	6.037(−2)	5.993(−2)	5.929(−2)	5.423(−2)	3.320(−2)	6.691(−3)	7.129(−4)	1.858(−5)
23.....	8.019(−4)	8.014(−4)	7.979(−4)	7.640(−4)	5.197(−4)	1.115(−4)	1.500(−5)	6.254(−7)
$C^{18}O$: Unattenuated Rate[b] $k_{i0} = 2.035 \times 10^{-10} I_{UV}$ s^{-1}								
0.....	1.000	9.897(−1)	9.243(−1)	6.673(−1)	2.921(−1)	9.464(−2)	1.451(−3)	7.450(−4)
19.....	8.088(−1)	8.000(−1)	7.450(−1)	5.405(−1)	2.383(−1)	7.686(−2)	1.194(−2)	6.310(−4)
20.....	7.032(−1)	6.953(−1)	6.477(−1)	4.708(−1)	2.091(−1)	6.811(−2)	1.042(−2)	5.071(−4)
21.....	3.611(−1)	3.587(−1)	3.424(−1)	2.655(−1)	1.371(−1)	4.805(−2)	6.614(−3)	2.436(−4)
22.....	6.093(−2)	6.059(−2)	6.005(−2)	5.592(−2)	4.069(−2)	1.480(−2)	1.640(−3)	3.276(−5)
23.....	9.061(−4)	9.061(−4)	9.042(−4)	8.855(−4)	7.410(−4)	2.968(−4)	3.616(−5)	8.619(−7)
$^{13}C^{18}O$: Unattenuated Rate[b] $k_{i0} = 2.043 \times 10^{-10} I_{UV}$ s^{-1}								
0.....	1.000	9.961(−1)	9.662(−1)	7.930(−1)	5.002(−1)	2.631(−1)	8.532(−2)	1.245(−2)
19.....	8.385(−1)	8.360(−1)	8.155(−1)	6.887(−1)	4.641(−1)	2.516(−1)	8.027(−2)	1.118(−2)
20.....	7.298(−1)	7.274(−1)	7.097(−1)	6.011(−1)	4.077(−1)	2.245(−1)	7.014(−2)	8.977(−3)
21.....	3.597(−1)	3.587(−1)	3.507(−1)	2.980(−1)	2.013(−1)	1.264(−1)	4.384(−2)	5.512(−3)
22.....	6.818(−2)	6.735(−2)	6.701(−2)	6.412(−2)	5.575(−2)	4.530(−2)	1.662(−2)	8.928(−4)
23.....	2.984(−3)	2.984(−3)	2.984(−3)	2.979(−3)	2.941(−3)	2.600(−3)	9.290(−4)	1.765(−5)

[a] These shielding functions have been computed for the unmodified Draine 1978 radiation field and the following parameters: $b(CO) = 1.0$ km s^{-1}, $b(H_2) = 3.0$ km s^{-1}, $b(H) = 5.0$ km s^{-1}, $T_{ex}(H_2) = 10^{1.5}$ K, $T_{ex}(CO) = 10$ K, and $N(H) = 5 \times 10^{20}$ cm^{-2}. The fixed abundance ratios of the isotopic varieties are $^{12}C^{16}O : {}^{13}C^{16}O : {}^{12}C\,{}^{18}O : {}^{13}C^{18}O = 1 : 1/45 : 1/500 : 1/2000$. The shielding of the isotopic species is thus expressed as a function of the column density of $^{12}C^{16}O$.

[b] The unattenuated rate is the value that would apply for a cloud illuminated on one side only. For equal illumination of both sides of a finite slab, the boundary rate should be 1/2 times the listed unattenuated rate.

the isotope involved. Thus, a table of exponents as functions of the various parameters would need to be constructed. In that case, the shielding functions presented in Table 5 are as easy to adopt, and are more accurate for the important class of clouds with total thickness $A_V^{tot} = 1$–5 mag.

Mamon *et al.* (1988) have also discussed approximate treatments of the depth dependence in the context of circumstellar envelopes. They propose a simplification in which the CO photodissociation is represented by the effect of a number of identical, "characteristic" bands at a single characteristic wavelength. The effects of shielding by H_2 and H are incorporated into this approximation by reducing the number of effective bands, on the grounds that about half the dissociation rate is contributed by CO bands that lie far from any H_2 line. Inspection of Table 5 indicates that the H_2 shielding in the interstellar case indeed reduces the CO photodissociation rates by factors of 2–3 when log $N(H_2) < 10^{21}$ cm^{-2}. Thus for small column densities of H_2 and H, which may often be appropriate for circumstellar envelopes, the approach of Mamon *et al.* appears to be useful.

IV. CHEMISTRY OF CO

The detailed treatment of the photodissociation of CO and its isotopes has been incorporated into comprehensive models of the structure and chemistry of interstellar clouds (see van Dishoeck and Black 1986*a*, hereafter vDB). In these models, the abundances of H and H_2 are computed accurately at each depth into the cloud by simultaneous calculation of the formation process of H_2 on grains, its depth-dependent photodissociation by ultraviolet starlight, and its excitation by the ultraviolet fluorescence process and by inelastic and reactive collisions. The temperature and density in the models are either taken to be constant with depth into the cloud, or they are assumed to be governed by a polytropic equation of state. The models contain a detailed network of chemical reactions between the major species of the H, D, C, O, N, Cl, and metal families, as well as an extensive set of fractionation reactions involving ^{13}C and ^{18}O (see Langer *et al.* 1984). Compared with the work of vDB, the major modifications to the models have been the incorporation of the extensive treatment of the CO photodissociation (see § II and III) and the inclusion of metals

and large molecules, such as polycyclic aromatic hydrocarbons, into the chemistry (see Lepp *et al.* 1988). The network is appropriate for the chemistry in diffuse clouds, as well as for denser thicker clouds.

The parameters that enter the model calculations are the density and temperature structure of the cloud, the strength of the incident radiation field, the optical properties of the grains, and the gas-phase elemental abundances. For our purposes, the gas phase carbon abundance $[^{12}C] = 4.68 \times 10^{-4} \delta_C n_H$ and oxygen abundance $[^{16}O] = 8.3 \times 10^{-4} \delta_O n_H$, together with the adopted isotope ratios $[^{12}C]/[^{13}C] = 45$ (Hawkins and Jura 1987) and $[^{16}O]/[^{18}O] = 500$, are most important. In most of the models presented here, we have not included large molecules (LMs) in the chemistry. The inclusion of LMs influences the ionization balance in the cloud. Specifically, if $\sim 1\%$ of the overall carbon abundance were in the form of large molecules containing 50 carbon atoms each, corresponding to an abundance $x_{LM} = n(LM)/n_H \approx 10^{-7}$, the atomic carbon column densities would be enhanced by $\sim 20\%$. The CO column densities are not significantly affected, however, for LM abundances up to 10^{-6}.

In the following sections, we will discuss the influence of the new CO photodissociation rates on the column densities of CO and its isotopes for diffuse clouds, translucent clouds, and dense photodissociation regions. The interesting case of metal-poor clouds will be discussed separately by Maloney, Black, and van Dishoeck (1988). Most of the models presented in §§ IV*a–e* do not employ the full calculation of the CO photodissociation rate, but use the approximation in which only the $R(0)$ lines of CO and the lines of H_2 with $J'' = 0$ and 1 are taken into account. As demonstrated in Figures 5 and 6, this approximation can affect the CO photodissociation rate at some depths by up to an order of magnitude. However, the column densities of CO and the related species C and C^+ are affected by factors of 2 or less, and the relative CO, ^{13}CO, $C^{18}O$, and $^{13}C^{18}O$ column densities by much smaller factors. Since both the oscillator strengths for the CO photodissociation transitions and the intensity of the background ultraviolet radiation field between 912 and 1100 Å are still uncertain by factors of at least 2, this approximation is justified in the present models, and leads to considerable computational savings.

a) Diffuse Clouds

Detailed models which reproduce a multitude of observational data for the diffuse clouds in front of the stars ζ Oph, ζ Per, χ Oph, and *o* Per have been developed by vDB. The physical conditions in these clouds have been constrained by observational data on the H_2 and C_2 rotational excitations, the H/H_2 abundance ratio, and the atomic fine-structure populations. The inferred central temperatures, $T \approx 30$ K, and central densities, $n_H \approx 250$–800 cm^{-3}, are uncertain by up to a factor of 2, as is the scaling factor for the ultraviolet radiation field, $I_{UV} \approx 2$–4 (van Dishoeck and Black 1988*a*). The uncertainties in the physical parameters directly affect the calculated CO abundances in the models. The resulting CO column densities with the new photodissociation rates are presented in Table 6 for the ζ Oph and ζ Per clouds, where they are compared with the results obtained by vDB. Other minor changes in the chemistry that affect the CO abundance slightly are enhanced rates at low temperature for the reactions of C^+ with OH and H_2O. It appears that the new CO column densities differ by only factors of 3 from the old results. This is due to the fact that vDB included already a quite detailed treatment of the self-shielding and mutual shielding in the photodissociation of CO and its isotopes through a number of ultraviolet transitions, although they did not consider shielding by lines of H and H_2. The unshielded CO photodissociation rate adopted by vDB was a factor of 4 smaller than the value obtained here, but the decrease of the rate with depth into the cloud was less rapid compared with the new results due to the neglect of the H and H_2 shielding.

The new results therefore support the conclusion of vDB that the current steady state models of diffuse clouds fail to

TABLE 6

COMPUTED COLUMN DENSITIES[a] FOR DIFFUSE CLOUDS[b]

Cloud	Model	$(n_H)_0$ (cm^{-3})	T_0 (K)	A_V^{tot} (mag)	I_{UV}	δ_C	x_{LM}	C	C^+	CO	^{13}CO	$C^{18}O$
ζ Oph	G[c]	350	30	0.8	3.5	0.67	0.0	3.3(15)	4.2(17)	1.9(14)	3.4(12)	...
	G	350	30	0.8	3.5	0.67	0.0	4.4(15)	4.2(17)	8.4(13)	1.9(12)	1.1(11)
	G	350	30	0.8	3.5	0.52	0.0	2.8(15)	3.2(17)	8.2(13)	1.8(12)	1.1(11)
	G	350	30	0.8	3.5[d]	0.52	0.0	2.8(15)	3.2(17)	2.5(14)	5.3(12)	1.8(11)
	G	350	30	0.8	3.5[d]	0.21	6(−7)	3.3(15)	1.3(17)	2.0(14)	2.7(12)	1.2(11)
	Observed	.....						(3.2 ± 0.6)(15)	(1 ± 0.5:)(17)	(2.0 ± 0.5)(15)	(3.6 ± 1.0)(13)	...
ζ Per	F[c]	325	40	1.0	3.5	0.62	0.0	3.4(15)	4.4(17)	2.0(14)	3.8(12)	...
	F	325	40	1.0	3.5	0.62	0.0	4.2(15)	4.7(17)	9.1(13)	2.1(12)	1.1(11)
	F	325	40	1.0	3.5	0.50	0.0	2.9(15)	3.8(17)	8.9(13)	2.0(12)	1.1(11)
	F	325	40	1.0	3.5[d]	0.50	0.0	2.8(15)	3.8(17)	2.6(14)	5.7(12)	1.8(11)
	F	325	40	1.0	3.5[d]	0.40	1(−7)	3.1(15)	3.0(17)	2.5(15)	4.9(12)	1.7(11)
	Observed	.....						(3.3 ± 0.4)(15)	(3.0 ± 1.0)(17)	(6 ± 3)(14)	...	...
π Sco	A	75	80	0.3	1.2	0.1	0.0	3.2(13)	2.7(16)	3.9(11)	8.5(9)	7.8(8)
	A	75	80	0.3	1.2[d]	0.1	0.0	3.2(13)	2.7(16)	6.3(11)	1.4(10)	1.3(9)
	Observed	.....						(1.0 ± 0.5)(13)[e]	...	(1.2 ± 0.5)(12)[f]	...	...

[a] In cm^{-2}.
[b] See van Dishoeck and Black 1986*a* for definition of the symbols, for other parameters characterizing the models, and for references to the observations.
[c] Results of van Dishoeck and Black 1986*a*.
[d] Using the modified Draine radiation field as described in text and illustrated in Fig. 7.
[e] Jenkins and Shaya 1979.
[f] Federman *et al.* 1980, corrected for improved oscillator strength.

account for the observed amounts of CO by factors of 5–50. The CO column density derived from observations toward ζ Per is still uncertain. The column density listed in Table 6 is based on the measured equivalent widths of the C–X and E–X (0, 0) bands by Federman *et al.* (1980), using the oscillator strengths listed in Table 1 and taking saturation effects into account. The inferred value is somewhat larger than that given by vDB, and may not be significantly smaller than the observed CO column density toward ζ Oph. As a further test of the chemistry involving CO, we have developed a model of the diffuse cloud toward π Sco. This cloud has an atomic hydrogen column density $N(\mathrm{H}) \approx 5.3 \times 10^{20}$ cm^{-2} that is comparable to that of the ζ Oph and ζ Per clouds, but its molecular hydrogen column density, $N(\mathrm{H_2}) \approx 2.1 \times 10^{19}$ cm^{-2}, is a factor of 20 lower. The observed $\mathrm{H_2}$ $J'' = 0$–5 rotational population distribution and $\mathrm{H}/\mathrm{H_2}$ abundance ratio (Spitzer, Cochran, and Hirschfeld 1974; Jenkins *et al.* 1988) can be well reproduced in a model with a constant density $n_{\mathrm{H}} \approx 75$ cm^{-3}, $T \approx 80$ K, and $I_{\mathrm{UV}} \approx 1$, although the actual structure of the cloud may be more complicated (Jenkins *et al.* 1988). The atomic carbon data suggest that carbon is quite depleted in this region, $\delta_{\mathrm{C}} \approx 0.1$. The line of sight toward π Sco is of interest because it is the cloud for which the smallest CO column density has been detected to date, $N(\mathrm{CO}) \approx (1.2 \pm 0.5) \times 10^{12}$ cm^{-2} (Federman *et al.* 1980, corrected for improved oscillator strengths). This column is small enough that CO self-shielding is negligible, so that only the unattenuated rate and the subsequent shielding by H, $\mathrm{H_2}$, and dust play a role. The resulting model column density, $N(\mathrm{CO}) \approx 4 \times 10^{11}$ cm^{-2} is again somewhat low compared with observations, although not by a large factor.[2]

As discussed by vDB, the main formation route of CO in diffuse clouds is through the reactions

$$\mathrm{C^+ + OH \rightarrow CO^+ + H} \quad (5)$$

$$\rightarrow \mathrm{CO + H^+}\,, \quad (6)$$

followed by

$$\mathrm{CO^+ + H_2 \rightarrow HCO^+ + H} \quad (7)$$

$$\mathrm{HCO^+ + e \rightarrow CO + H}\,. \quad (8)$$

Alternative channels through the reactions of CH and O, $\mathrm{CH_3^+}$ and O, or even $\mathrm{CH^+}$ and O have formation rates that are at best comparable to those of reactions (5)–(8). Grain surface reactions or reactions between C and $\mathrm{C^+}$ with large molecules are also unlikely to contribute significantly (van Dishoeck and Black 1988*a*; Lepp *et al.* 1988). Since the models are constructed so as to reproduce the observed $\mathrm{C^+}$ and OH column densities, or even exceed them, the formation rate of CO is not expected to be in error by more than a factor of 2.

The discrepancy between models and observations is thus most likely caused by an overestimate of the CO photodissociation rate, which is the main destruction channel of CO in diffuse clouds. Since the CO oscillator strengths are now thought to be known to a factor of 2, this implies that the intensity of the ultraviolet radiation field in the relevant wavelength region 912–1100 Å may have been overestimated in the models. The scaling factor I_{UV} is constrained principally by the rotational populations of $\mathrm{H_2}$ in levels $J'' \geq 5$. It has been argued (Draine and Katz 1986*a*, *b*; Draine 1986; Pineau des Forêts *et al.* 1986) that a substantial part of the $J'' = 5$ population could result from a magnetohydrodynamic (MHD) shock passing through the cloud. Such a shock appears necessary in any case to explain the observed $\mathrm{CH^+}$ abundances. In that case, the intensity of the radiation field could be lowered by a factor of ~ 2, which would be sufficient for some clouds, such as the ζ Per and π Sco clouds, to bring the model CO column densities into harmony with, or close to, the observed values. However, the current MHD shock models cannot maintain significant populations in the $\mathrm{H_2}$ levels $J'' = 6$ and 7. The existing observational data for these levels toward ζ Oph still require an enhancement of the radiation field $I_{\mathrm{UV}} \approx 3$, so that an arbitrary lowering of the radiation field appears not to be justified. A definite measurement of the relative importance of ultraviolet fluorescence and collisional processes in populating the $\mathrm{H_2}$ $v'' = 0$, $J'' \geq 5$ levels must await the detection of ultraviolet lines out of vibrationally excited levels of $\mathrm{H_2}$, which can only be populated by the fluorescence process (see vDB). An enhanced rate of formation of CO due to shock chemistry itself appears to be ruled out in the ζ Oph cloud where the indirect evidence for a molecular shock is fairly strong. Millimeter emission-line measurements of CO (Langer, Glassgold, and Wilson 1987) reveal a complex structure in radial velocity, but indicate no significant amount of CO in any shocked component of the right velocity and velocity dispersion implied by the presence of shocked $\mathrm{CH^+}$.

An alternative solution would be to lower the intensity of the radiation field not over the full ultraviolet wavelength range, but only at $\lambda < 980$ Å, where most of the CO photodissociation occurs. Since more than 50% of the $\mathrm{H_2}$ ultraviolet pumping rate is due to Lyman and Werner transitions at $\lambda > 980$ Å, this would affect the excited $\mathrm{H_2}$ rotational populations by a comparatively small factor. As discussed in detail in the Appendix, the shape of the interstellar ultraviolet radiation field between 912 and 1000 Å is poorly constrained observationally. Figure 7 illustrates the various estimates that have been made. Comparison of the interstellar radiation fields with the measured spectrum of the B1 star α Vir (Brune *et al.* 1979) suggests that the intensity of the former may have been overestimated at $\lambda < 950$ Å. The dotted curve in Figure 7 is a modified version of the Draine (1978) radiation field, constructed to have a slope even somewhat steeper than that of a B star at $\lambda < 975$ Å. The resulting CO column densities adopting this radiation field are included in Table 6. It appears that the observational data toward π Sco can be reproduced with this ad hoc modification, but that the models still give CO column densities for the ζ Oph and possibly the ζ Per clouds that are too low by factors of ~ 2–6. Part of the remaining discrepancy may result from the fact that the ultraviolet extinction is abnormally high in the ζ Oph and ζ Per clouds (Bless and Savage 1972). If the actual extinction curve for ζ Oph as parametrized by Fitzpatrick and Massa (1988) is adopted rather than the average curve of Seaton (1979), the CO abundances are increased by another factor of 2 (see also van Dishoeck and Black 1988*b*).

Since most of the $\mathrm{H_2}$ UV absorptions leading to dissociation occur at $\lambda < 1000$ Å, the $\mathrm{H}/\mathrm{H_2}$ abundance ratio is also affected by the modification of the radiation field. A decrease in either the density or the grain formation rate is necessary to make the models consistent with observations. The abundances of other species in the models will not be changed significantly, since their photodestruction occurs principally at $\lambda > 1000$ Å. One

[2] Reinspection of the original *Copernicus* data suggests that the uncertainty in the equivalent width is substantially larger than claimed by Federman *et al.* (1980), and that the column density may be lower by a factor of 2–3.

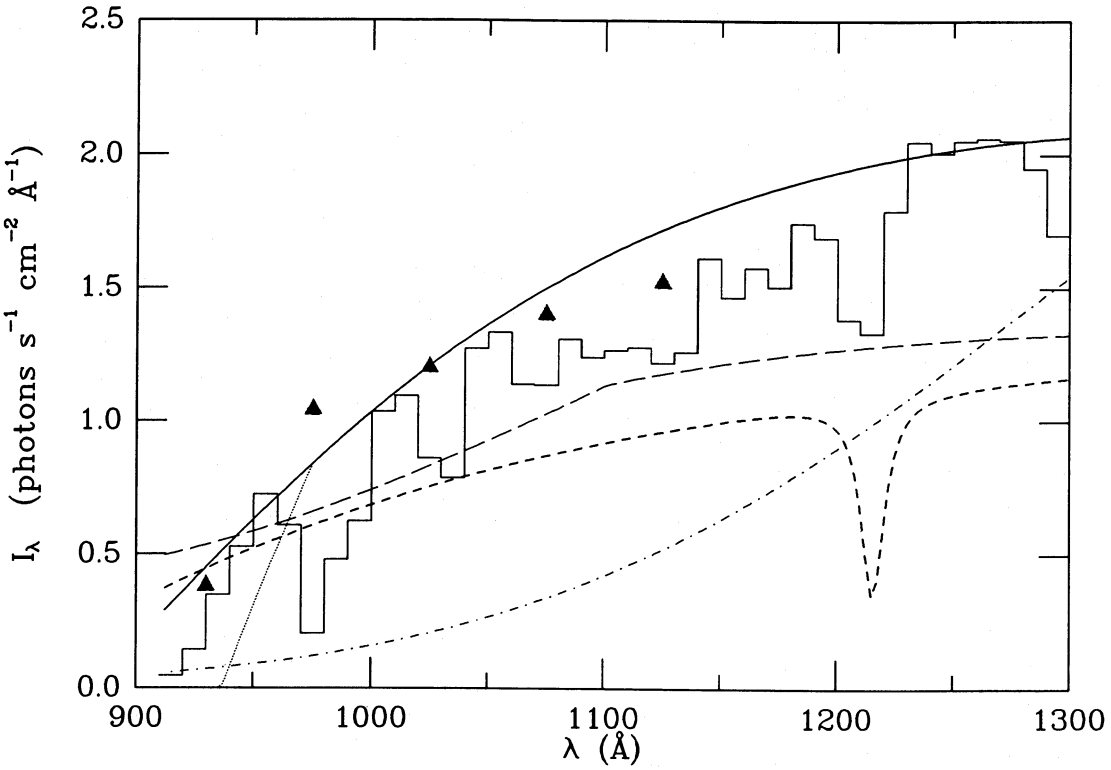

FIG. 7.—Wavelength dependence of the interstellar radiation field for several representations. Solid curve is the adopted radiation field of Draine (1978). Filled triangles are the fluxes calculated for the solar vicinity by Jura (1974). Long-dashed curve is the radiation field of Mathis *et al.* (1983). Short-dashed curve is a smoothed version of the radiation field of Gondhalekar *et al.* (1980). Dot-dashed curve is a smooth version of the radiation field by Grewing (1975). Solid histogram represents the spectrum of the B1 IV star α Vir measured by Brune *et al.* (1979). This spectrum has been corrected for a reddening of $E(B-V) = 0.02$ mag and has been scaled to match the Draine (1978) interstellar intensity at $\lambda = 1265$ Å. Dotted curve is the adopted modified version of the Draine field at $\lambda < 975$ Å.

of the few exceptions is the CN molecule, for which photodissociation also takes place primarily at $\lambda < 1000$ Å (van Dishoeck 1987). The decrease in the intensity of the radiation field at short wavelengths helps to diminish the discrepancy between model and observed abundances for this species as well.

The ratio of the computed ^{12}CO and ^{13}CO column densities is typically (45 ± 10) in the models for an adopted isotope ratio $[^{12}C]/[^{13}C] = 45$ of carbon in all forms, based on the $^{12}CH^+/^{13}CH^+$ measurements of Hawkins and Jura (1987). It is not modified significantly if the ^{13}CO shifts of Stark *et al.* (1988) are adopted. This ratio is consistent with the ratio $^{12}CO/^{13}CO = (55 \pm 11)$ inferred for the ζ Oph cloud from ultraviolet observations by Wannier, Penzias, and Jenkins (1982), but is substantially lower than the ratio of ~80 inferred by Langer *et al.* (1987) from millimeter observations. As discussed below, the $^{12}CO/^{13}CO$ abundance ratio depends on the temperature in the cloud through temperature-sensitive exchange reactions and is also affected by the overall carbon depletion factor. The data thus suggest either a somewhat higher temperature (weighted by the CO column density) in the ζ Oph cloud, a smaller value of δ_C than adopted to fit the uncertain C^+ column density, or a somewhat larger $[^{12}C]/[^{13}C]$ ratio than suggested by the $^{12}CH^+/^{13}CH^+$ abundance ratio. In particular, if LMs are included in the chemistry at the level suggested by the ionization balance (Lepp *et al.* 1988), δ_C is decreased and the $^{12}CO/^{13}CO$ abundance is increased from 47 to 74. A much higher temperature in the center of the ζ Oph cloud would be inconsistent with the observational data on C_2 (see van Dishoeck and Black 1986*b*).

Because of the lingering uncertainties in the exact shape and strength of the radiation field between 912 and 1100 Å, we have continued to use the original radiation field of Draine (1978) as our reference in the subsequent calculations. Results with the modified radiation field at $\lambda < 975$ Å (see Fig. 7) would be similar to those with the original Draine radiation field, but with the scaling factor of the radiation field reduced by a factor of ~2.

b) Translucent Clouds

i) ^{12}CO *Abundance*

Models of thicker clouds are of interest because they clearly demonstrate how the fraction of carbon in CO grows with increasing cloud thickness (Langer 1976; de Jong, Dalgarno, and Boland 1980; Boland and de Jong 1984; Glassgold *et al.* 1985). A particularly interesting class is that of the translucent clouds. A translucent cloud is defined here as a cloud in which photoprocesses still play an important role in the chemistry throughout the cloud, even though their rates diminish rapidly toward the center. The clouds typically have total visual extinctions $1 < A_V^{tot} < 5$ mag, and thus occupy the region of parameter space between the classical diffuse and dense interstellar clouds. They have the virtue that they can be studied observationally not only by millimeter emission lines, but also by absorption line techniques, provided that a suitable background star is available. A number of such translucent clouds, or small molecular clouds, have been identified in recent years by searches for molecular absorption lines toward highly reddened stars (Hobbs, Black, and van Dishoeck 1983; Lutz

and Crutcher 1983; van Dishoeck and de Zeeuw 1984; Crutcher 1985; Crutcher and Chu 1985; Cardelli and Wallerstein 1986; Gredel and Münch 1986; Federman and Lambert 1988; van Dishoeck and Black 1988*b*), and sometimes accidentally by CO millimeter observations (Knapp and Bowers 1988). A good example is provided by the small cloud in front of the star HD 169454, investigated recently by Jannuzi *et al.* (1988). Although the translucent models are usually taken to refer to isolated small clouds, they may also represent the outer edges of dense molecular clouds.

In Table 7, a series of models with increasing $N(H_2)$ and total visual extinction A_V^{tot} is presented. All other parameters such as temperature and density are kept fairly similar in the models. Models T3–T6 have gradients of temperature and density through the cloud: the temperatures at the outer boundaries of these clouds are ~50–60 K, decreasing to 15–20 K in the centers; the densities $n_H = n(H) + 2n(H_2)$ at the edge are ~300–400 cm^{-3}, increasing to 700–1000 cm^{-3} in the centers. Results are presented for two values of the depletion factor of carbon, $\delta_C = 0.4$ and 0.1.

Model T1 represents a typical diffuse cloud such as the ζ Per cloud, where the CO photodissociation transitions just start to become saturated. Carbon is still mostly in the form of C^+ in this cloud. In model T2, the H_2 column density is increased by only a factor of 2 with respect to model T1, but both the CO and C column densities are larger by an order of magnitude for the same value of δ_C, owing to the rapid decrease of the photodissociation rate of CO and photoionization rate of C inside the cloud. Another factor of 2 increase in H_2 column density results in further large increases in CO and C column densities. The C^+ column density stays approximately constant in the models. In model T4 with $A_V^{tot} \approx 2$ mag, the CO and C^+ column densities are comparable, and for thicker clouds, CO becomes the dominant form of carbon. Thus in the extinction

TABLE 7

COMPUTED COLUMN DENSITIES[a] FOR TRANSLUCENT CLOUDS[b]

Model	n_H (cm^{-3})	T (K)	A_V^{tot} (mag)	I_{UV}	δ_C	H_2	H	C	C^+	CO	^{13}CO	$C^{18}O$	$^{13}C^{18}O$
T1	500	40	0.7	1	0.4	5.0(20)	1.0(20)	6.8(15)	2.0(17)	5.0(14)	1.6(13)	4.9(11)	1.6(10)
					0.1			9.1(14)	5.0(16)	3.4(14)	6.7(12)	3.7(11)	9.1(9)
T2	500	40	1.3	1	0.4	1.0(21)	1.2(20)	2.4(16)	3.6(17)	6.6(15)	2.9(14)	4.3(12)	1.7(11)
					0.1			3.4(14)	9.0(16)	4.3(15)	1.3(14)	3.2(12)	8.2(10)
T3[c]	500	20	2.0	1	0.4	1.5(21)	2.9(20)	8.6(16)	4.8(17)	6.2(16)	2.8(15)	2.3(13)	8.7(11)
					0.1			1.1(16)	1.0(17)	3.8(16)	9.2(14)	1.8(13)	2.8(11)
T4[c]	700	15	3.0	1	0.4	2.2(21)	3.1(20)	1.3(17)	4.3(17)	3.2(17)	7.6(15)	1.1(14)	1.7(12)
					0.1			2.1(16)	9.7(16)	1.0(17)	1.9(15)	4.0(13)	4.9(11)
T5[c]	1000	15	3.9	1	0.4	3.0(21)	2.0(20)	1.5(17)	3.7(17)	6.4(17)	1.4(16)	3.2(14)	4.1(12)
					0.1			3.0(16)	8.8(16)	1.8(17)	3.2(15)	8.9(13)	1.1(12)
T6[c]	1000	15	5.1	1	0.4	4.0(21)	2.1(20)	1.3(17)	3.8(17)	1.1(18)	2.2(16)	8.2(14)	1.3(13)
					0.1			2.8(16)	9.0(16)	2.8(17)	5.3(15)	2.3(14)	3.5(12)
T6A	1000	15	5.1	1	0.4	4.0(21)	2.1(20)	1.5(17)	4.2(17)	1.0(18)	2.4(16)	9.3(14)	1.1(13)
T6B	1000	50	5.1	1	0.4	4.0(21)	1.5(20)	1.3(17)	3.9(17)	1.0(18)	2.2(16)	8.6(14)	1.5(13)
T6C	10000	15	5.0	1	0.4	4.0(21)	2.7(19)	1.3(17)	1.3(17)	1.3(18)	3.0(16)	9.8(14)	1.1(13)
T6D[d]	1000	15	5.2	1	0.4	4.0(21)	3.4(20)	4.4(17)	8.9(17)	2.0(17)	1.2(16)	4.6(13)	2.1(12)
H1	500	40	0.4	0.5	0.4	3.0(20)	5.2(19)	5.6(15)	1.2(17)	4.8(14)	1.6(13)	4.6(11)	1.6(10)
H2	500	40	0.7	0.5	0.4	5.0(20)	6.0(19)	1.2(16)	1.8(17)	1.9(15)	7.6(13)	1.5(12)	5.5(10)
H3	500	40	1.3	0.5	0.4	1.0(21)	6.9(19)	3.8(16)	3.2(17)	2.7(16)	1.1(15)	1.2(13)	4.5(11)
H4	500	40	1.9	0.5	0.4	1.5(21)	7.3(19)	6.6(16)	3.5(17)	1.6(17)	4.5(15)	5.4(13)	1.4(12)
H5	500	40	2.6	0.5	0.4	2.0(21)	7.8(19)	7.5(16)	3.4(17)	3.4(17)	8.4(15)	1.3(14)	2.6(12)
H6	500	40	3.8	0.5	0.4	3.0(21)	8.7(19)	8.7(16)	3.5(17)	7.3(17)	1.6(16)	4.7(14)	7.6(12)
I1	2000	30	0.8	10	0.4	5.0(20)	2.7(20)	3.9(15)	2.3(17)	2.9(13)	7.8(11)	3.6(10)	1.1(9)
I2	2000	30	1.4	10	0.4	1.0(21)	2.9(20)	1.4(16)	4.1(17)	2.2(14)	8.1(12)	2.1(11)	8.5(9)
I3	2000	30	2.1	10	0.4	1.5(21)	3.0(20)	5.1(16)	5.6(17)	1.6(15)	9.1(13)	1.1(12)	5.6(10)
I4	2000	30	2.7	10	0.4	2.0(21)	3.1(20)	1.2(17)	6.7(17)	1.2(16)	7.3(14)	4.9(12)	2.7(11)
I5	2000	30	4.0	10	0.4	3.0(21)	3.2(20)	2.5(17)	7.1(17)	2.1(17)	6.2(15)	5.5(13)	1.5(12)
I6	2000	30	5.2	10	0.4	4.0(21)	3.2(20)	3.2(17)	7.1(17)	5.2(17)	1.2(16)	2.0(14)	3.8(12)
I7	2000	30	9.0	10	0.4	7.0(21)	3.3(20)	3.1(17)	7.4(17)	1.7(18)	3.8(16)	2.0(15)	3.9(13)
I8	2000	30	12.8	10	0.4	1.0(22)	3.4(20)	3.2(17)	7.5(17)	2.9(18)	6.2(16)	4.4(15)	8.7(13)

[a] In cm^{-2}.

[b] All models have an oxygen depletion factor $\delta_O = 0.5$, use a cosmic-ray ionization rate $\zeta = 5 \times 10^{-17}$ s^{-1}, and employ grain model 2, unless otherwise indicated. The adopted CO excitation temperature increases from $T_{ex} = 5$ K for the lower column density models to $T_{ex} = 10$–20 K for the highest column density models.

[c] These models have temperatures and densities varying with depth. The tabulated values refer to the center of the model.

[d] This model uses grain model 3.

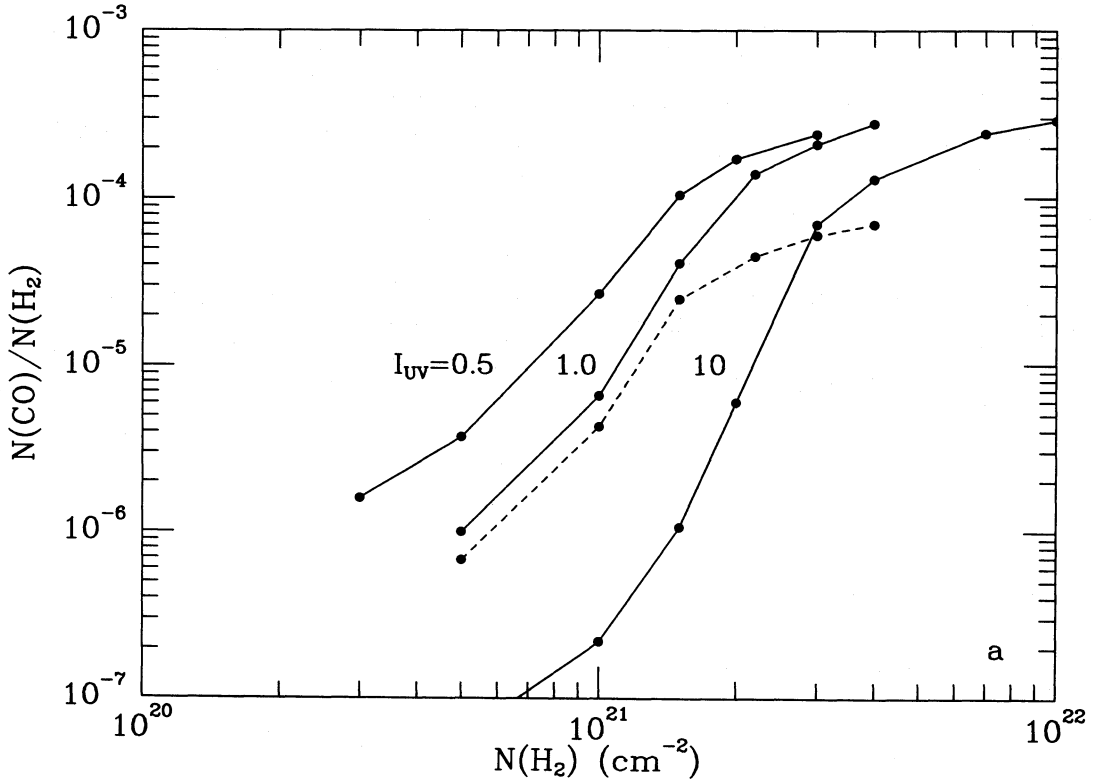

FIG. 8a

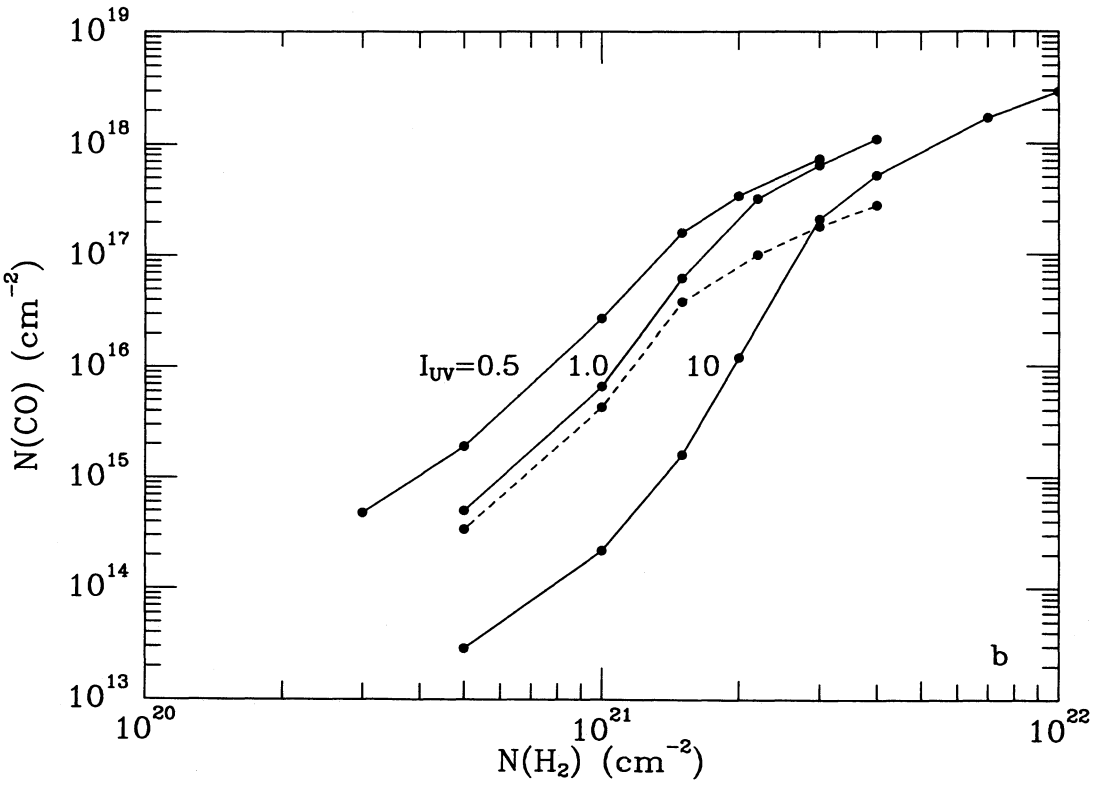

FIG. 8b

FIG. 8.—(*a*) Computed CO/H_2 column density ratio as a function of total H_2 column density for the translucent clouds of Table 7. Curve labeled $I_{UV} = 0.5$ refers to models H1–H6; curves labeled $I_{UV} = 1$ to models T1–T6; and curve $I_{UV} = 10$ to models I1–I8. All full curves are for $\delta_C = 0.4$, whereas dashed curve refers to $\delta_C = 0.1$ and $I_{UV} = 1$. (*b*) Total CO column density as a function of total H_2 column density for the same translucent cloud models.

range $A_V^{tot} \approx 1$–5 mag, the $N(CO)/N(H_2)$ column density ratio changes by almost three orders of magnitude from $\sim 10^{-7}$, the value appropriate for diffuse clouds, to 10^{-4}, the value thought to apply to dense clouds. This variation is illustrated graphically in Figure 8*a*. The fraction of gas-phase carbon in CO increases from less than 1% to nearly 100%. Figure 9 shows the concentrations of the various species as functions of depth into translucent cloud model T6. Note that the $C^+ \rightarrow C \rightarrow CO$ transition is much less sharp than the $H \rightarrow H_2$ transition zone.

As Table 7 indicates, the CO column densities are not as strongly affected by the depletion factor of carbon as the C and C^+ column densities, provided that CO is not the dominant form of carbon. The adopted depletion factor $\delta_C = 0.4$ in most models probably gives a reasonable upper limit to the amount of gas-phase carbon in the clouds, since at least 50% of the carbon is needed to form the grains. Carbon may be somewhat more depleted in denser regions. Figure 8*a* illustrates the sensitivity of the $N(CO)/N(H_2)$ ratio to the carbon depletion factor. For lower values of δ_C, the transition region where CO becomes significant is shifted to slightly larger values of A_V^{tot}, and the maximum CO column density is, of course, smaller. Plots of the total CO column densities versus total H_2 column densities (Fig. 8*b*) are useful for direct comparison with observations.

The CO transition region depends sensitively on the intensity of the incident radiation field. This is illustrated by two additional series of translucent cloud models which are included in Table 7. Models H1–H6 have the scaling factor for the radiation field reduced to $I_{UV} = 0.5$, whereas in models I1–I8, I_{UV} is increased to 10. The temperature and density in models H1–H6 are kept constant at $T = 40$ K and $n_H = 500$ cm^{-3}, whereas models I1–I7 have somewhat larger densities $n_H = 2000$ cm^{-3} with $T = 30$ K. The models with the reduced radiation field may be appropriate to describe the clouds that have recently been detected at high galactic latitudes (Magnani, Blitz, and Mundy 1985). Figures 8*a*, 8*b* include the resulting CO column densities, and the influence of the radiation field on the CO/H_2 column density ratio is apparent.

The sensitivity of the transition zone to various other parameters has been investigated through a series of models denoted as T6A–D in Table 7. Model T6A is similar to model T6, except that the temperature and density are kept constant at $T = 15$ K and $n_H = 1000$ cm^{-3} throughout the cloud. In model T6B, the temperature is increased to $T = 50$ K, with all other parameters held fixed. In model T6C, the density is increased to $n_H = 10^4$ cm^{-3}, whereas model T6D employs the more forward scattering grain model 3 instead of model 2. As Table 7 indicates, the increase in temperature or density affects the total CO column densities only slightly. This is not surprising, since CO is already the dominant form of carbon integrated through this cloud. The use of grain model 3 has the same effect as an increase in I_{UV}: the CO column density is reduced, whereas the C and C^+ column densities are significantly increased. The effects of the parameters with increasing cloud thickness are illustrated in Figure 10, where the cumulative CO column densities are plotted as functions of depth, or, equivalently, as functions of H_2 column densities. This figure is similar to Figure 8*b*, except that the CO column densities

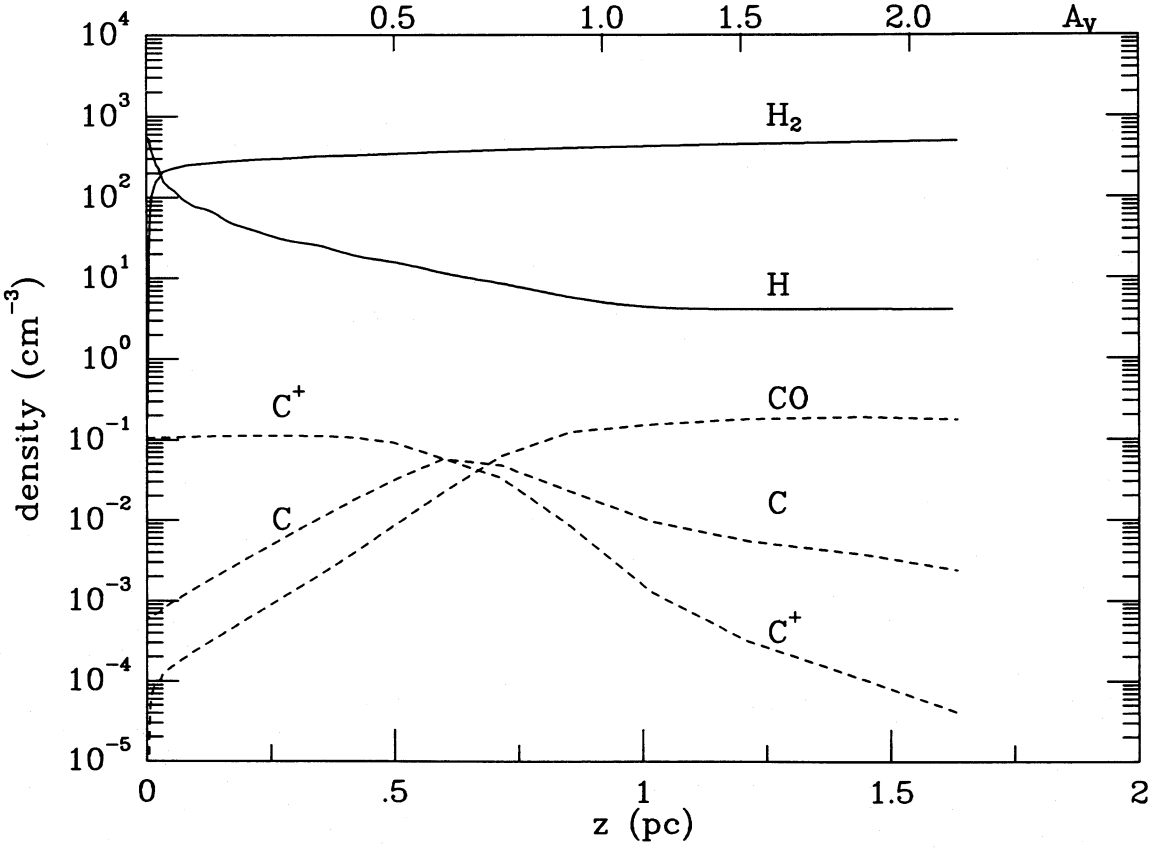

FIG. 9.—Densities of the major species as functions of depth into the translucent cloud model T6

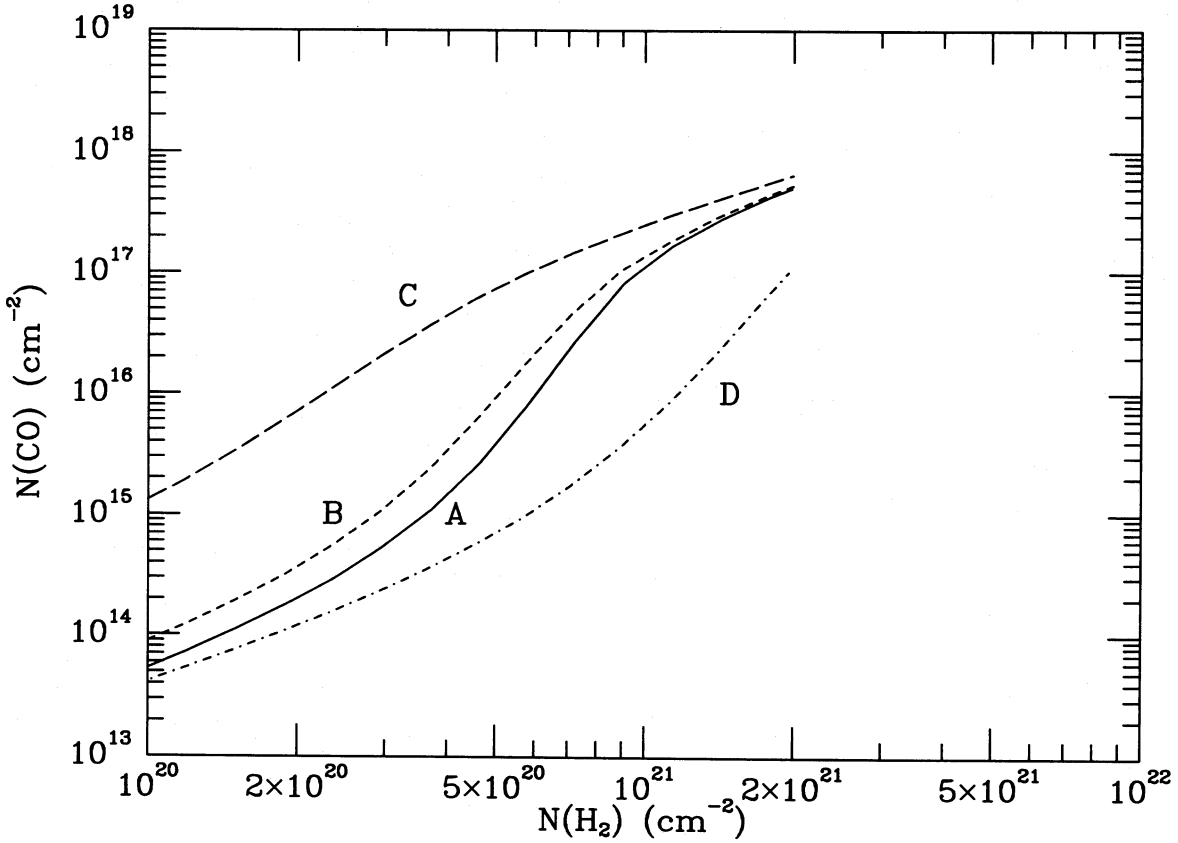

FIG. 10.—Cumulative CO column densities as functions of cumulative H_2 column densities in models T6A–D. *Full line:* model T6A with $n_H = 10^3$ cm^{-3} and $T = 15$ K. *Short-dashed line:* model T6B with $T = 50$ K. *Long-dashed line:* model T6C with $n_H = 10^4$ cm^{-3}. *Dash-dotted line:* model T6D, which uses grain model 3 instead of model 2.

result from one model with $A_V^{tot} = 5.2$ mag, rather than from a series of discrete models with A_V^{tot} increasing from 1 to 5 mag. Thus the radiation field is effectively reduced in Figure 10 compared with Figure 8*b*, with the consequence that the transition region is shifted to somewhat lower H_2 column densities. Figure 10 clearly illustrates that an increase in density shifts the transition zone to smaller H_2 column densities or visual extinction, whereas the use of the more forward scattering grain model 3 shifts the region to larger H_2 column densities.

ii) *Isotopic Abundances*

The relative abundances of the isotopic species in the clouds are determined by several competing effects, which have been discussed extensively by Bally and Langer (1982), Chu and Watson (1983), and Glassgold *et al.* (1985). As Figures 5 and 6 illustrate, the photodissociation rates of the isotopic species are significantly larger than that of ^{12}CO inside a translucent cloud. This selective destruction of the isotopes is counteracted by ion-molecule exchange reactions such as

$$^{13}C^+ + {}^{12}CO \rightleftarrows {}^{12}C^+ + {}^{13}CO + 36\ K \qquad (9)$$

which enhance the amount of ^{13}CO with respect to ^{12}CO at low temperatures. The amount of fractionation depends in detail on the cloud properties, such as its total thickness, the strength of the incident radiation field, the temperature structure, and the carbon depletion factor. At the edge of the cloud, the photodissociation rate is normally so rapid that the ion-exchange reaction cannot compete. Inside the cloud, there is usually a region where both isotope-selective processes are effective. Deep inside the cloud, the photodissociation rate has diminished so much that processes like

$$He^+ + CO \rightarrow C^+ + O + He \qquad (10)$$

start to dominate the destruction of CO and its isotopes. At this depth, the $^{13}C^+$ concentration has usually also become so small that reaction (9) does not contribute anymore to the formation of ^{13}CO. Thus the isotope fractionation effects will be most significant for translucent clouds and in the outer regions of dense molecular clouds (see Bally and Langer 1982; Glassgold *et al.* 1985).

Table 7 includes the resulting isotopic CO column densities in the various models. The computed $^{12}CO/^{13}CO$ column density ratios range between 25 and 55 for the adopted abundance ratio $[^{12}C]/[^{13}C] = 45$ of carbon in all forms. The lower part of this range is found mostly for clouds of lower column density with $\delta_C = 0.4$, whereas the ^{13}CO appears not to be fractionated significantly for the thicker clouds, or if carbon is more depleted. Both the $^{12}CO/C^{18}O$ and $^{12}CO/^{13}C^{18}O$ column density ratios in the translucent models are substantially larger (by factors of 2–10) than the overall isotopic abundance ratios of 500 and 2.25×10^4, respectively, as a result of the larger photodissociation rates for the isotopic species. These findings depend, of course, on the adopted molecular parameters for the isotopic photodissociation, in particular on our ad hoc assignments of the vibrational quantum numbers of some excited states. However, as Table 4 demonstrates, the

largest isotope selective effect appears to come from the E–X (1, 0) band at 1051 Å, which is spectroscopically well identified. Unless the predissociation efficiency for this band is substantially lower than 100%, the results are unlikely to be in error by more than a factor of 2. Test calculations show that the ^{13}CO column densities are changed by less than 30% if the shifts measured by Stark *et al.* (1988) are adopted.

Additional insight into the fractionation processes can be gained from the variation of the isotopic abundances with depth into a cloud. In Figure 11, the ratios of the cumulative column densities of the isotopic species, normalized to the overall isotopic abundances, are presented as functions of depth into the translucent cloud model T6. The normalized ratios $\mathscr{R}$ at each depth z are obtained according to

$$\mathscr{R}(z) = \frac{N(^xC^yO)(z)}{N(^{12}C^{16}O)(z)} \times \frac{[^{12}C]}{[^xC]} \times \frac{[^{16}O]}{[^yO]}, \quad (11)$$

where

$$N(^xC^yO)(z) = \int_0^z n(^xC^yO)(z')dz' \quad (12)$$

is the cumulative column density. Plots of the local density ratios of the isotopic species with depth are very similar to those of the cumulative column densities presented in Figure 11.

The $^{13}CO/^{12}CO$ column density ratio shows a complex behavior with depth into the cloud. Initially both isotope selective effects are nearly cancelling each other so that the overall ratio deviates little from unity. At a depth of ~0.5 pc into the cloud, corresponding to 0.5 mag extinction, both the photodissociation rate and the temperature have decreased enough that the ion-exchange reaction (9) enhances the $^{13}CO/^{12}CO$ ratio by a small amount. At larger depths, the decrease in the C^+ abundance makes this reaction less effective. At the same depths, the ^{12}CO lines start to become strongly self-shielding, while the ^{13}CO lines that are not shielded by ^{12}CO are still optically thin, so that the ^{12}CO column density increases more rapidly than the ^{13}CO column density, resulting in a decrease of the $^{13}CO/^{12}CO$ ratio. At the center of the cloud, the CO photodissociation rate has become so small that the reaction (10) with He^+ is the principal destruction route, and the normalized ratio approaches unity. If the spectroscopic ^{13}CO shifts are adopted, the ratio is lowered by ~20%, but shows the same behavior with depth. Both the $C^{18}O/^{12}CO$ and $^{13}C^{18}O/^{12}CO$ ratios initially fall rapidly below unity due to the enhanced photodissociation of the isotopic species and the strong increase in ^{12}CO column density. The ion-exchange reactions are ineffective in enhancing the $^{13}C^{18}O/^{12}CO$ ratio significantly. As the importance of photodissociation decreases, the ratios start to increase again, but are still at least a factor of 2 below unity in the center of the cloud.

Figure 12 illustrates the effects of temperature on the $^{13}CO/^{12}CO$ and $^{13}CO/C^{18}O$ column density ratios with depth by comparing the results of models T6A and B. The lower temperature causes the ^{13}CO fractionation to be larger at the edge of the cloud, but the effect on the total column density is small. The effect of a higher density (model T6C) would be to shift the

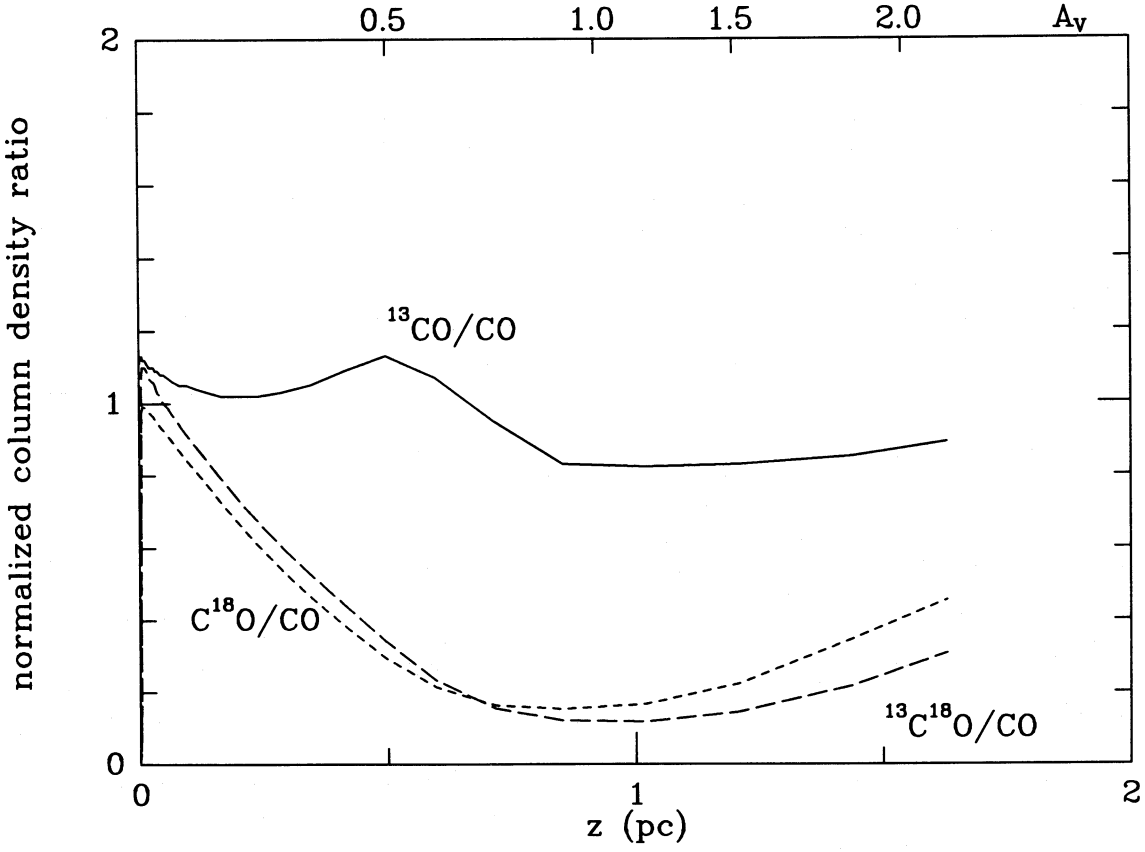

FIG. 11.—Cumulative isotopic column density ratios, normalized to the overall isotope abundances, as functions of depth into translucent cloud model T6. *Full line:* $^{13}CO/^{12}CO$. *Short-dashed line:* $C^{18}O/^{12}CO$. *Long-dashed line:* $^{13}C^{18}O/^{12}CO$.

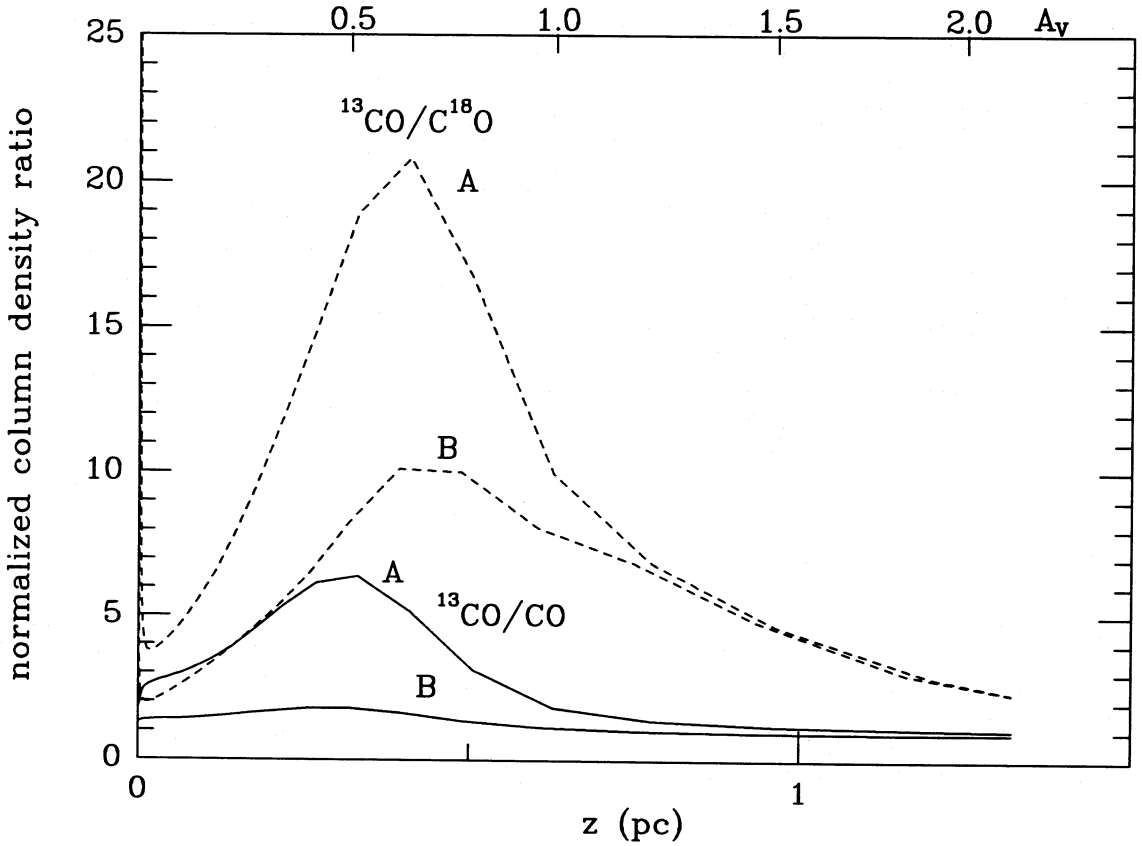

FIG. 12.—Cumulative isotopic column density ratios, normalized to the overall isotope abundances, as functions of depth into translucent cloud models T6A (T = 15 K) and T6B (T = 50 K). *Full lines:* $^{13}CO/^{12}CO$. *Dashed lines:* $^{13}CO/C^{18}O$.

peak positions to smaller depth, whereas an increase in the strength of the radiation field (model T6D or models I1–I8) would shift the peaks to larger depth. Similarly, a smaller carbon depletion factor, $\delta_C = 0.1$, would shift the peak to greater depths and would decrease the magnitude of the effect. The ratios shown in Figures 11 and 12 are consistent with the $^{12}CO/C^{18}O$ and $^{13}CO/C^{18}O$ ratios observed by Bally and Langer (1982) and Young *et al.* (1982) at the edges of molecular clouds.

The results presented in this section are qualitatively similar to those of Glassgold *et al.* (1985). They differ quantitatively due to the fact that the overall unshielded photodissociation rate of CO in this work is more than an order of magnitude larger than that employed by Glassgold *et al.*, and to differences in the molecular parameters adopted for the photodissociation of the isotopic species. In particular, Glassgold *et al.* used equal oscillator strengths for the *E–X* (1, 0) band and the (0, 0) band, whereas the (1, 0) transition is an order of magnitude weaker. As a result of these differences, the enhancement of ^{13}CO is substantially less in the current models than illustrated, for example, in Figure 7 of Glassgold *et al.* for similar temperatures.

iii) *Comparison with Observations*

Only limited observational data are available for direct comparison with the models. As summarized in Table 3 of van Dishoeck and Black (1987), the few direct measurements of CO and H_2 in interstellar clouds indicate that the CO/H_2 column density ratio does indeed increase from $\sim 10^{-7}$ in diffuse clouds to $\sim 10^{-4}$ in dense clouds, consistent with the models. No direct observations, however, have yet been possible for the interesting transition zone consisting of the translucent clouds. Some information on the CO and H_2 column densities can be obtained from indirect measurements (Dickman 1978; Frerking, Langer, and Wilson 1982; Bloemen *et al.* 1986; Bachiller and Cernicharo 1986). In particular, Frerking *et al.* (1982) performed accurate millimeter observations of ^{13}CO and $C^{18}O$ for a number of regions in the Ophiuchus and Taurus cloud complexes for which they could also estimate visual extinctions using infrared photometry of background stars. The visual extinctions can then be converted into molecular hydrogen column densities through adoption of the conversion factor $N_H/A_V^{tot} = 1.59 \times 10^{21}$ cm^{-2} mag^{-1} determined from ultraviolet absorption line observations of regions at low visual extinction (Savage *et al.* 1977), under the assumption that all the hydrogen is in molecular form. The data of Frerking *et al.* (1982) indicate a bimodal distribution of $N(C^{18}O)$ versus A_V^{tot} or $N(H_2)$, with a discontinuity for $C^{18}O$ column densities of (1–2) $\times 10^{14}$ cm^{-2} at visual extinctions of $\sim$4 mag. As Table 7 and Figure 8 indicate, this is just the region where ^{12}CO becomes strongly self-shielding and also effectively shields ^{13}CO and $C^{18}O$. The ^{13}CO column densities in the ρ Oph region show a similar abrupt rise at $A_V^{tot} \approx 4$ mag, but the relation for the Taurus sources is more gradual. Figures 13*a*–13*d* compare the ^{13}CO and $C^{18}O$ data for the Taurus and ρ Oph sources with the theoretical models of Table 7. Note that the theoretical models assume a gas to dust ratio

$N_H/A_V^{tot} = 1.59 \times 10^{21}$ cm^{-2} mag^{-1}. Within the large observational uncertainties, the ^{13}CO and C^{18}O data in the Taurus region are consistent with a normal radiation field $I_{UV} \approx 1$ and carbon depleted by $\delta_C \approx 0.1$–0.2, provided that the densities in the clouds are similar to those used in the models, $n_H \approx$ 500–2000 cm^{-3}. The ρ Oph data can be reproduced if the radiation field is enhanced, $I_{UV} \approx 5$–10, and the carbon depleted by a factor $\delta_C \approx 0.2$. Note that the temperature-dependent fractionation effects can enhance the scatter in the ^{13}CO data in the range $A_V^{tot} \approx 1$–3 mag.

The break in the C^{18}O versus A_V^{tot} relation found by Frerking *et al.* has been questioned by Duvert, Cernicharo, and Baudry (1986), Bachiller and Cernicharo (1986), and Cernicharo and Guelin (1987), who compared ^{13}CO and C^{18}O column densities with visual extinctions estimated from star counts for a large number of positions in the Perseus and Taurus clouds. The ^{13}CO and C^{18}O relations found by Cernicharo and Guelin (1987; hereafter CG) for the Heiles cloud 2 region, which contains a part of the Taurus cloud studied by Frerking *et al.*, are included in Figures 13*a* and 13*b*. It appears that the ^{13}CO relation of CG agrees well with that found by Frerking *et al.*, but that their C^{18}O column densities are much larger at low $A_V^{tot} < 4$ mag. There are several possible explanations for this discrepancy. First, the visual extinction estimates may differ by ~ 1 mag. If the star counts gave extinctions that were too low by ~ 0.5 mag, and the infrared photometry values that were too high by ~ 0.5 mag, the two sets of C^{18}O data would be reasonably consistent. Both methods have associated uncertainties of about this magnitude. Such a shift would only slightly worsen the agreement for the ^{13}CO data. Second, the C^{18}O column densities for low A_V^{tot} derived by CG under the assumption of LTE may have been overestimated. Indeed, it is likely that for regions of low A_V^{tot} with densities $n_H < 1000$ cm^{-3}, the C^{18}O is subthermally excited, as is ^{13}CO (Jannuzi *et al.* 1988). However, as argued by CG, the errors are not expected to be large: the column densities derived by Frerking *et al.* for small antenna temperatures are quite similar to those given by CG. Finally, the limited number of lines of sight surveyed by Frerking *et al.* may result in an apparent break at $A_V^{tot} \approx 4$ mag, which would be diminished for the large number of points studied by CG. The scatter in the latter data is actually substantial. It should be noted that the theoretical models also show a strong increase in C^{18}O column density for $A_V^{tot} \approx 4$–5 mag, provided that carbon is not too much depleted. A nearly linear relation is found only for quite low values of δ_C, in which case the models fall significantly below observations for large A_V^{tot}. The C^{18}O column density could be increased by raising the density or lowering the radiation field in the models. If n_H is increased to 10^4 cm^{-3} or I_{UV} is lowered to 0.5, the theoretical curves are shifted to smaller A_V^{tot} by ~ 0.3–0.5 mag. However, these curves continue to have the same nonlinear behavior for low A_V^{tot}, where they still fall below the average observed relation. The ^{13}CO/A_V^{tot} and C^{18}O/A_V^{tot} relations found by Duvert *et al.* (1986) for regions in Taurus, and by Bachiller and Cernicharo (1986; hereafter BC) for regions in Perseus, agree within factors of 2 with those found by CG for the Heiles cloud 2. The ^{13}CO and C^{18}O measurements of BC for the Perseus regions are included in Figures 13*c* and 13*d* for comparison.

In conclusion, the current models can reproduce the ^{13}CO and C^{18}O observations of Frerking *et al.*, as well as the average ^{13}CO/A_V^{tot} relations found by CG and BC, reasonably well with a consistent set of parameters. They fail to account for the large C^{18}O column densities at low A_V^{tot} suggested by the average relations of CG and BC, unless the density is higher in these regions than $n_H \approx 10^4$ cm^{-3} or the radiation field significantly lower than $I_{UV} \approx 1$. However, if either n_H were increased or I_{UV} decreased by a large factor, the models would give ^{13}CO column densities that are too high compared with observations. It is unlikely that ^{13}CO and C^{18}O sample regions with (average) densities that differ by more than an order of magnitude for $A_V^{tot} < 4$ mag. Further studies of the C^{18}O abundance in translucent clouds are warranted.

Comparison between models and observations is also possible for a number of translucent molecular clouds that have been investigated recently in more detail. In particular, Jannuzi *et al.* (1988) were able to reproduce well the variety of observational data on the cloud in front of the star HD 169454 with models similar to T3 and T4 in Table 7. Models T4 or T5 may be appropriate to describe the observed column densities of CO and other species in the translucent cloud in front of HD 29647 (Crutcher 1985; Hobbs *et al.* 1983). The translucent cloud toward the star HD 147889 in the ρ Oph region appears somewhat warmer, $T \approx 50$ K, and denser, $n_H \approx 2000$ cm^{-3} (van Dishoeck and de Zeeuw 1984), and may be exposed to more intense radiation (Snow 1983). A model in between models T4 and I4 may best represent this cloud.

Significant column densities of CO, $N(CO) \approx 10^{16}$ cm^{-2}, have recently been found in clouds at high galactic latitude (Magnani *et al.* 1985). Although the extinction determinations for these regions by the method of star counts are rather uncertain due to the paucity of background stars, the clouds appear to have quite low visual extinctions of ~ 1–2 mag. Lada and Blitz (1988) have compared the CO column densities of a sample of high-latitude clouds with those of a set of "classical" diffuse molecular clouds having similar extinctions, such as the ζ Oph and *o* Per clouds, and have concluded that the high-latitude clouds are significantly richer in CO. As Figure 8 and Table 7 demonstrate, such large CO column densities at $A_V^{tot} \approx 1$–2 mag can only be produced within the current steady state models if the intensity of the background radiation is reduced by a factor of ~ 2 with respect to the average interstellar radiation field. Such a reduction is not implausible for regions at high galactic latitude, if the young stars in the galactic disk illuminate the clouds from one side only. A small value of I_{UV} would also be necessary to explain the large CO column densities in the "tiny molecular clouds" detected in the direction of α Ori by Knapp and Bowers (1988). An independent measure of the strength of the radiation field in these regions is needed to confirm this interpretation.

Federman and Lambert (1988) have recently compared CO column densities derived from ultraviolet absorption line observations with CH column densities obtained from visual absorption line data for a number of highly reddened lines of sight with $A_V^{tot} \approx 1$–3 mag. The CH abundance is thought to vary linearly with the H_2 abundance (Danks *et al.* 1984; Mattila 1986). Although the determination of CO column densities from *IUE* observations of highly reddened lines of sight is rather uncertain, the data seem to indicate that the CO abundance increases approximately quadratically with increasing H_2 column density. The data thus show some effect due to self-shielding of CO, although the change is clearly not as pronounced as that for the H $\rightarrow$ H_2 transition. The rather gentle increase in CO column densities could be best explained if the observed regions of low column densities are exposed to rather low intensity radiation fields, $I_{UV} \approx 1$, and if carbon is more

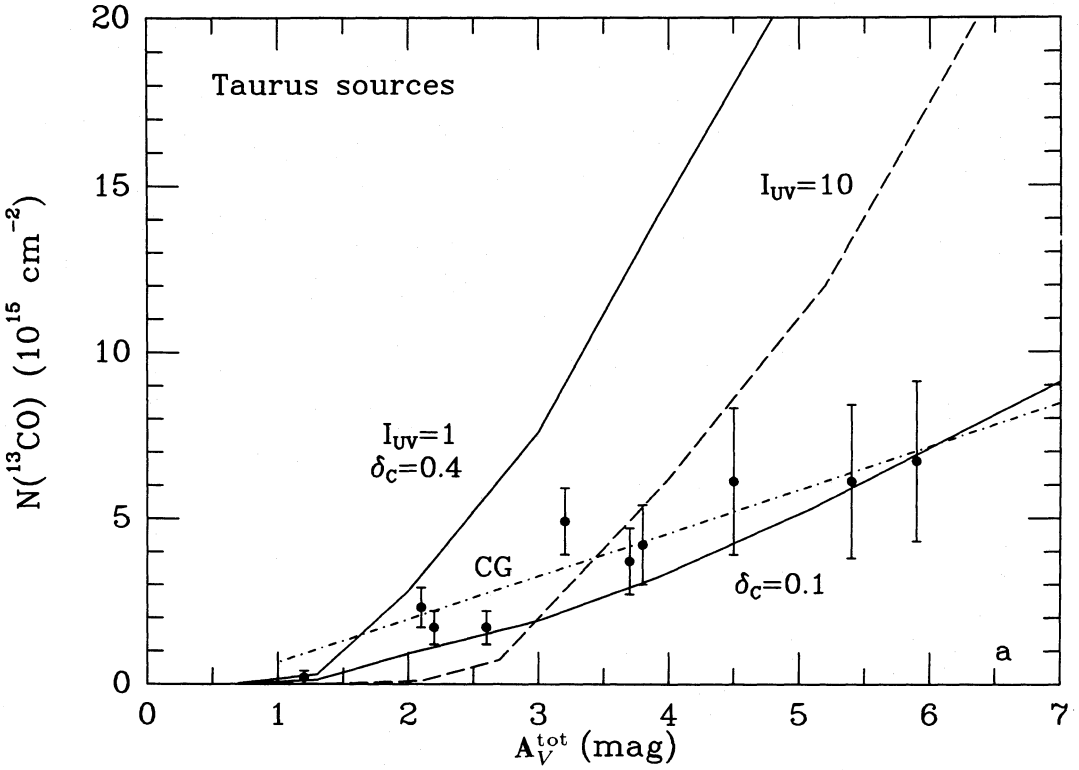

FIG. 13*a*

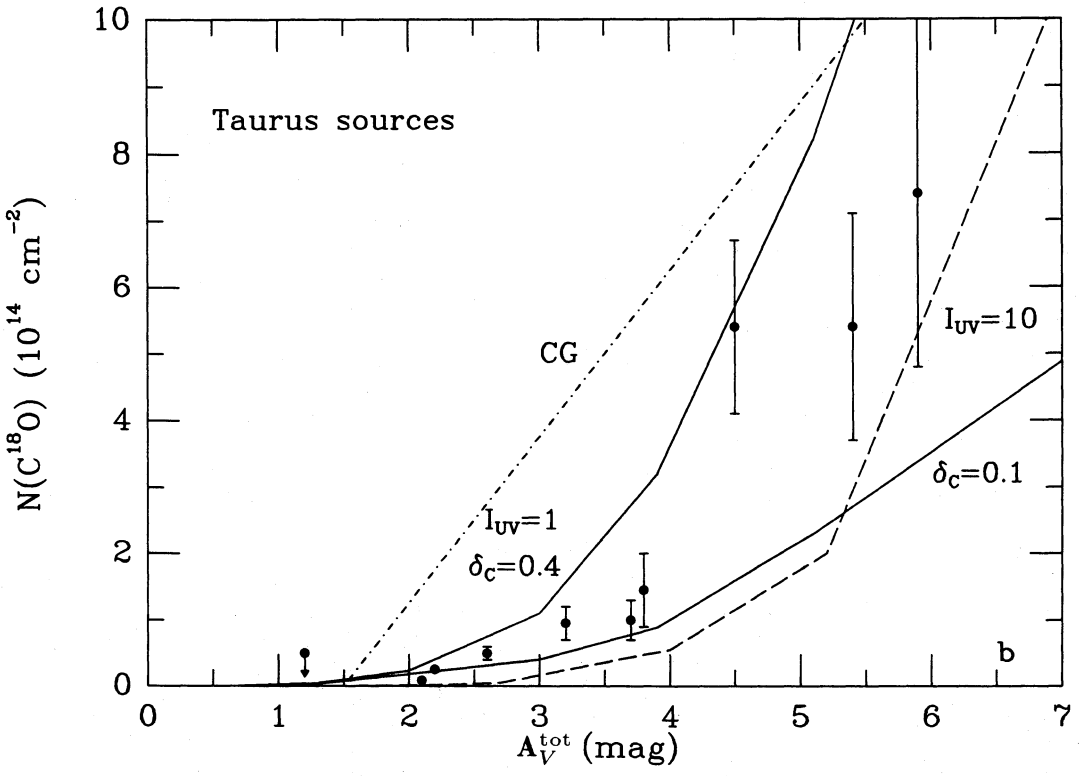

FIG. 13*b*

FIG. 13.—Comparison of the theoretical model results with measured ^{13}CO and $C^{18}O$ column densities of Frerking *et al.* (1982), indicated by big dots, as functions of total visual extinction A_V^{tot} for several positions in the Taurus (*a*), (*b*) and ρ Oph cloud complex (*c*), (*d*). Full lines are the model results for $I_{UV} = 1$ and $\delta_C = 0.4$ and 0.1, respectively. Long-dashed line is for $I_{UV} = 10$ and $\delta_C = 0.4$. Dash-dotted lines labeled CG in Figs. 14*a* and 14*b* refer to the average relations found by Cernicharo and Guelin (1987) for Heiles cloud 2. Dash-dotted lines labeled BC in Figs. 14*c* and 14*d* refer to the average relations found by Bachiller and Cernicharo (1986) for regions in Perseus.

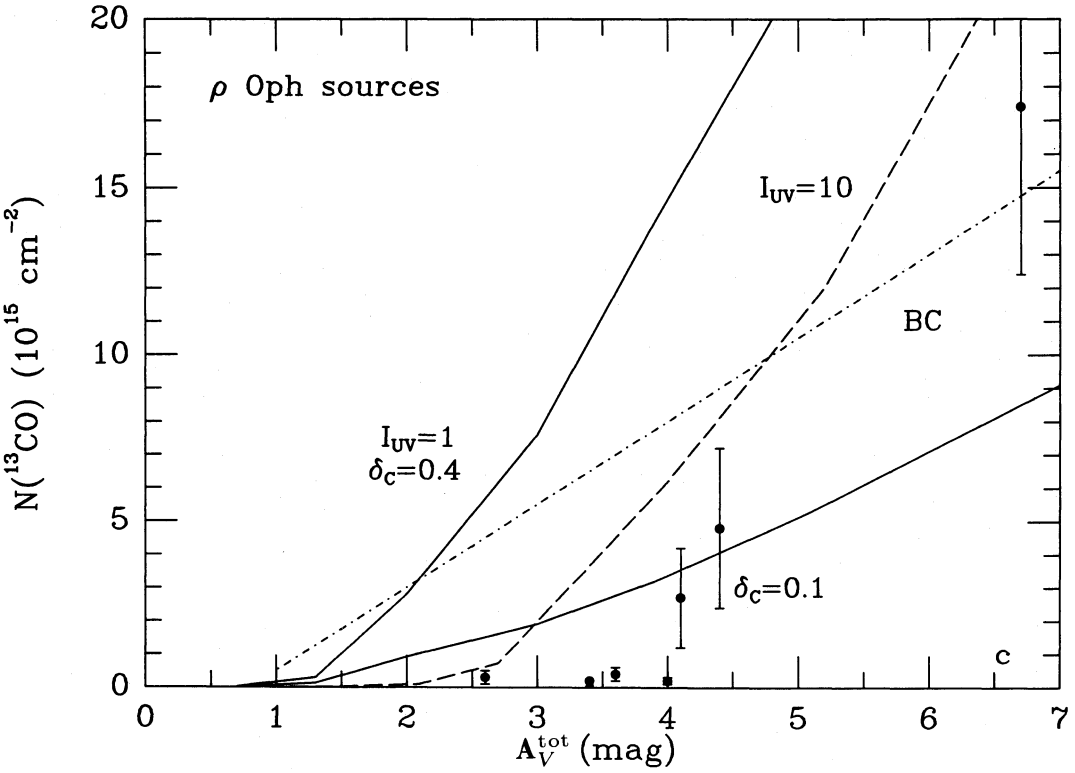

FIG. 13*c*

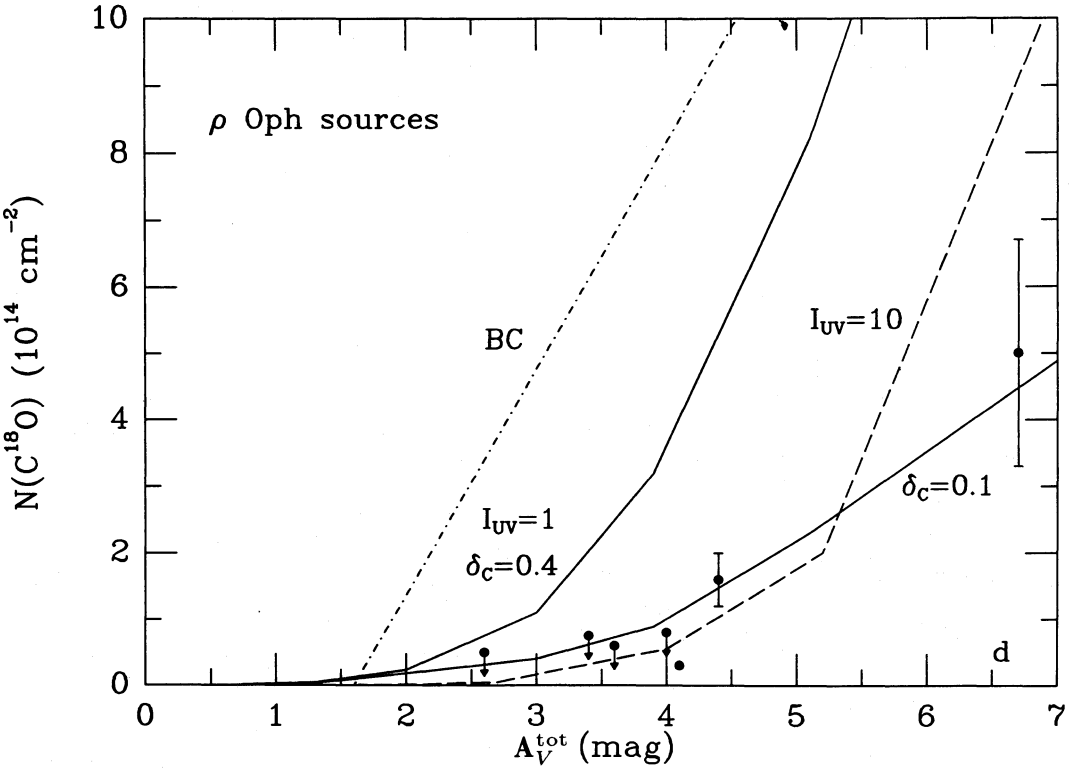

FIG. 13*d*

depleted in the clouds of higher total column density included in Figure 4 of Federman and Lambert.

Measurements of the atomic C and C^+ column densities also provide significant tests of the current models. Frerking *et al.* (1988) have recently published observations of the C 609 μm line for a number of the positions in the ρ Oph complex for which they previously obtained ^{13}CO, $C^{18}O$, and visual extinction measurements. As Table 7 indicates, the computed column density of atomic carbon increases rapidly with increasing thickness of the cloud until it reaches a constant value at $A_V^{tot} \approx 3$–5 mag. For a given cloud thickness, the amount of C can be decreased by lowering the depletion factor of carbon δ_C, and can be increased by raising the strength of the radiation field, or by using the more forward scattering grain model 3. Figures 14*a* and 14*b* illustrate the variations of the computed C column densities as functions of the ^{13}CO and $C^{18}O$ column densities in the models for various values of δ_C and I_{UV}. The observations of Frerking *et al.* (1988) are included in the figures. It appears that the models easily produce too much atomic carbon at low visual extinctions: either a significant carbon depletion, $\delta_C \approx 0.1$, or a low strength of the radiation field, $I_{UV} \approx 0.5$, or a combination of these two factors, is needed to reproduce the data. Since the ^{13}CO and $C^{18}O$ column densities as functions of A_V^{tot} require either a low carbon depletion factor or a high radiation field for $A_V^{tot} \leq 7$ mag, it appears that a low carbon depletion factor is most consistent with both sets of observations. The measurements for higher extinctions can be reproduced in models in which carbon is less depleted and the radiation field somewhat enhanced. For the clouds of highest extinction, $A_V^{tot} > 80$ mag, an additional contribution may come from the photodissociation of CO by the cosmic-ray–induced photons inside the clouds (Gredel *et al.* 1987). If this contribution is taken to be a fraction 0.005 of the abundance of ^{12}CO, an additional column $N(C) \approx 2 \times 10^{17}$ cm^{-2} can be produced inside a cloud with $A_V^{tot} \approx 80$ mag. The dash-dotted lines in Figures 14*a* and 14*b* illustrate the total carbon column density that would result if this contribution is added to that produced in the outer parts by the models with $I_{UV} = 10$ and $\delta_C = 0.4$.

It thus appears that the continued increase of the C column density with visual extinction in the ρ Oph cloud can be reproduced only if the effective incident radiation field increases for lines of sight with higher extinctions. Part of the C column density at the largest extinctions may be produced by the destruction of CO induced by cosmic rays, although this process is not actually required to reproduce the observed values. Variations of an order of magnitude in the strength of the radiation field and a factor of a few in depletion from place to place are not unlikely in an actively star-forming region like the Ophiuchus complex, and it is quite possible that the regions of highest extinction contain embedded sources of radiation. In addition, a clumpy structure of the clouds would effectively increase the amount of radiation penetrating the thicker clouds, consistent with the observed trend. Observational evidence for clumpiness on small scales in molecular clouds in general has recently been given by Falgarone and Puget (1985), Falgarone and Pérault (1987), and Blitz (1987).

It thus appears that—within these restrictions—the atomic carbon data of Frerking *et al.* (1988) can be reproduced with the present steady state models of translucent clouds and photodissociation regions, with a possible contribution from cosmic-ray–induced photodissociation of CO inside the clouds. No time-dependent effects or dynamical mechanisms (see e.g. van Dishoeck 1988*b* for a recent summary) need necessarily be invoked, although they cannot be excluded. Additional observations which could constrain the carbon depletion factor and/or the scaling factor for the radiation field independently are needed to confirm the present models.

c) *Dense Photodissociation Regions*

In the previous section, models of clouds exposed to the normal interstellar radiation field were considered. If the cloud is located close to young hot stars, the intensity of the radiation field may be enhanced by up to a factor $I_{UV} = 10^5$. In this case, the envelopes of the clouds are often denoted as "photodissociation regions" (Tielens and Hollenbach 1985). These regions are of interest observationally because they show strong atomic fine-structure emission lines of species such as C^+, C, O, and Si^+ (e.g. Melnick *et al.* 1979; Russell *et al.* 1980; Phillips and Huggins 1981; Crawford *et al.* 1985; 1986; see Watson 1985 and Melnick 1987 for reviews). In addition, the infrared line emission of H_2 due to fluorescent excitation is strong enough in these regions to be detectable (Gatley and Kaifu 1987; Gatley *et al.* 1987; Sellgren 1986). The fluorescent H_2 emission can provide valuable constraints on the physical parameters such as temperature and density (Black and van Dishoeck 1987). More importantly, it is an independent probe of the strength of the radiation field in the 912–1100 Å region, because the ultraviolet excitation of H_2 occurs in the same wavelength interval as the photodissociation of CO and the photoionization of atomic carbon. Deeper into the cloud, the rates of the photoprocesses diminish, and the atomic and ionized carbon are transformed into CO

In Table 8, a series of models of photodissociation regions are presented for increasing strength of the radiation field. In these cases, the radiation is incident on only one side of the model clouds. The density in the models is kept fixed at 10^4 cm^{-3}, whereas the temperature increases from 20 K for low I_{UV} to 100 K for clouds with $I_{UV} > 100$. Such (column averaged) temperatures are suggested by detailed calculations of the thermal balance in photodissociation regions (see Tielens and Hollenbach 1985; Sternberg and Dalgarno 1988), although the actual temperature may vary from a few hundred Kelvins at the edge to less than 100 Kelvins inside. The total column density in the models is chosen to be 10^{22} cm^{-2}, corresponding to a total visual extinction $A_V^{tot} \approx 13$ mag. At this depth, CO has become the dominant form of carbon, and the photoprocesses cease to be important. Compared with translucent clouds, the transition zone where carbon is transformed into CO has shifted from $A_V \approx 1$ mag to more than 4 mag, depending on the adopted grain model.

It appears from Table 8 that both the C and C^+ column densities increase with increasing strength of the radiation field, although the latter more strongly than the former. The C column density levels off at $N(C) \approx (2$–$3) \times 10^{17}$ cm^{-2} for $I_{UV} > 100$, $\delta_C = 0.4$, and grain model 2, whereas the C^+ column density increases up to 10^{18} cm^{-2}. These results are not significantly affected by changes of an order of magnitude in density and a factor of 2 in temperature. If the more forward scattering grain model 3 is employed (see models PF 7–8), the maximum C column density is increased up to 10^{18} cm^{-2} and that of C^+ to $(2$–$3) \times 10^{18}$ cm^{-2}. The behavior of the C^+ and C column densities with increasing strength of the radiation field is qualitatively similar to that found for the infrared line intensity of H_2 and results from the competition between the grains and the CO molecules and C atoms for the ultraviolet

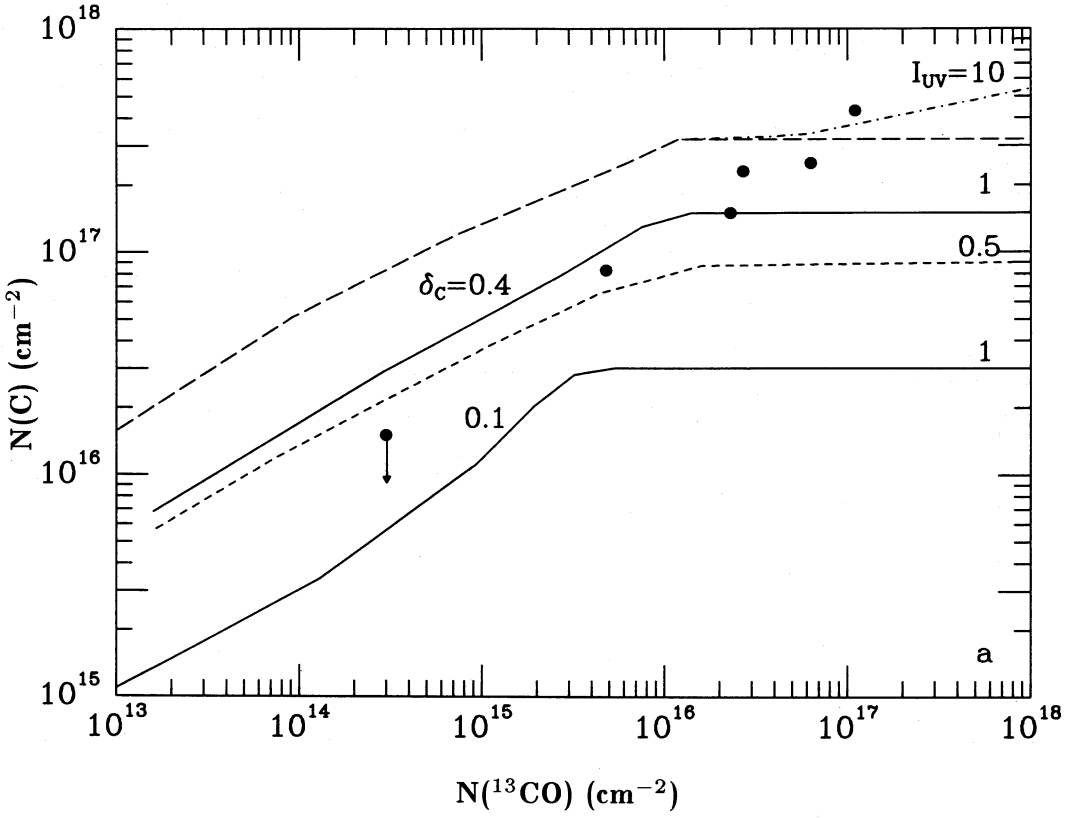

FIG. 14*a*

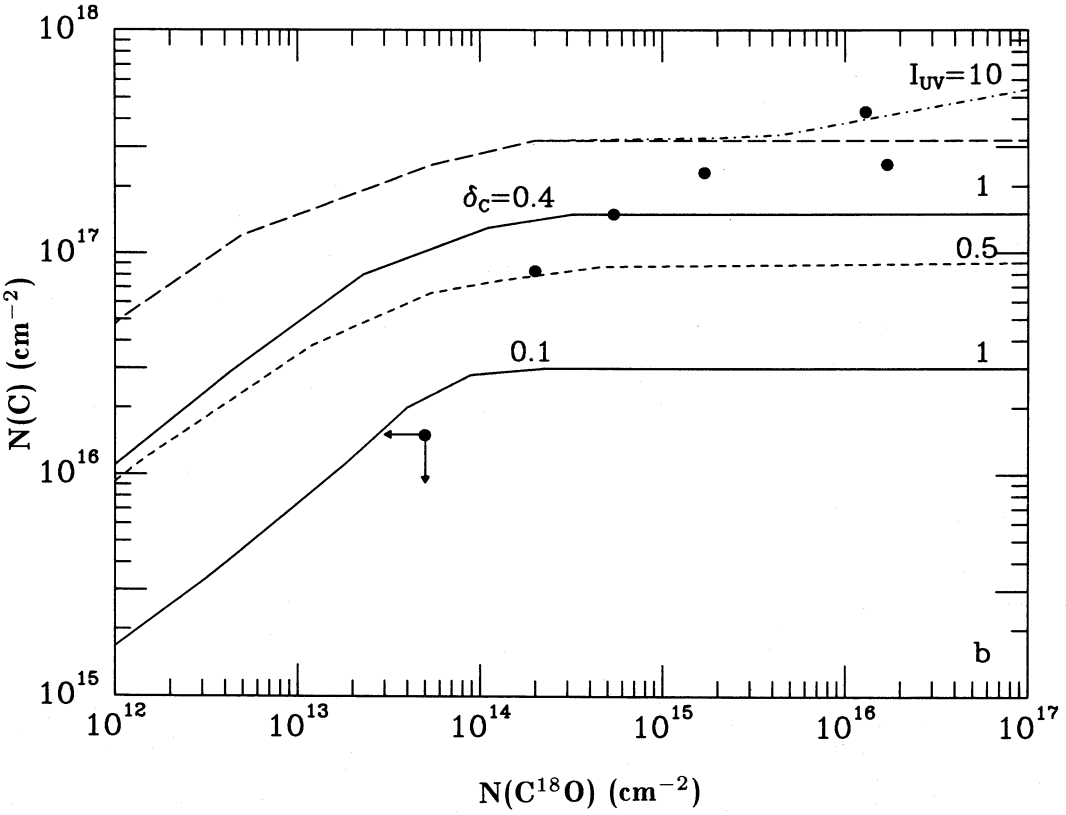

FIG. 14*b*

FIG. 14.—Total atomic carbon column density as a function of total ^{13}CO column density (*a*) and total C^{18}O column density (*b*) for different values of the strength of the radiation field I_{UV} and carbon depletion factor δ_C. Full lines are for $I_{UV} = 1$ and $\delta_C = 0.4$ and 0.1, respectively. Long-dashed line is for $I_{UV} = 10$ and $\delta_C = 0.4$; dash-dotted extension at large ^{13}CO and C^{18}O column densities is the total C column density that would result if cosmic-ray–induced photodissociation inside the cloud is taken into account in addition to the C produced at the edge; short-dashed line is for $I_{UV} = 0.5$ and $\delta_C = 0.4$. Big dots denote the values of Frerking *et al.* (1988) observed at various positions in the ρ Oph cloud complex.

TABLE 8

COMPUTED COLUMN DENSITIES[a] FOR PHOTODISSOCIATION REGIONS[b]

Model	n_H (cm^{-3})	T (K)	A_V^{tot} (mag)	I_{UV}	H_2	H	C	C^+	CO	^{13}CO
PD 1	1(4)	20	12.6	1(0)	1.0(22)	8.1(18)	9.5(16)	9.3(16)	3.3(18)	8.1(16)
PD 2	1(4)	50	12.6	1(1)	1.0(22)	3.9(19)	1.9(17)	2.6(17)	3.4(18)	7.4(16)
PD 3	1(4)	100	12.7	1(2)	1.0(22)	2.2(20)	2.0(17)	4.8(17)	3.2(18)	7.0(16)
PD 4	1(4)	100	13.2	1(3)	1.0(22)	9.8(20)	2.3(17)	7.4(17)	3.0(18)	6.7(16)
PD 5	1(4)	100	13.9	1(4)	1.0(22)	2.1(21)	3.1(17)	1.0(18)	2.9(18)	6.6(16)
PD 6	1(4)	300	13.8	1(4)	1.0(22)	1.9(21)	2.0(17)	9.9(17)	3.0(18)	6.6(16)
PD 7[c]	1(3)	100	14.1	1(2)	1.0(22)	2.4(21)	6.1(17)	2.2(18)	1.4(18)	3.2(16)
PD 8[c]	1(4)	100	26.7	1(3)	2.0(22)	2.5(21)	9.0(17)	2.3(18)	4.8(18)	1.0(17)
NGC 2023[c]	3(4)	100	13.5	3(2)	1.0(22)	1.4(21)	1.1(18)	2.5(18)	1.3(18)	3.1(16)
NGC 2024[c,d]	3(4)	40	16.7	2(1)	1.3(22)	1.6(21)	1.1(18)	1.2(18)	2.6(18)	5.8(16)

[a] In cm^{-2}.

[b] All models use an oxygen depletion factor $\delta_O = 0.5$, a carbon depletion factor $\delta_C = 0.4$, a cosmic-ray ionization rate $\zeta = 5 \times 10^{-17}\ s^{-1}$, and employ grain model 2, unless otherwise indicated. The adopted CO excitation temperature $T_{ex} = 20$–30 K in the various models. The $C^{18}O$ column density is $\sim 5 \times 10^{15}\ cm^{-2}$ and the $^{13}C^{18}O$ column density is $\sim 10^{14}\ cm^{-2}$ in models PD 1–PD 7.

[c] These models use grain model 3.

[d] Temperature and density vary with depth.

photons (see Black and van Dishoeck 1987). The dependence is less strong than in the case of H_2, because the CO formation occurs deeper into the cloud where the grains and H_2 molecules already constitute a significant part of the absorption.

The ^{13}CO column densities are included in Table 8. Because of the large total thickness of the cloud, all isotopic column density ratios are close to the adopted overall $[^{12}C]/[^{13}C]$ and $[^{16}O]/[^{18}O]$ abundance ratios.

The most critical tests of the models of photodissociation regions come from observations of the atomic species C and C^+, and their spatial distribution with respect to the radiation source. The fine-structure line intensity for transition j at frequency ν is calculated according to

$$I_\nu^j = B_\nu(T_{ex}^j)(1 - e^{-\tau_j}) , \tag{13}$$

where the Planck function B_ν is evaluated for an excitation temperature

$$T_{ex}^j = \frac{h\nu}{k \ln (g_u N_l^j / g_l N_u^j)} \tag{14}$$

that is defined in terms of the column densities of the upper and lower states of the transition, N_u^j and N_l^j, and their statistical weights g_u and g_l, respectively. The optical depth includes the nonnegligible correction for stimulated emission:

$$\tau_j = 2.245 \times 10^{-7} \frac{A_{ul}}{\tilde{\nu}^3} \frac{N_l}{b} \frac{g_u}{g_l} (1 - e^{-h\nu/kT_{ex}^j}) , \tag{15}$$

where A_{ul} is the spontaneous transition probability in s^{-1}, b is the Doppler broadening parameter in km s^{-1}, and $\tilde{\nu} = \nu/c$ is the transition frequency in cm^{-1}. The state-specific column densities result from level populations that are computed explicitly at each depth for a statistical equilibrium among the following processes: (1) spontaneous transitions $u \rightarrow l$; (2) absorption and stimulated emission $u \leftrightarrow l$ in a radiation field that includes trapped line radiation, the $T = 2.7$ K cosmic background radiation, and thermal emission by dust at a temperature $T_d = 15$ K; (3) excitation and de-excitation by collisions with electrons, H, and H_2; and (4) pumping by ultraviolet resonance lines.

The predicted intensities for the submillimeter lines of C, C^+, and O for selected models are listed in Table 9. The C^+ and O line intensities are very sensitive to the temperature structure of the cloud for $T < 100$ K, as shown by Tielens and Hollenbach (1985). This is also illustrated in Table 9 by comparison of the results of, for example, model T6A with those for other models. In particular, if any of the colder models had a warmer envelope, the C^+ and O line intensities would be increased by 1–2 orders of magnitude. Observations of the atomic carbon 609 μm line (Phillips and Huggins 1981) and 370 μm line (Jaffe *et al.* 1985; Zmuidzinas, Betz, and Goldhaber 1986) in warm dense clouds have resulted in column densities N(C) of $\sim 10^{18}\ cm^{-2}$. As Table 8 indicates, such large column densities can be reproduced within one homogeneous model only for the highest densities and fluxes, if in addition the most favorable assumptions about the scattering properties of the grains are made, and if carbon is not significantly depleted. Even more difficult to explain in terms of photodissociation models are the observed spatial distributions of C in warm regions where the ionization front is seen edge-on. In particular, the measurements of the C 609 μm line and the ^{12}CO and ^{13}CO $J = 1 \rightarrow 0$ millimeter lines in M17 and S140 by Keene *et al.* (1985) at positions offset from the ionization front show that, contrary to expectations, the C emission peaks farther into the molecular cloud than does CO. The estimated visual extinction between the ionization peak and the C peak is at least 60 mag. Stutzki *et al.* (1988) have recently observed the C^+ 158 μm fine-structure line in M17 at various places offset from the ionization front. Appreciable amounts of C^+ are found not only near the edge of the cloud, but also deep inside, in contrast with the models.

Although the cosmic-ray–induced photodissociation of CO can produce substantial amounts of atomic carbon inside dense clouds (Gredel *et al.* 1987), the process may not be sufficient to explain the observed column densities for M17 and the spatial distribution. In addition, the cosmic-ray photons are not effective in forming significant amounts of C^+ inside the clouds. Stutzki *et al.* (1988) have recently argued that much of the C and C^+ data for M17 can be explained by a clumpy structure of the cloud. In that case, the ultraviolet photons penetrate effectively between clumps and are thus available to photodissociate CO and ionize carbon deeper into the cloud. In order to obtain quantitative agreement with the data, the filling factor of the clumps must be sufficiently low (0.1–0.4 by

TABLE 9

COMPUTED ATOMIC FINE-STRUCTURE LINE INTENSITIES[a] FOR SELECTED MODELS[b]

Model	$C(^3P_1 \rightarrow {}^3P_0)$ (609 μm)	$C(^3P_2 \rightarrow {}^3P_1)$ (370 μm)	$C^+(^2P_{3/2} \rightarrow {}^2P_{1/2})$ (158 μm)	$O(^3P_1 \rightarrow {}^3P_2)$ (63 μm)	$O(^3P_0 \rightarrow {}^3P_1)$ (145 μm)
ζ Oph	8.9(−8)	5.5(−7)	8.2(−5)	2.0(−6)	6.9(−3)
T1	1.3(−7)	8.2(−7)	1.8(−5)	4.3(−8)	1.3(−3)
T2	3.9(−7)	2.7(−6)	1.8(−5)	4.4(−8)	1.1(−3)
T3	6.3(−7)	6.4(−6)	2.6(−5)	2.1(−7)	1.3(−3)
T4	9.3(−7)	8.8(−6)	4.6(−5)	5.2(−7)	1.4(−3)
T5	1.6(−6)	1.2(−5)	9.5(−5)	1.6(−6)	1.5(−3)
T6	2.0(−6)	1.3(−5)	1.4(−4)	7.4(−6)	2.8(−3)
T6A	4.0(−7)	3.5(−6)	8.0(−7)	3.4(−10)	5.5(−4)
T6B	1.6(−6)	1.1(−5)	5.2(−5)	3.2(−7)	9.8(−4)
T6C	1.2(−6)	5.3(−6)	2.8(−6)	1.5(−9)	7.8(−5)
H1	1.1(−7)	6.8(−7)	1.7(−5)	3.9(−8)	1.4(−3)
H3	5.3(−7)	4.0(−6)	1.7(−5)	4.1(−8)	1.1(−3)
H5	7.4(−7)	6.6(−6)	1.7(−5)	4.5(−8)	9.2(−4)
H6	7.8(−7)	7.3(−6)	1.7(−5)	4.9(−8)	8.2(−4)
I1	8.1(−8)	4.9(−7)	6.0(−5)	8.8(−8)	2.6(−3)
I3	9.3(−7)	5.8(−6)	5.6(−5)	7.7(−8)	1.8(−3)
I6	3.2(−6)	2.2(−5)	5.5(−5)	8.3(−8)	1.3(−3)
I8	3.2(−6)	2.2(−5)	5.5(−5)	9.8(−8)	9.4(−4)
PD 3	3.9(−6)	2.3(−5)	7.7(−4)	1.2(−4)	3.2(−3)
PD 4	4.5(−6)	2.6(−5)	1.0(−3)	1.7(−4)	2.3(−3)
PD 5	6.0(−6)	3.5(−5)	1.3(−3)	2.4(−4)	1.9(−3)
PD 6	4.1(−6)	2.5(−5)	1.8(−3)	2.3(−3)	5.9(−3)
NCG 2023	1.0(−5)	4.2(−5)	4.1(−4)	4.0(−5)	2.0(−4)
NGC 2024	5.9(−6)	2.4(−5)	1.4(−4)	3.8(−6)	1.9(−4)

[a] In ergs s^{-1} cm^{-2} sr^{-1}.

[b] All results are for a carbon depletion factor $\delta_C = 0.4$, except for the ζ Oph model G which uses $\delta_C = 0.67$.

volume), and the interclump medium must be nearly transparent to the radiation. Additional embedded low-luminosity sources need to be invoked, however, to reproduce the measured C and C^+ abundances at cloud depths as large as 60 mag. Observations of the fluorescent infrared line emission of H_2 in these regions would provide a direct measure of the strength of the radiation field offset from the ionization front, and would be a significant test of the models. Nevertheless, it is clear that more detailed calculations of models of clumpy clouds, which include both the photo processes at the edges, as well as the cosmic-ray–induced photodissociation inside, are needed to investigate the influence on the C and C^+ line intensities. The models presented here for homogeneous clouds can serve as the input for the properties of the individual clumps in these models.

Table 8 includes two models which were developed to reproduce existing data on two specific warm dense clouds: NGC 2023 and NGC 2024. The model parameters for NGC 2023 were constrained by Black and van Dishoeck (1987) such that they reproduce very well the H_2 infrared line emission at the 80″ south position observed by Gatley *et al.* (1987). The model for the NGC 2024 cloud is appropriate for the direction of IRS 2, and was based on the analysis of the infrared absorption lines of CO (Black and Willner 1984). More details of this last model were given already in § III, where the photodissociation rates of the various species as functions of depth were presented. The computed line intensities of C, C^+, and O in the two regions are presented in Table 9. For NGC 2023, the measured C^+ line intensity of 6×10^{-4} ergs s^{-1} cm^{-2} sr^{-1} (Crawford *et al.* 1985) is consistent with the model result, and suggests that carbon is not highly depleted in this cloud. Observations of the C 609 μm or 370 μm lines would provide significant tests of the models. The measured $N(C) \approx 10^{18}$ cm^{-2} for the NGC 2024 region (Phillips and Huggins 1981) is consistent with the column density found in the model.

V. CONCLUDING REMARKS

The most important result emerging from the new laboratory work by Letzelter *et al.* (1987) and Yoshino *et al.* (1988) is that the photodissociation of interstellar CO is finally fairly well understood. Although the adopted cross sections for individual transitions may still be inaccurate by factors of 2, the uncertainty in the total photodissociation rate is expected to be less, and is comparable to—or smaller than—the uncertainties in the intensity and shape of the interstellar radiation field and the continuum attenuation due to dust. Within these uncertainties, it is now possible to start to use the measured CO abundances as diagnostics of the physical parameters in the regions, such as the strength of the radiation field or the carbon abundance, if additional information on the total thickness of the cloud is available. The photodissociation processes of the isotopic varieties are still not as well understood. Accurate measurements of the ^{13}CO, $C^{18}O$, and $^{13}C^{18}O$ shifts at $\lambda <$ 1000 Å are needed to confirm our results. In addition, an independent measurement of the predissociation probabilities of the E–X (0, 0) and (1, 0) bands for low rotational quantum numbers is of paramount importance for understanding the isotope-selective photodissociation.

The total unattenuated photodissociation rate of CO is large, $\sim 2 \times 10^{-10}$ s^{-1}, so that a substantial reduction of the rate must occur inside the clouds in order to build up the large observed column densities of CO. The present calculations have illustrated the importance of self-shielding, mutual shielding, shielding by lines of H and H_2, and continuum attenuation in the calculation of the depth dependence of the photodissociation rates. Although some approximations in the treat-

ment of the shielding can be made without affecting the results by more than a factor of 2, care must be taken not to simplify the treatment too much if, for example, accurate information on the relative abundances of the isotopic species is needed. A table of typical shielding functions is presented to provide a fast method of computing the depth-dependent rates.

With the new CO photodissociation rate, the models of diffuse clouds have great difficulty in accounting for the observed column densities of CO. In particular, if the strength of the background radiation field is constrained by the observed rotational population of H_2, the models produce too little CO by an order of magnitude. Part of the discrepancy may result from our poor understanding of the shape of the interstellar radiation field at $\lambda < 1000$ Å, and some ad hoc modifications are suggested which would result in better agreement between measured and model CO column densities. Additional observations pertaining specifically to this problem would be useful.

The majority of new models presented in this paper concern translucent clouds with properties in between those of diffuse and dense interstellar clouds. The calculations show clearly how the fraction of carbon in CO rapidly increases with total cloud thickness. Although there are no direct measurements of CO and H_2 column densities for such clouds, the results are consistent with a variety of indirect observations. The computations also illustrate the sensitivity of the isotope abundance ratios to the local conditions in the cloud, such as temperature, strength of the radiation field, depletion of carbon, and total cloud thickness. Given this sensitivity, it is unlikely that overall carbon isotope ratios $[^{12}C]/[^{13}C]$ accurate to better than a factor of 2 can ever be derived from observations of the $^{12}CO/^{13}CO$ abundance ratio in translucent clouds without a detailed knowledge of these parameters. It is satisfying to note that the current models are capable of reproducing the observational data on atomic carbon for these regions fairly well and that no special circumstances or processes appear necessary to account for the observed amounts.

Models of dense photodissociation regions show that substantial amounts of atomic carbon can be produced near the edges. Whether the models are able to explain all of the observational data on atomic carbon for warm dense clouds is still an open question. One of the largest challenges for future models will be the inclusion of clumpiness into the calculations. In particular, the radiative transfer through various clumps and the attenuation of the radiation by the interclump medium are still not well understood, and the results are expected to depend sensitively on the sizes of the individual clumps. The current results for the translucent and dense clouds can serve as input parameters for the individual clumps in the models.

The authors are much indebted to K. Yoshino, G. Stark, P. L. Smith, W. Parkinson, and F. Rostas for many stimulating discussions concerning the ultraviolet spectrum of CO and for providing them with their laboratory results on the photodissociation cross sections and line positions prior to publication. They are also grateful to K. Kirby for communicating her theoretical results on the CO oscillator strengths, and to J. B. Keene and T. G. Phillips for sending them a preprint of their atomic carbon observations in the ρ Oph region. Finally, they thank the referee for constructive comments on the manuscript. This work was supported in part by NSF grant RII 86-20342 to Princeton University, and in part by NASA through Theoretical Astrophysics grant NAGW-763 to the University of Arizona. The hospitality of the Institute for Advanced Study, and its partial support through NSF grant PHY 86-20266, are greatly appreciated.

APPENDIX

The critical part of the radiation field for photodissociation of CO is the region $\lambda = 912$–1076 Å, which is also the least well determined (see Paresce and Jakobsen 1980). Three approaches have been used to construct an interstellar radiation field in this region. One is to adopt direct measurements of the background radiation (Sandel, Shemansky, and Broadfoot 1979; Gondhalekar *et al.* 1980; Henry, Anderson, and Fastie 1980; Paresce, McKee, and Bowyer 1980; Bixler, Bowyer, and Grewing 1984; Holberg 1986). A second technique is to calculate the radiation expected from all hot stars within some volume of space such as the nearest few hundred parsecs around the Sun (Habing 1968; Jura 1974; Henry 1977; Witt and Johnson 1973). The third method is to infer the intensity and spectral shape of the radiation from an analysis of the ionization balance of the local interstellar medium (Grewing 1975; Reynolds 1986; Chassefière *et al.* 1986). Other widely quoted discussions of the background ultraviolet radiation field include those of Mathis *et al.* (1983) who adopt the results of Gondhalekar *et al.* (1980) but scale their fluxes by a factor 1.15 to be in harmony with the measurements of Henry *et al.* (1980), and of Draine (1978), who represented a variety of theoretical and experimental results with a simple formula. The first and second methods are not always completely independent in that models of the spatial distribution of light from hot stars and of the spectral character of their light are often used to distinguish direct starlight from diffuse radiation and to interpret broad-band measurements.

Very few flux measurements have been made at wavelengths $\lambda < 1200$ Å. The ultraviolet spectrometers on the *Voyager* spacecraft have been used to measure both the fluxes of individual hot stars and of the background radiation. At $\lambda < 1100$ Å, positive detections were made at low galactic latitudes $|b| < 20°$ while only upper limits were obtained at higher latitudes (Sandel *et al.* 1979; Holberg 1986). Comparison of these measurements and limits at $\lambda = 975$ Å with the fluxes at the corresponding positions and longer wavelength, $\lambda = 1565$ Å (Gondhalekar *et al.* 1980), indicates that there are quite different latitude dependences at the two wavelengths. Specifically, the intensity ratio (photons per unit wavelength) I_{975}/I_{1565} has values 0.05–0.075 for $|b| < 10°$, 0.9–1.6 for $|b| = 11°$–$20°$, and has upper limits in the range 0.03–1.2 at $|b| > 20°$, although the number of observed points is small. This suggests caution in using the brightness distribution at longer wavelengths to convert limited data at $\lambda < 1200$ Å into mean intensities over the whole sky. Opal and Weller (1984) presented measurements of ultraviolet light in a broad band, $\lambda = 911$–1050 Å, over approximately two-thirds of the sky. They found a total intensity in this band of $I_\lambda = 1.4 \times 10^5$ s^{-1} cm^{-2} Å^{-1} over the whole sky, based on a spectrum similar to that of a B1 star. This result is not unambiguous, however, because such a spectrum is rather steep in this wavelength region and because Opal and Weller used questionable model atmospheres and reddening estimates to

interpret the measurements. Although the line-blanketed, LTE atmospheres of Kurucz (1979) or Kurucz, Peytremann, and Avrett (1974) are valuable for many purposes, they consistently overestimate the fluxes of O and B stars at $\lambda \leq 1100$ Å in comparison with calibrated, spectrophotometric observations (Brune, Mount, and Feldman 1979; Woods, Feldman, and Bruner 1985) and suggest effective temperatures that are too high for O stars. Problems of comparison between stellar observations and model atmospheres are exacerbated by uncertain extinction corrections at $\lambda \leq 1100$ Å. It appears that non–LTE effects are probably significant in atmospheres of high effective temperature and low gravity (Massa and Savage 1985), so that unblanketed non–LTE models (see Mihalas 1972) may be preferable to blanketed LTE models (see Kurucz 1979) for characterizing the spectra of O and early B stars at $\lambda \leq 1100$ Å. Unfortunately, the LTE models have been used in most discussions of the short-wavelength part of the interstellar radiation field (e.g. Jura 1974; Gondhalekar *et al.* 1980; Henry 1977).

Figure 7 compares the mean intensities, I_λ in photons s^{-1} cm^{-2} $Å^{-1}$, for several different representations of the interstellar radiation field in the solar neighborhood. It is evident that there is good general agreement among various results, at least at the longer wavelengths. The smoothed version of the spectrum inferred by Grewing (1975) lies significantly below the others at $\lambda < 1300$ Å. The ionization data analyzed by Grewing do not constrain very closely the flux specifically in the 900–1100 Å interval; moreover, such a large deficit of flux in this interval would affect not only the photochemistry of CO, but also the excitation and abundance of H_2 and the ionization of atomic carbon in our cloud models.

Figure 7 also includes the reddening-corrected spectrum of a B1 IV star, α Vir (Brune *et al.* 1979), for comparison with the interstellar radiation fields. This spectrum has been multiplied by a factor of 32.4 so that it matches the intensity of the Draine (1978) spectrum at $\lambda = 1265$ Å. The shape of this stellar spectrum is bracketed by the interstellar spectra of Draine (1978) and of Mathis *et al.* (1983) for $\lambda > 950$ Å; however, it is rather steeper than any of the interstellar spectra in the interval $\lambda = 912$–950 Å, suggesting that a steeper decline from $\lambda = 950$ Å to the Lyman limit of H is probably more realistic. The dotted curve in Figure 7 is a modified version of the Draine (1978) radiation field, constructed to have a slope even somewhat steeper than that of a B star at $\lambda < 975$ Å. As discussed in § IV*a*, such a small change in the interstellar radiation field has significant effects on the rate of photodissociation of CO in interstellar clouds owing to the large fraction of its total absorption rate that occurs at these wavelengths. An interstellar radiation field produced by B stars with strong photospheric absorption in the Lyman lines of H will also be deficient in flux at the wavelengths of these lines even without attenuation by interstellar H. The ultraviolet radiation from any O or B star within an ionization-bounded H II region will suffer substantial absorption in the Lyman lines of H I in the immediate vicinity of the star because the boundary of the H II region must correspond to an optical depth greater than unity in the Lyman continuum [i.e. a column density $N(\mathrm{H}) > 1.6 \times 10^{17}$ cm^{-2}]. Thus the interstellar radiation field may have large depressions at $\lambda = 1025.7$ and 972.5 Å. We have made no attempt to modify the radiation field for Lyman line absorption in or near its sources, but have included the interstellar absorption explicitly. Finally, there is also the possibility that interstellar dust particles or putative large molecules (e.g. PAHs) have previously undetected strong absorption features at $\lambda < 1000$ Å that would further modify the ultraviolet radiation field inside interstellar clouds.

REFERENCES

Amiot, C., Roncin, J.-Y., and Verges, J. 1986, *J. Phys. B*, **19**, L19.
Bachiller, R., and Cernicharo, J. 1986, *Astr. Ap.*, **166**, 283.
Bally, J., and Langer, W. D. 1982, *Ap. J.*, **255**, 143; **261**, 747.
Bixler, J., Bowyer, S., and Grewing, M. 1984, *Astr. Ap.*, **141**, 422.
Black, J. H., and van Dishoeck, E. F. 1987, *Ap. J.*, **322**, 412.
———. 1988, in preparation.
Black, J. H., and Willner, S. P. 1984, *Ap. J.*, **279**, 673.
Bless, R. C., and Savage, B. D. 1972, *Ap. J.*, **171**, 293.
Blitz, L. 1987, in *Physical Processes in Interstellar Clouds*, ed. G. Morfill and M. S. Scholer (Dordrecht: Reidel), p. 35.
Bloemen, J. B. G. M., *et al.* 1986, *Astr. Ap.*, **154**, 25.
Boland, W., and de Jong, T. 1984, *Ap. J.*, **134**, 87.
Brune, W. H., Mount, G. H., and Feldman, P. D. 1979, *Ap. J.*, **227**, 884.
Cardelli, J. A., and Wallerstein, G. 1986, *Ap. J.*, **302**, 492.
Cernicharo, J., and Guélin, M. 1987, *Astr. Ap.*, **176**, 299.
Chassefière, E., Bertaux, J. L., Lallemont, R., and Kurt, V. G. 1986, *Astr. Ap.*, **160**, 229.
Chu, Y.-H., and Watson, W. D. 1983, *Ap. J.*, **267**, 151.
Chlewicki, G., and Greenberg, J. M. 1984, *M.N.R.A.S.*, **210**, 791; **211**, 719.
Cook, G. R., Metzger, P. H., and Ogawa, M. 1965, *Canadian J. Phys.*, **43**, 1706.
Cooper, D. L., and Kirby, K. 1987, *J. Chem. Phys.*, **87**, 424.
Crawford, M. K., Genzel, R., Townes, C. H., and Watson, D. M. 1985, *Ap. J.*, **291**, 755.
Crawford, M. K., Lugten, J. B., Fitelson, W., Genzel, R., and Melnick, G. 1986, *Ap. J.* (*Letters*), **303**, L57.
Crutcher, R. M. 1985, *Ap. J.*, **288**, 604.
Crutcher, R. M., and Chu, Y.-H. 1985, *Ap. J.*, **290**, 251.
Danks, A. C., Federman, S. R., and Lambert, D. L. 1984, *Astr. Ap.*, **130**, 62.
de Jong, T., Dalgarno, A., and Boland, W. 1980, *Astr. Ap.*, **91**, 68.
Dickman, R. L. 1978, *Ap. J. Suppl.*, **37**, 407.
Draine, B. T. 1978, *Ap. J. Suppl.*, **36**, 595.
———. 1986, *Ap. J.*, **310**, 408.
Draine, B. T., and Katz, N. S. 1986*a*, *Ap. J.*, **306**, 655.
———. 1986*b*, *Ap. J.*, **310**, 392.
Draine, B. T., and Lee, H. M. 1984, *Ap. J.*, **285**, 89.
Duvert, G., Cernicharo, J., and Baudry, A. 1986, *Astr. Ap.*, **164**, 349.
Eidelsberg, M., Launay, F., Rostas, F., le Floch, A., Breton, J., and Thiebleemont, B. 1984, *Ann. Israel. Phys. Soc.*, **6**, 240.
Eidelsberg, M., Letzelter, C., and Rostas, F. 1987, in preparation.
Falgarone, E., and Pérault, M. 1987, in *Physical Processes in Interstellar Clouds*, ed. G. Morfill and M. S. Scholer (Dordrecht: Reidel), p. 59.
Falgarone, E., and Puget, J. L. 1985, *Astr. Ap.*, **142**, 157.
Federman, S. R., Glassgold, A. E., Jenkins, E. B., and Shaya, E. J. 1980, *Ap. J.*, **242**, 545.
Federman, S. R., and Lambert, D. L. 1988, *Ap. J.*, **328**, 777.
Fitzpatrick, E. L., and Massa, D. 1988, *Ap. J.*, **328**, 734.
Fock, J.-H., Gürtler, P., and Koch, E. E. 1980, *Chem. Phys.*, **47**, 87.
Frerking, M. A., Langer, W. D., and Wilson, R. W. 1982, *Ap. J.*, **262**, 590.
Frerking, M. A., Keene, J., Blake, G. A., and Phillips, T. G. 1988, *Ap. J.*, submitted.
Gatley, I., and Kaifu, N. 1987, in *IAU Symposium 120, Astrochemistry*. ed. M. S. Vardya and S. P. Tarafdar (Dordrecht: Reidel), p. 153.
Gatley, I., *et al.* 1987, *Ap. J.* (*Letters*), **318**, L73.
Glassgold, A. E., Huggins, P. J., and Langer, W. D. 1985, *Ap. J.*, **290**, 615.
Gondhalekar, P. M., Phillips, A. P., and Wilson, R. 1980, *Astr. Ap.*, **85**, 272.
Gredel, R., Lepp, S., and Dalgarno, A. 1987, *Ap. J.* (*Letters*), **323**, L137.
Gredel, R., and Münch, G. 1986, *Astr. Ap.*, **154**, 336.
Grewing, M. 1975, *Astr. Ap.*, **38**, 391.
Habing, H. J. 1968, *Bull. Astr. Inst. Netherlands*, **19**, 421.
Hawkins, I., and Jura, M. 1987, *Ap. J.*, **317**, 926.
Henry, R. C. 1977, *Ap. J. Suppl.*, **33**, 451.
Henry, R. C., Anderson, R. C., and Fastie, W. G. 1980, *Ap. J.*, **239**, 859.
Hobbs, L. M., Black, J. H., and van Dishoeck, E. F. 1983, *Ap. J.* (*Letters*), **271**, L95.
Holberg, J. B. 1986, *Ap. J.*, **311**, 969.
Huber, K. P., and Herzberg, G. 1979, *Constants of Diatomic Molecules* (Princeton: van Nostrand Reinhold).
Hudson, R. D. 1971, *Rev. Geophys. Space Phys.*, **9**, 305.
Huffman, R. E., Larrabee, J. C., and Tanaka, Y. 1964, *J. Chem. Phys.*, **40**, 2261.
Jaffe, D. T., Harris, A. I., Silber, M., Genzel, R., and Betz, A. L. 1985, *Ap. J.* (*Letters*), **290**, L59.
Jannuzi, B. T., Black, J. H., Lada, C. J., and van Dishoeck, E. F. 1988, *Ap. J.*, **332**, in press.
Jenkins, E. B., and Shaya, E. J. 1979, *Ap. J.*, **231**, 55.
Jenkins, E. B., *et al.* 1988, in preparation.
Jura, M. 1974, *Ap. J.*, **191**, 375.
Keene, J., Blake, G. A., Phillips, T. G., Huggins, P. J., and Beichman, C. A. 1985, *Ap. J.*, **299**, 967.

Kirby, K., and Cooper, D. L. 1987, in preparation.
Knapp, G. R., and Bowers, P. F. 1988, *Ap. J.*, **331**, 974.
Kurucz, R. L. 1979, *Ap. J. Suppl.*, **40**, 1.
Kurucz, R. L., Peytremann, E., and Avrett, E. H. 1974, *Blanketed Model Atmospheres for Early-Type Stars* (Washington, DC: Smithsonian Institution Press).
Lada, E. A., and Blitz, L. 1988, *Ap. J. (Letters)*, **326**, L69.
Langer, W. D. 1976, *Ap. J.*, **206**, 699.
Langer, W. D., Graedel, T. E., Frerking, M. A., and Armentrout, P. B. 1984, *Ap. J.*, **277**, 581.
Langer, W. D., Glassgold, A. E., and Wilson, R. W. 1987, *Ap. J.*, **322**, 450.
Lee, L. C., and Guest, J. A. 1981, *J. Phys. B*, **14**, 3415.
Letzelter, C., Eidelsberg, M., Rostas, F., Breton, J., and Thieblemont, B. 1987, *Chem. Phys.*, **114**, 273.
Lepp, S., Dalgarno, A., van Dishoeck, E. F., and Black, J. H. 1988, *Ap. J.*, **329**, 418.
Lindholm, E. 1968, *Arkiv Fys.*, **40**, 103.
Lutz, B. L., and Crutcher, R. M. 1983, *Ap. J. (Letters)*, **271**, L101.
Magnani, L., Blitz, L., and Mundy, L. 1985, *Ap. J.*, **295**, 402.
Maloney, P., Black, J. H., and van Dishoeck, E. F. 1988, in preparation.
Mamon, G. A., Glassgold, A. E., and Huggins, P. J. 1988, *Ap. J.*, **328**, 797.
Massa, D., and Savage, B. D. 1985, *Ap. J.*, **299**, 905.
Mathis, J. S., Mezger, P. G., and Panagia, N. 1983, *Astr. Ap.*, **128**, 212.
Mattila, K. 1986, *Astr. Ap.*, **160**, 157.
Melnick, G. 1987, in *IAU Symposium 120, Astrochemistry*, ed. M. S. Vardya and S. P. Tarafdar (Dordrecht: Reidel), p. 137.
Melnick, G., Gull, G. E., and Harwit, M. 1979, *Ap. J. (Letters)*, **227**, L29.
Mihalas, D. 1972, NCAR Tech. Note TN-STR/76.
Morris, M., and Jura, M. 1983, *Ap. J.*, **264**, 546.
Morton, D. C. 1975, *Ap. J.*, **197**, 85.
Ogawa, S., and Ogawa, M. 1972, *J. Molec. Spectrosc.*, **41**, 393.
———. 1974, *J. Molec. Spectrosc.*, **49**, 454.
Opal, C. B., and Weller, C. S. 1984, *Ap. J.*, **282**, 445.
Paresce, F., and Jakobsen, P. 1980, *Nature*, **288**, 119.
Paresce, F., McKee, C. F., and Bowyer, S. 1980, *Ap. J.*, **240**, 387.
Phillips, T. G., and Huggins, P. J. 1981, *Ap. J.*, **251**, 533.
Pineau des Forêts, G., Flower, D. R., Hartquist, T. W., and Dalgarno, A. 1986, *M.N.R.A.S.*, **220**, 801.
Prasad, S. S., and Tarafdar, S. P. 1983, *Ap. J.*, **267**, 603.
Reynolds, R. J. 1986, *A.J.*, **92**, 653.
Roberge, W. G., Dalgarno, A., and Flannery, B. P. 1981, *Ap. J.*, **243**, 817.
Russell, R. W., Melnick, G., Gull, G. E., and Harwit, M. 1980, *Ap. J. (Letters)*, **240**, L99.
Sandel, B. R., Shemansky, D. E., and Broadfoot, A. L. 1979, *Ap. J.*, **227**, 808.
Savage, B. D., Bohlin, R. C., Drake, J. F., and Budich, W. 1977, *Ap. J.*, **216**, 291.
Sellgren, K. 1986, *Ap. J.*, **305**, 399.
Seaton, M. J. 1979, *M.N.R.A.S.*, **187**, 73p.
Snow, T. P. 1983, *Ap. J.*, **266**, 576.
Solomon, P. M., and Klemperer, W. 1972, *Ap. J.*, **178**, 389.
Spitzer, L., Cochran, W. D., and Hirschfeld, A. 1974, *Ap. J. Suppl.*, **28**, 373.
Spitzer, L., and Morton, W. A. 1976, *Ap. J.*, **204**, 731.
Stark, G., Smith, P. L., Yoshino, K., and Parkinson, W. H. 1987, private communication.
———. 1988, private communication.
Sternberg, A., and Dalgarno, A. 1988, *Ap. J.*, submitted.
Stutzki, J., Stacey, G. J., Genzel, R., Harris, A. I., Jaffe, D. T., and Lugten, J. B. 1988, *Ap. J.*, in press.
Tielens, A. G. G. M., and Hollenbach, D. 1985, *Ap. J.*, **291**, 722; 747.
Tilford, S. G., and Vanderslice, J. T. 1968, *J. Molec. Spectrosc.*, **26**, 419.
Tilford, S. G., Vanderslice, J. T., and Wilkinson, P. G. 1965, *Canadian J. Phys.*, **43**, 450.
van Dishoeck, E. F. 1987, in *IAU Symposium 120, Astrochemistry*, ed. M. S. Vardya and S. P. Tarafdar (Dordrecht: Reidel), p. 51.
———. 1988*a*, in *Rate Coefficients in Astrochemistry*, ed. T. J. Millar and D. A. Williams (Dordrecht: Kluwer), p. 49.
———. 1988*b*, in *Millimetre and Submillimetre Astronomy*, ed. R. D. Wolstencroft and W. B. Burton (Dordrecht: Kluwer), p. 117.
van Dishoeck, E. F., and Black, J. H. 1986*a*, *Ap. J. Suppl.*, **62**, 109.
———. 1986*b*, *Ap. J.*, **307**, 332.
———. 1987, in *Physical Processes in Interstellar Clouds*, ed. G. Morfill and M. S. Scholer (Dordrecht: Reidel), p. 241.
———. 1988*a*, in *Rate Coefficients in Astrochemistry*, ed. T. J. Millar and D. A. Williams (Dordrecht: Kluwer), p. 209.
———. 1988*b*, *Ap. J.*, submitted.
van Dishoeck, E. F., and de Zeeuw, T. 1984, *M.N.R.A.S.*, **206**, 383.
Viala, Y. P., Letzelter, C., Eidelsberg, M., and Rostas, F. 1988, *Astr. Ap.*, **193**, 265.
Wannier, P. G., Penzias, A. A., and Jenkins, E. B. 1982, *Ap. J.*, **254**, 100.
Watson, D. M. 1985, *Phys. Scripta*, **T11**, 33.
Williams, D. A. 1985, *Quart. J. R. A. S.*, **26**, 463.
Witt, A. N., and Johnson, M. W. 1973, *Ap. J.*, **181**, 363.
Woods, T. N., Feldman, P. D., and Bruner, G. H. 1985, *Ap. J.*, **292**, 676.
Yoshino, K., Stark, G., Smith, P. L., Parkinson, W. H., and Ito, K. 1988, *J. Phys.*, in press.
Young, J. S., Goldsmith, P. F., Langer, W. D., Wilson, R. W., and Carlson, E. R. 1982, *Ap. J.*, **261**, 513.
Zmuidzinas, J., Betz, A. L., and Goldhaber, D. M. 1986, *Ap. J. (Letters)*, **307**, L75.

JOHN H. BLACK: Steward Observatory, University of Arizona, Tucson AZ 85721

EWINE F. VAN DISHOECK: Center for Cosmochemistry, Division of Geological and Planetary Sciences, California Institute of Technology, 170-25 Pasadena, CA 91125